

AN ABSTRACT OF THE DISSERTATION OF

Sumate Pengpumkiat for the degree of Doctor of Philosophy in Chemistry presented on March 17, 2017.

Title: Semiconductor Nanocrystals as Detection Components in Microfluidic Analytical Systems.

Abstract approved:

Vincent T. Remcho

Miniaturized and portable microfluidic analytical platforms have been widely explored in the broad field of chemical analysis. The concept of microfluidics offer a number of important advantages, including low reagent consumption, low-cost detection, high sample throughput, and shorter analysis time. Semiconductor nanocrystals or quantum dots have been extensively utilized in a wide variety of manners including as emitters in consumer products (light bulbs) and, more importantly here, as elements for chemical and biological sensing. These applications are possible because of their unique optical and electronic properties. The goal of this dissertation was to integrate two fields of study – microfluidics for chemical and biological analysis, and semiconductor nanocrystals for detection – into a single analytical device. In this work, the development of microfluidic analytical devices incorporating semiconductor nanocrystals for chemical sensing is presented.

The research effort started with the synthesis of a dual emission fluorescent quantum dot pair. CdTe quantum dots of two different sizes, emitting green and red

light, were utilized as fluorophores. The green dot was used as a constant emitter and was encapsulated in a silica shell. The red dot was immobilized on the silica surface and selectively quenched in the presence of copper. The wavelength-ratiometric sensor thus constructed resulted in a fluorescence color change from red to green, identified visually, corresponding to the absence and presence of copper. The wavelength-ratiometric sensor was transferred to a microfluidic format made of poly(methyl methacrylate) (PMMA) and assembled using polycaprolactone (PCL). Red and green intensity values from the RGB colorspace were used as analytical signals to generate a calibration curve. A Stern-Volmer plot in the range of 1-30 mg/L was used to quantify copper in water samples. For serum samples, absolute intensity values of green and red were plotted to mitigate non-linearity in the Stern-Volmer plot arising from the formation of copper-protein complexes.

The research continued with the development of a quantum dot assay performed in a paper-based well plate format for cyanide detection. Chitosan modified CdTe quantum dots (CS-QDs) were synthesized and used as a fluorophore. The CS-QDs were quenched with copper and deposited onto a glass microfiber filter (GF/B). The paper-based well plate resembled a conventional plastic well plate in its x and y dimensions, to facilitate detection in a plate reader, and was designed to contain three layers: an opaque floor, a middle layer containing the reagents in a GF/B matrix, and an upper layer that retained the reagent pads while providing direct access to the individual wells for sample application and optical interrogation. The dried assay of quenched CS-QDs on GF/B was assembled on a paper-based well plate using PCL as a hydrophobic barrier and adhesive for each individual assay. The

introduction of cyanide triggered recovery of a fluorescent signal from the CS-QDs in proportion to cyanide concentration, arising from copper-cyanide complex formation and depletion of copper from the QD surface. Linear calibration was measured in the range of 0-200 μM within 30 min. A paper-based well plate using CS-QDs made rapid, high sample throughput, low-cost testing feasible and convenient for cyanide detection. The color change was visually perceptible (making field use feasible) and the fluorescence output change was readily and sensitively measured, with greater accuracy and precision, using an automated plate reader.

In the final component of the research effort described here, a novel method of constructing dsDNA, aimed at total gene synthesis on a shortened timescale and with a reduced error rate, was developed. Short (28-mer) oligo fragments from a library were assembled through successive annealing and ligation processes, followed by polymerase chain reaction (PCR) amplification. First, two oligo fragments annealed to form a double-stranded DNA molecule (dsDNA). The dsDNA was immobilized onto magnetic beads as solid support via streptavidin-biotin binding. Next, single-stranded oligo fragments were successively added through ligation to form the complete DNA molecule. More than 97% of the nucleotides matched the expected sequence. Coupled with an automated dispensing system and libraries of short oligo fragments, this novel dsDNA synthesis method offers an efficient and cost-effective method for dsDNA production. The longer-term aim of the project is to utilize inkjet deposition technology to fully automate the assembly process.

©Copyright by Sumate Pengpumkiat
March 17, 2017
All Rights Reserved

Semiconductor Nanocrystals as Detection Components in Microfluidic
Analytical Systems

by
Sumate Pengpumkiat

A DISSERTATION

submitted to

Oregon State University

in partial fulfillment of
the requirements for the
degree of

Doctor of Philosophy

Presented March 17, 2017
Commencement June 2017

Doctor of Philosophy dissertation of Sumate Pengpumkiat presented on March 17, 2017

APPROVED:

Major Professor, representing Chemistry

Chair of the Department of Chemistry

Dean of the Graduate School

I understand that my dissertation will become part of the permanent collection of Oregon State University libraries. My signature below authorizes release of my dissertation to any reader upon request.

Sumate Pengpumkiat, Author

ACKNOWLEDGEMENTS

Firstly, I would like to express my sincere gratitude to my advisor, Professor Vincent T. Remcho for his patient, motivation, continuous support throughout my graduate career. His invaluable guidance and enthusiasm have helped me in all time, not only in the research area but also in all stages of my study here at OSU. His mentorship has made me an independent initiator in science.

I would like to extend my appreciation to my graduate committees: Dr. Staci Simonich, Dr. Sean Burrows, Dr. Dipankar Koley, Dr. David McIntyre and Dr. Neal Sleszynski for their insightful comments, valuable time and commitment to serve in my academic committees.

My sincere thank goes to the exceptional people that I have worked with in the past and present members/collaborators in the Remcho research group for their friendship, encouragement and support: Dr. Myra Koesdjojo, Dr. Jintana Nammoonnoy, Dr. Adeniyi Adenuga, Dr. Yuanyuan Wu, Dr. Christopher A. Heist, Anukul Boonloed, Chandima Bandara, Kelly Ramzy, Matthew Kremer, Saichon Sumantakul, Dr. Ngoc Nguyen, Wei Xu, Peng Yu, Leslie Loh, Lindsey Sequeira, Dr. Genevieve Weber, Dr. Yolanda Tennico, Sara Townsend, Chadd Armstrong, Simon Brundage, Emily Schumacher, Andrew McKelvey, Daniel Huynh, Derek Wong, Joel Pommerenck, Pascal Sanchez, and Lorena Colcer.

I acknowledge the technical support from Teresa Sawyer and Dr. Peter Eschbach for their helps on SEM and TEM. Many thanks also go to Dr. Shay Bracha,

Dr. Sergei Filichkin, and Nicole J. Hams for their technical discussion. I thank the Department of Chemistry at OSU, the faculty, staffs for their support.

I would like to thank my joyful friend, Craig E. Brauer for his moral support, encouragement and editorial review.

I am grateful for the financial supports from The Ministry of Science and Technology, Royal Thai government. I greatly appreciate Dr. Wantanee Phanprasit for her understanding and giving me an opportunity to study at OSU.

Most importantly, I would like to thank my parents, Boonplod and Sunanta Pengpumkiat, for their understanding, unconditionally endless love and eternal supports throughout my life. I love you, Dad and Mom.

CONTRIBUTION OF AUTHORS

My research advisor, Dr. Vincent T. Remcho, edited and assisted in writing all chapters of this dissertation. His name appears on all published and submitted work contained herein. Dr. Yuanyuan Wu assisted with the design and the writing of Chapter 2 and 3. Anukul Boonloed and Gayan C. Bandara were involved with the design of Chapter 2. Dr. Christopher A. Heist and Saichon Sumantakul were involved with design and the writing of Chapter 3. Dr. Myra Koesdjojo collaborated and contributed in designing and the writing of Chapter 4 of this dissertation.

TABLE OF CONTENTS

	<u>Page</u>
1. Introduction to semiconductor nanocrystals, fluorescence quenching, and fluorescence based microfluidic detection	1
1.1 Semiconductor nanocrystals	1
1.1.1 Introduction to semiconductor nanocrystals and optical properties.....	1
1.1.2 General synthesis routes for semiconductor nanoparticles	5
1.1.2.1 Non-aqueous / organometallic synthesis.....	5
1.1.2.2 Aqueous synthesis	7
1.1.3 Core/shell quantum dots.....	8
1.1.4 Surface modification and functionalization	10
1.1.5 The advantages of quantum dots.....	12
1.2 Types of fluorescence quenching.....	14
1.2.1 Dynamic quenching.....	14
1.2.2 Static quenching	15
1.3 Fluorescence detection in microfluidic systems	17
1.4 Reference	22
2. A microfluidic detection system for quantitation of copper incorporating a wavelength-ratiometric fluorescent quantum dot pair.....	25
2.1 Abstract.....	27
2.2 Introduction.....	28
2.3 Materials and methods	32
2.3.1 Materials.....	32
2.3.2 Synthesis of CdTe quantum dots.....	33

TABLE OF CONTENTS (Continued)

	<u>Page</u>
2.3.3 Synthesis of CdTe/CdS core/shell quantum dots	34
2.3.4 Silica encapsulation of CdTe Quantum dots	34
2.3.5 Assembly of the ratiometric sensor	35
2.3.6 Microfluidic chip design	36
2.3.7 Deposition of QD ratiometric sensor on a chip.....	36
2.3.8 Quantitation of copper ion on a chip	37
2.4 Results and discussion	38
2.4.1 Characterization of CdTe QDs and CdTe/CdS core/shell QDs	38
2.4.2 Characterization of the QD ratiometric sensor.....	39
2.4.3 Detection mechanism and Stern-Volmer calibration plot	42
2.4.4 Measurement of copper in water samples and assay optimization	43
2.4.5 Assay specificity of QD ratiometric probe.....	44
2.4.6 Reaction time for color development	45
2.4.7 Calibration of devices for application to environmental water samples	48
2.4.8 Measurement of copper in serum samples	50
2.5 Conclusions.....	53
2.6 Acknowledgments.....	54
2.7 References.....	54
3. A paper-based disposable well plate for cyanide detection incorporating a fluorescent chitosan-CdTe quantum dot nanoparticle.....	57
3.1 Abstract	58
3.2 Introduction.....	59

TABLE OF CONTENTS (Continued)

	<u>Page</u>
3.3 Materials and methods	63
3.3.1 Materials.....	63
3.3.2 Synthesis of core CdTe quantum dots.....	64
3.3.3 Synthesis of chitosan encapsulated CdTe quantum dots (CS-QD520).....	64
3.3.4 Cyanide probe - Quenching of CS-QD520 by copper ion	65
3.3.5 Paper-based well plate and a plate holder	65
3.3.6 Quantitation of cyanide ion on a chip	67
3.4 Results and discussion	68
3.4.1 Characterization of CdTe QDs and chitosan encapsulated QDs.....	68
3.4.2 Paper-based well plate design and evaluation.....	70
3.4.3 Detection mechanism and selectivity.....	72
3.4.4 Optimization of the cyanide assay on paper-based well plate	74
3.4.5 Quantitative cyanide analysis.....	76
3.4.6 Real sample analysis	77
3.4.7 Kinetic fluorescent method for cyanide detection	79
3.5 Conclusions.....	82
3.6 Acknowledgments.....	83
3.7 References.....	83
4. Rapid synthesis of a long double-stranded oligonucleotide from a single-stranded nucleotide using magnetic beads and an oligo library.....	86
4.1 Abstract.....	88
4.2 Introduction.....	89

TABLE OF CONTENTS (Continued)

	<u>Page</u>
4.3 Materials and methods	93
4.3.1 Materials.....	93
4.3.2 Preparation of Streptavidin-coated magnetic beads.....	95
4.3.3 Annealing process	95
4.3.4 Binding streptavidin coated-magnetic beads and biotinylated oligos.....	95
4.3.5 Ligation	96
4.3.6 Polymerase chain reaction (PCR)	96
4.3.7 Gel electrophoresis.....	97
4.3.8 Sanger DNA sequencing	97
4.3.9 One-pot dsDNA synthesis.....	97
4.4 Results and discussion	97
4.4.1 Annealing	98
4.4.2 Ligation	99
4.4.3 Oligonucleotide synthesis using streptavidin-coated magnetic beads	101
4.4.4 Sequencing of the target DNA	103
4.5 Conclusions.....	104
4.6 Acknowledgments.....	105
4.7 References.....	105
5. Summary and conclusions.....	107
5.1 References.....	110

LIST OF FIGURES

<u>Figure</u>	<u>Page</u>
1.1 Energy bandgap of semiconductor nanocrystals at different sizes of nanocrystals.	2
1.2 Various types and sizes of quantum dots, and their size-dependent fluorescence emission properties.....	5
1.3 The stages of nucleation and growth in the preparation of monodisperse QDs from the classical La Mer model	6
1.4 Schematic diagrams showing the energy level alignment in type-I and type-II core/shell systems.	9
1.5 Schematic diagram for multiple quantum dots (QD cluster) encapsulation in a silica shell.....	11
1.6 Size-dependent optical properties of MPA-capped CdTe QDs	13
1.7 Schematic diagram for dynamic fluorescence quenching.	15
1.8 Schematic diagrams for static fluorescence quenching.	16
1.9 Comparison of the temperature sensitivities of dynamic and static quenching processes.	17
2.1 Microfluidic chip design and detection system for color measurement using a QD ratiometric sensor.....	36
2.2 Absorption spectra of QD530 (green) and QD650 (red) and Fluorescence emission spectra of QD530 and QD650.	38
2.3 Spectra of QD ratiometric sensors prepared by varying the relative amounts of QD650 and QD530 to optimize the relative red/green fluorescence signal.	40
2.4 Scanning electron microscope images.....	41
2.5 The assay specificity of a microfluidic ratiometric probe to various cations generally found in environmental waters and serum samples.	44
2.6. Effect of reaction time on sensitivity and linearity of the calibration curve.....	47
2.7 RGB profile plot for a microfluidic QD ratiometric sensor after application of copper standards.....	48

LIST OF FIGURES (Continued)

<u>Figure</u>	<u>Page</u>
2.8 calibration curve derived from the Stern-Volmer plot for microfluidic copper detection in water samples.....	49
2.9 calibration curve derived from a Stern-Volmer plot for microfluidic copper detection from copper-fortified serum sample.....	52
3.2 A Paper-based well plate resembling a standard plastic 96 well plate designed for use in a plate reader.....	66
3.3 A plate holder for the paper-based well plate.....	67
3.4 Characterization of chitosan encapsulated CdTe QDs (CS-QD520).....	69
3.5 Interaction of CS-QD520 on the GF/B surface.....	70
3.6 Evaluation of 3-layered paper-based well plates for a PCL hydrophobic barrier.	71
3.7 Evaluation of 4-layer paper-based well plates for a PCL hydrophobic barrier. ...	72
3.8 Selectivity of the assay on paper-based well plates.....	73
3.9 Comparative study of assay sensitivity.....	74
3.10 Optimization parameters for cyanide detection on paper-based well plates.....	76
3.11 Endpoint calibration graph derived from paper-based well plates.....	77
3.12 Calibration graphs plotted between cyanide concentrations and fluorescence intensity.....	80
3.13 Kinetic fluorescence method.....	81
4.1 Schematic diagram for the proposed dsDNA synthesis.....	93
4.2 Schematic of the building blocks for DNA construction.....	94
4.3 Agarose gel electrophoresis of annealed and ligation products.....	99
4.4 Agarose gel electrophoresis of the final product.....	102
4.5 DNA sequencing alignment of the final product.....	104

LIST OF TABLES

<u>Table</u>	<u>Page</u>
Table 1.1 The bandgap energies of selected bulk semiconductors in electron volts (eV).....	4
Table 2.1 Recovery test of microfluidic copper detection in water samples.....	50
Table 2.2 Recovery data for microfluidic copper detection of samples prepared in fetal bovine serum samples (n=40).....	53
Table 3.1 Recovery of cyanide at different concentrations in drinking water.....	78
Table 3.2 Thermodynamic quantities for the Cu^+ and CN^- system.	79
Table 3.3 The relationship between cyanide concentrations and reaction rates.	82
Table 4.1 Sequence of the oligo fragments used to form the complete dsDNA.....	94

SEMICONDUCTOR NANOCRYSTALS AS DETECTION COMPONENTS IN MICROFLUIDIC ANALYTICAL SYSTEMS

CHAPTER 1

INTRODUCTION TO SEMICONDUCTOR NANOCRYSTALS, FLUORESCENCE QUENCHING, AND FLUORESCENCE DETECTION IN MICROFLUIDIC SYSTEMS

The introductory chapter provides a general background and reviews recent advancements in the use of semiconductor nanocrystals as fluorophores in microfluidic analytical devices. The chapter is divided into three sections: (1) a review of semiconductor nanocrystals, their optical properties, synthetic routes, and surface modification; (2) a review of fluorescence quenching, which can be an effective analytical tool for quantitative chemical analysis; and (3) a review of fluorescence detection methods employed in the microfluidic format. Applications of semiconductor nanocrystals in microfluidic chips are presented in Chapters 2 and 3.

1.1 Semiconductor nanocrystals

1.1.1 Introduction to semiconductor nanocrystals and optical properties

Semiconductor nanocrystals or quantum dots (QDs) are nanomaterials comprised of an inorganic core semiconductor, and have diameters in the range of 2-10 nm. They are generally composed of atoms from the group II-VI or III-V elements. Energy bandgaps of semiconductors are small enough that electrons can readily be promoted from the lower valance band to the conduction band. Quantum dots exhibit unique electronic properties, intermediate between those of bulk

semiconductors and discrete molecules. Due to their small size, when the radii of the semiconductor nanocrystals are smaller than the exciton Bohr radius (the average distance between the electron in the conduction band and the hole in the valence band), the electrons are confined in quantized energy levels – thus they are referred to as quantum dots. In general, as the size of the nanocrystal increases, the difference in energy between the highest valence band and the lowest conduction band decreases, as shown in Figure 1.1. Less energy is then needed to excite the quantum dot and less energy is released when the nanocrystal returns to its ground state. This phenomenon leads to an emitted light color shift from blue to red. For this reason, quantum dots comprised of the same material can emit light of differing colors, and this is accomplished simply by changing the size of the dot.

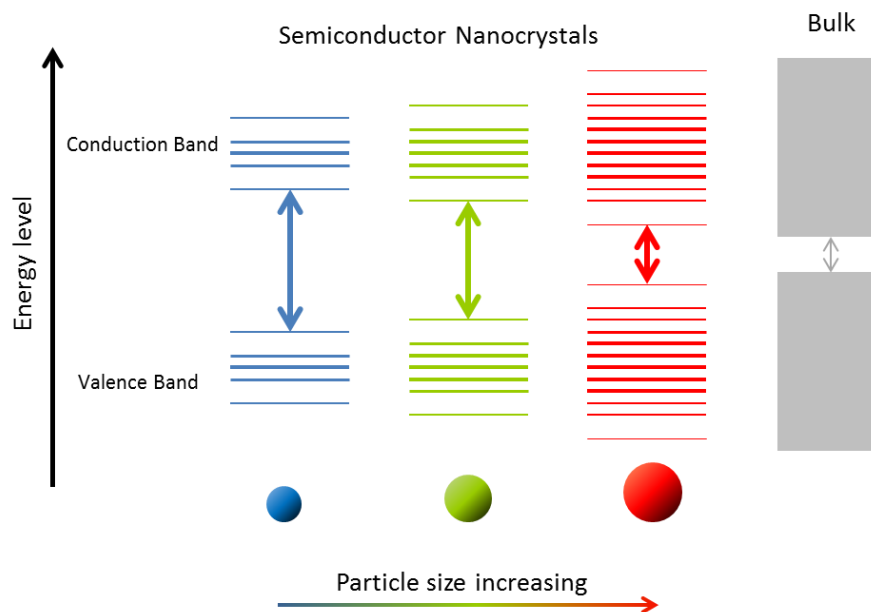


Figure 1.1 Energy bandgap of semiconductor nanocrystals at different sizes of nanocrystals.

Brus (1984)^{1,2} first published a theoretical calculation for bandgap energy of semiconductor nanoparticles based on effective mass approximation. In this study, the exciton is considered to be confined in a spherical nanocrystal volume and the absolute masses of the electron and hole are replaced by effective masses (m_e and m_h) to define the wave function:

$$E_{g(QD)} = E_{g(bulk)} + \frac{\hbar^2}{8R^2} \left(\frac{1}{m_e^*} + \frac{1}{m_h^*} \right) - \frac{1.86e^2}{4\pi\epsilon_0\epsilon_r R}$$

where $E_{g(QD)}$ is the bandgap energy of the quantum dot, $E_{g(bulk)}$ is the bandgap energy of the bulk semiconductor, R is radius of the quantum dot, m_e^* and m_h^* are the effective masses of the excited electron and hole, respectively, and \hbar is Planck's constant.

The first term on the right side of the equation represents the band gap energy, which is a bulk material characteristic. The choice of semiconductor material, therefore, essentially indicates the available fluorescence emission wavelength range for QDs produced using that material. The second term of the equation represents the additional energy attributable to the quantum confinement effect, which depends on the inverse of the nanoparticle radius; (R^{-2}). In general, the bandgap energy for a given QD decreases with increasing size of the nanoparticle, which reflects the experimentally determined size-dependent optical emission properties of these unique nanoparticles. The third term accounts for the coulombic interaction energy (usually negligible due to the high dielectric constants typical of semiconductor materials). This equation indicates that the bandgap energies of quantum dots are larger than those for bulk materials of the same elemental composition.

Table 1.1 The bandgap energies of selected bulk semiconductors in electron volts (eV), corresponding to fluorescence emission wavelength in nanometers.³

Materials	Type	Band gap (eV) @ 300K	nm
ZnS	II-VI	3.60	344
ZnSe	II-VI	2.70	459
ZnTe	II-VI	2.25	551
CdS	II-VI	2.42	512
CdSe	II-VI	1.73	717
CdTe	II-VI	1.49	832
InP	III-V	1.35	919
InAs	III-V	0.36	3444
PbS	IV-VI	0.37	3351
PbSe	IV-VI	0.27	4593
PbTe	IV-VI	0.29	4276

Each type of semiconductor nanocrystal has its own set of optical emission characteristics, and these characteristics are largely based on the bandgap energy of the bulk materials. Table 1.1 shows the bandgap energies for some bulk semiconductors and their predicted emission wavelengths, which correlate to the graphs in Figure 1.2A, illustrating the different types of quantum dots and their emission wavelengths. For emission in the visible region (400-700 nm), CdSe and CdTe QDs are available and suitable for many applications.

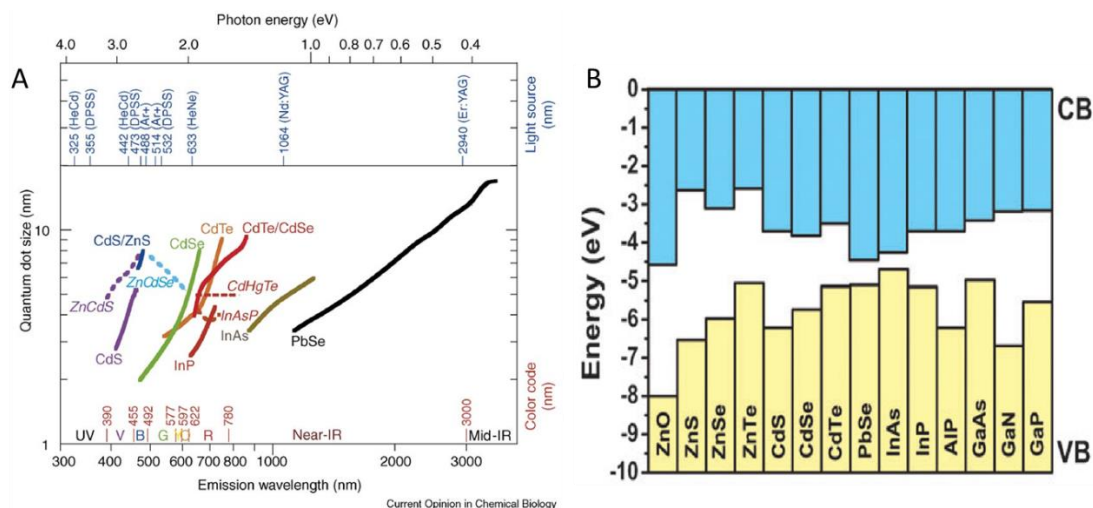


Figure 1.2 (A) Various types and sizes of quantum dots, and their size-dependent fluorescence emission properties. (A) Reprinted from *Current Opinion in Chemical Biology*, 10, S. K. Shin, H. Yoon, Y. J. Jung, J. W. Park, Nanoscale controlled self-assembled monolayers and quantum dots, p.426, Copyright (2006) (Ref. 4), with permission from Elsevier; (B) The electronic energy levels of selected semiconductors; CB = conduction band, VB = valence band; Reproduced from C. de M. Donegá, *Chem. Soc. Rev.*, 2011, 40, 1512–1546 (Ref. 5) with permission of The Royal Society of Chemistry.

1.1.2 General synthesis routes for semiconductor nanoparticles

1.1.2.1 Non-aqueous / organometallic synthesis

The non-aqueous QD synthetic approach was initially developed by Bawendi,⁶ Alivisatos^{7–9} and Peng¹⁰ in the 1990s. The fundamental elements of the approach include metallic or organometallic precursors (cadmium, zinc, mercury) along with chalcogen precursors (sulfur, selenium, or tellurium) in a coordinating solvent at high temperature. The pyrolysis of cadmium organometallic precursors with selenium or tellurium has been extensively used for synthesizing CdSe or CdTe QDs, respectively. In general, dimethyl cadmium is first dissolved in trioctylphosphine (TOP) and trioctylphosphine oxide (TOPO) at 230–300°C.

TOP/TOPO represents a long-chain surface passivating ligand for hydrophobic QDs. After the decomposition of precursors, the solution becomes supersaturated and nucleation begins. With this, the concentration of precursors dramatically declines to a level below the critical value for nucleation. As a result, the existing nucleated particles continue to grow without further formation of new nuclei, as shown in Figure 1.3. Reaction time is a key parameter for successful growth of nanoparticles of a given size: longer reaction times result in larger average particle size.

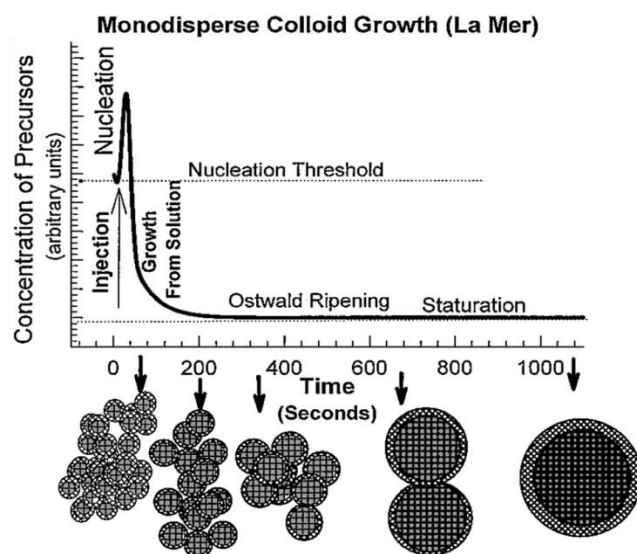


Figure 1.3 The stages of nucleation and growth in the preparation of monodisperse QDs from the classical La Mer model¹¹ including monomer accumulation, nucleation, and growth. As nanoparticles grow with time, it depletes the precursor concentration from the reaction vessel. (Reproduced from Ref. 12, with permission).

An organic outer layer or stabilizing agent must be present in the solution during the growth period to prevent aggregation and precipitation of the nanoparticles. The stabilizing agent is preset on the nanoparticle surface as a monolayer capping agent, passivating the nanoparticle surface in a manner analogous

to the binding of ligands in traditional coordination chemistry. In order to use hydrophobic QDs in the aqueous phase, the nanoparticle surface can be modified via ligand exchange with hydrophilic capping agents such as mercaptoacetic acid or mercaptopropionic acid.

1.1.2.2 Aqueous synthesis

Thermodynamically, direct aqueous synthesis of QDs is associated with some important parameters. First, the solubility product of semiconductor compounds in water can be used to predict the formation of the desired nanoparticles. Second, nanoparticle formation depends on the chemistry of the semiconductors. Soft acids prefer to bind strongly with soft bases. Thus far, the aqueous approaches have proven to be more suitable for synthesizing II-VI, I-III-VI, I-VI semiconductor nanocrystals¹³ such as Zn(S, Se, Te), Cd(S, Se, Te), Hg(S, Se, Te), Pb(S, Se), CuIn(S, Se)₂, Ag₂(S, Se, Te). Third, a capping agent is necessary in the aqueous synthesis of QDs. Water-soluble small molecules, amphiphilic molecules, macromolecules or hydrophilic polymers can be used as capping agents. These molecules serve to mediate the growth of QDs, electrostatically or sterically. They effectively bind to the QD surface via covalent, dative (coordinate covalent), or ionic bonds.

The pH of the aqueous solution modulates the binding affinity of the capping agent. A basic solution is normally used as a medium for the aqueous synthesis due to the fact that high pH enables thiol-thiolate equilibrium to form the RS⁻ species, which can bind strongly to the QD surface.¹⁴

1.1.3 Core/shell quantum dots

Quantum dots can be fabricated as heterostructures, and are called core/shell quantum dots. Inorganic core QDs can be coated with layers of a second different semiconductor of wider bandgap forming core/shell QDs. The shell QDs play different roles in core/shell systems depending on the bandgaps and relative positions of electronic energy levels of the core and shell QDs. Core/shell QDs systems are generally classified into 2 types: type I and type II.

Schematic diagrams of the energy-level alignment in two different core/shell systems are shown in Figure 1.2B. For type-I core/shell QDs; the bandgap of the shell semiconductor is wider and covers the bandgap of the core material. The conduction band of the shell is of higher energy than that of the core and the valence band of the shell is of lower energy than that of the core. Both electrons and holes are confined in the core QDs. The shell of the nanoparticle physically shields the core from its surrounding medium leading to an improvement in optical properties; namely, an increase fluorescent quantum yield and enhanced stability against photodegradation. The most studied type-I core/shell QDs system is CdSe/ZnS¹⁵ due to the wider bandgap energy and lower toxicity of the outer ZnS shell. Hines and Guyot-Sionnest firstly demonstrated coating a ZnS shell on a core CdSe QD, leading to an increase in fluorescent quantum yield of up to 50%.¹⁶

For type-II core/shell systems, shell growth on the core QDs tunes the emission wavelengths of the core/shell nanoparticles. The overlapped bandgap alignment results in a smaller effective bandgap energy than for either core or shell materials alone. This engineered design largely confines one carrier to the core, while

the other is mostly confined to the shell. The thickness of the shell can be used to manipulate the emission color over a given spectral range, making it possible to obtain longer wavelength emissions (a red-shift) from 700 to 1000 nm, which would not otherwise be achievable by simply increasing the nanoparticle diameter of a single material QD. Examples of type-II systems include CdTe/CdSe and CdSe/ZnTe.¹⁷

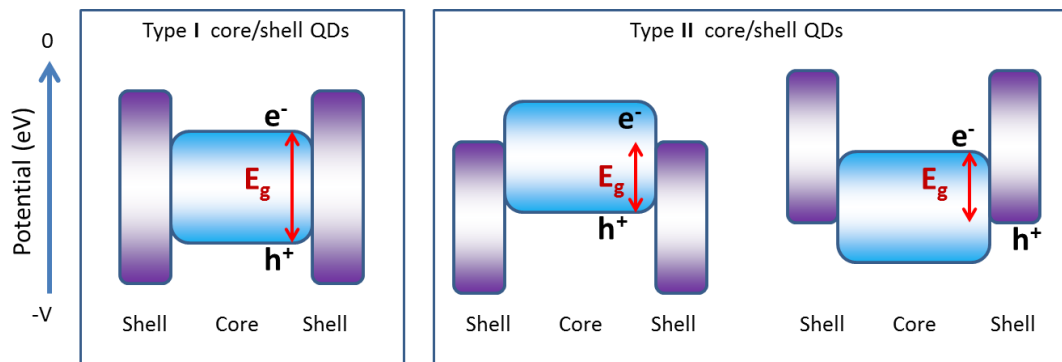


Figure 1.4 Schematic diagrams showing the energy level alignment in type-I and type-II core/shell systems.

Core/shell systems are mostly synthesized in a two-step process. The core is first formed in parallel with purification; the shell is then added using the second of semiconductor material. In order to prevent separate nucleation of the shell material and growth of a second population of dissimilar particles, the temperature used to grow the shell is generally kept lower than the temperature required to grow the core. In addition, the precursors of the shell component are slowly added to the core-particle containing solution during the core/shell synthesis.

1.1.4 Surface modification and functionalization

QD surfaces are modified in order to enhance their stability in aqueous solution over wide ranges of pH and ionic strength, to maintain/protect their optical properties, and to generate functional groups that facilitate further conjugation of the QD surface.

As mentioned in the previous section on QD synthesis, the organic outer layer (formed by the capping ligand) can be either hydrophobic or hydrophilic. In order to use QDs in various practical analytical applications, it is often important that they be soluble, or generate stable suspensions, in aqueous solutions and be able to conjugate to biomolecules, such as proteins, antibodies, aptamers, and oligonucleotides. There are several approaches to modification of the QD surface, including ligand exchange, silicate chemistry, or QD encapsulation in carrier vehicles (amphiphilic polymers, polymeric microbeads, liposomes). In this research effort, silicate chemistry and chitosan modification were employed in Chapters 2 and 3, respectively.

1.1.4.1 Silica encapsulation

Silica nanoparticles have been widely studied and have attracted much attention due to their superior chemical inertness, thermal stability, and colloidal stability. Silica particles are water-dispersible, non-toxic and biocompatible, which makes them suitable for biomedical applications and ideal for use in combination with other nanomaterials. There are a number of nanomaterials that can be cladded or “decorated” using silicate chemistry: noble metal nanoparticles, magnetic

nanoparticles, fluorescent dyes¹⁸ as well as semiconductor nanocrystals have been studied.

For semiconductor nanocrystals, two approaches to silica encapsulation of QDs have been pursued: single QD encapsulation and multiple QD encapsulation.

Single QD encapsulation generally follows a reverse microemulsion method (water-in-oil emulsion).¹⁹ The tiny aqueous droplets of the oil phase control the particle size of the silica nanoparticles. The hydrolyzed tetraethylorthosilicate (TEOS) has a high affinity for the QD surface, and a silicate layer therefore grows on the surface of the seed particle. On the other hand, multiple QD encapsulation follows a sol-gel polycondensation process. The Stober method²⁰ is used for preparation of monodisperse silica colloids by hydrolysis of alkyl silicates and subsequent condensation of silicic acid in alcoholic solutions using ammonia as a catalyst. These two steps are shown below:

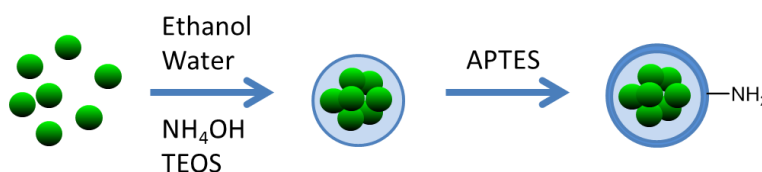
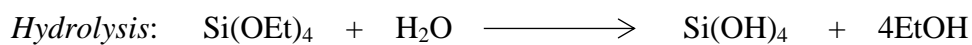


Figure 1.5 Schematic diagram for multiple quantum dots (QD cluster) encapsulation in a silica shell.

1.1.4.2 Chitosan encapsulation

Chitosan is a polysaccharide derived from naturally occurring chitin (a deacetylated product of chitin). It is an ideal polymer for a number of biological applications due to its unique chemical properties, film forming ability, pH dependent solubility, biodegradability, biocompatibility, and low toxicity.

The main use of chitosan in the field of analytical chemistry has been to serve as a matrix for the assembly of biomolecules, enzymes, nucleotides, cells, and nanoparticles (Chapter 3) due to its large number of accessible amino functional groups. Modification of the chitosan surface can therefore be achieved by physical interaction (electrostatic adsorption, entrapment) or by covalent chemical bonding (generally via peptide bonds).

For QD applications, chitosan can be directly used as a capping agent for CdS,^{21,22} and CdSe²³ QDs, resulting from the electrostatic attraction between the inorganic core surface and the amine and hydroxyl groups on the chitosan. Moreover, QDs can be incorporated with chitosan as nanoparticle composites and used for imaging,²⁴ immunoassay,²⁵ and as an electrochemical platform.²⁶

1.1.5 The advantages of quantum dots

- Quantum dots have size-dependent optical properties. Their fluorescence emission wavelengths are highly tunable, especially for the type-II core/shell QDs.
- Quantum dots demonstrate high photostability because they are made of inorganic materials.

- Broad absorption spectra and narrow symmetric emission peaks mean that a single light source can be used to excite multicolor QDs simultaneously. Multiple assays (separate or simultaneous) can therefore be developed using different colors of QDs.
- Quantum dots have large Stokes shifts; the difference between their excitation and emission wavelengths can be as high as 200 nanometers. Figure 1.6 shows MPA-capped CdTe QDs made in our lab under a 365 nm light. When illuminated by an ultraviolet light, the nanocrystal solutions glow in vibrant and distinct colors
- Surface functionalization is readily achieved, and this conjugation to various capping agents leads to a wide variety of possible applications.

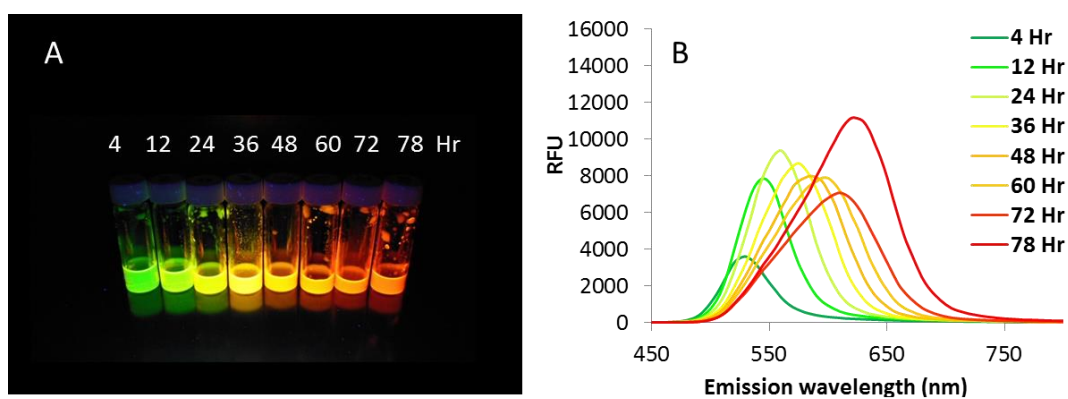


Figure 1.6 Size-dependent optical properties of MPA-capped CdTe QDs; (A) under UV 365 nm; (B) Scan emission spectra of the solutions in picture A. These MPA-capped CdTe QDs were synthesized in our lab and used in the application presented in Chapter 2.

1.2 Types of fluorescence quenching

In this research effort, the intensity of QD fluorescence was used as an analytical signal to quantify various analytes following specific sorptive events. Depending on the assay design, the increase or decrease in fluorescence was correlated to analyte concentration in solution. The principle used to obtain these analytical signals is “fluorescence quenching”. The atom or molecule that diminishes the fluorescence is called a “quencher”.²⁷ There are several molecular interactions leading to fluorescence quenching, namely: (1) excited state reaction, (2) molecular rearrangement, (3) energy transfer, (4) collisional quenching, and (5) ground state complex formation. Two main processes by which fluorescence quenching progresses are dynamic and static quenching, both of which require molecular contact between the fluorophore and the quencher. These processes can be used to study the accessibility of the fluorophore to the quencher.

1.2.1 Dynamic quenching

Dynamic or collisional quenching is a phenomenon whereby the quencher diffuses to the fluorophore during the lifetime of the excited state. As shown in Figure 1.7, electrons transition from excited state to ground state to release energy, which is absorbed by the adjacent quencher, without emission of a photon. Basically, dynamic quenching does not permanently change the quencher and fluorophore molecules.

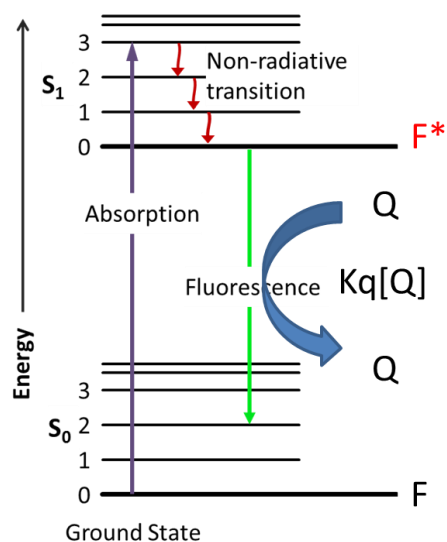


Figure 1.7 Schematic diagram for dynamic fluorescence quenching.

Dynamic quenching is described by the Stern-Volmer equation:

$$\frac{F_0}{F} = 1 + k_{SV}[Q] = k_q \tau_0 [Q]$$

Where F_0 and F are the fluorescence intensities in the absence and presence of the quencher, respectively; k_q is the biomolecular quenching constant; τ_0 is the lifetime of the fluorophore in the absence of quencher; and Q is the quencher concentration; k_{SV} is the Stern-Volmer constant ($= k_q \tau_0$).

1.2.2 Static quenching

Static quenching arises from the formation of a non-fluorescent ground state complex between the fluorophore and quencher. The complex absorbs light and immediately returns to the ground state without emission of a photon, as shown in Figure 1.8.

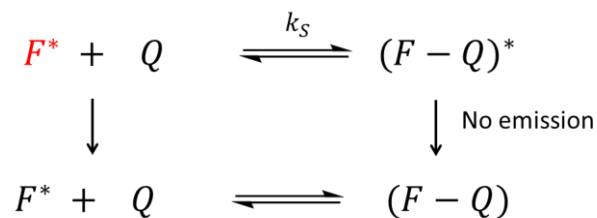


Figure 1.8 Schematic diagrams for static fluorescence quenching.

The relationship between the fluorescence intensity and the quencher concentration is given by:

$$k_S = \frac{[F - Q]}{[F][Q]} \quad (1)$$

$$\text{Recall: } [F]_0 = [F] + [F - Q] \quad (2)$$

$$k_S = \frac{[F]_0 - [F]}{[F][Q]} = \frac{[F]_0}{[F][Q]} - \frac{1}{[Q]}$$

$$\frac{F_0}{F} = 1 + k_S[Q]$$

Where K_s = association constant; $[F-Q]$ = the concentration of the complex; F_0 and F are the fluorescence intensities in the absence and presence of the quencher, respectively; $[Q]$ = the concentration of the quencher.

Both dynamic and static quenching share the same the Stern-Volmer plot; however, they can be distinguished by their differing dependence on temperature and viscosity, or lifetime measurement. Based on the Stokes-Einstein equation shown below, the diffusion of a molecule directly depends on the temperature.

$$D = \frac{kT}{6\pi\eta R}$$

where D = diffusion coefficient; k = Boltzmann's constant; T = temperature; η = the solvent viscosity; R = molecular radius.

For this reason, higher temperatures lead to more rapid molecular diffusion and therefore larger extents of collisional quenching, as shown in Figure 1.9. On the other hand, higher temperatures cause the dissociation of weakly bound complexes, resulting in smaller amounts of static quenching.

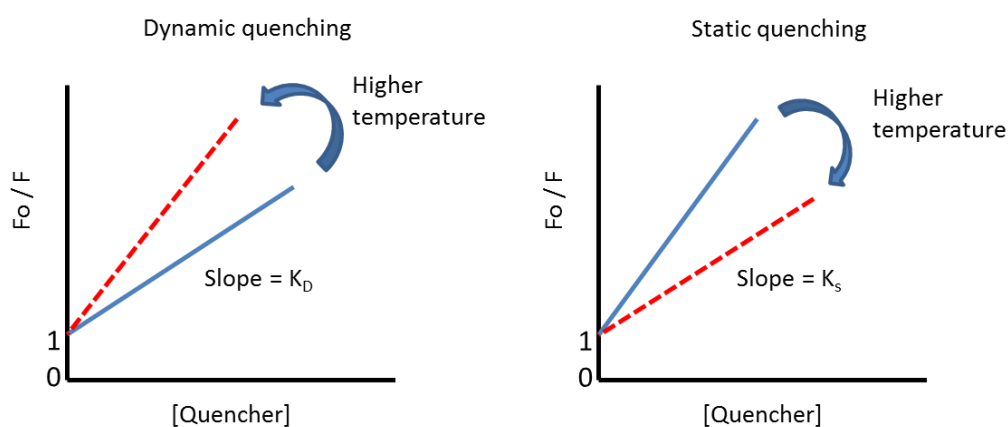


Figure 1.9 Comparison of the temperature sensitivities of dynamic and static quenching processes.

1.3 Fluorescence detection in microfluidic systems

The development of microfluidic devices, also called micro total analysis systems (μ TAS) and lab-on-a-chip systems, has progressed rapidly over almost three decades. The goal in designing and building these systems is not only to reduce the size of the system, but also to enhance the performance of the system. Microfluidic devices provide an ideal platform for point-of-care chemical or biological analysis as they offer several advantages over benchtop laboratory measurements, namely portability, high sample throughput, low reagent/sample consumption, automation, and integration of multiple analytical processes on a chip. In this section, microfluidic systems integrated with fluorescence detection (not only QDs) have been reviewed to provide a general background of the field. However, it is not possible to cite all works

as there are a considerable number of published papers in the field. Recently published articles relevant to the work presented in this dissertation are included here.

A variety of materials can be used as substrates for production of microfluidic chips, including inorganic materials (glass, silicon, ceramics), polymers (elastomers and thermoplastics), and filtration media (cellulosics including paper and nitrocellulose, glass microfiber membranes). The work presented here used several of these materials, separately and in combination, beginning with thermoplastic devices that facilitated fluorescence detection. A brief review of the history of the field puts this and the following studies in context.

Zhang et al.²⁸ developed polydimethyl siloxane (PDMS)-based microfluidic device to support a fluorescence assay for avian influenza virus (AIV), incorporated with immunomagnetic beads forming a reaction zone for AIV preconcentration. A sandwich immunomagnetic assay was performed using the magnetic beads as a solid support. Streptavidin (SA) conjugated QDs were utilized to generate a fluorescence signal for H9N2 virus, which was measured using a portable optical fiber optic spectrometer. The polymer-based open channel microfluidic system required a syringe pump to deliver the solutions flowing inside the channel and required multiple steps including preconcentration, incubation, and rinsing processes.

In our research group, Tennico et al.²⁹ developed an on-chip polymer-based microfluidic sandwich DNA assay. Aptamer functionalized magnetic beads were utilized to capture and preconcentrate the target analyte, while the second aptamer, conjugated to a QD signaling agent, was used to generate an analytical signal measured using a fluorescence microscope. The design utilized magnetic beads that

were trapped in the measurement zone by use of external permanent magnets (and later electromagnets) located beneath a reaction chamber. Each chip contained eight sample chambers enabling multiple analyses to be performed simultaneously. It was demonstrated that the platform could be used for multiplexed applications by using different colors of QDs.

Another class of micro total analysis system is a microfluidic paper-based analytical device (μ PAD), first introduced by the Whitesides group in 2007.³⁰ This class of analytical devices uses cellulose paper as a substrate or solid support for a dry reagent/assay. The hydrophilicity and porosity of paper enable the flow via capillary action. Several fabrication techniques have been utilized on paper-based analytical devices to define hydrophilic areas on the paper that are separated by hydrophobic permeation barriers. The number of available techniques for fabrication of these devices has grown to include wax patterning, inkjet printing, photolithography, chemical modification of the paper, and three-dimensional devices achieved by layering patterned paper components. The advantages of the μ PAD approach include enablement of non-pumped fluid flow, low cost, and high portability – many of these are attributable to the fact that reagents can be stored within the fiber network.

Among the many detection strategies explored for microfluidics, optical detection stands out for its breadth of applicability. In particular, the use of fluorescence detection is attractive because of its high sensitivity; however, one drawback is the high background fluorescence that is often seen from the paper whitening additives present when a cellulosic μ PAD is used. This drawback can be avoided through careful material selection, and by working in regions of emission

that are unaffected by this background fluorescence – for instance, by harnessing fluorescence resonance energy transfer (FRET).

FRET involves the measurement of fluorescence changes at two different wavelengths derived separately from donor and acceptor fluorophores. Kim et al.³¹ developed a paper-based sensor strip containing carbon nanodots (C-dots) conjugated with a rhodamine moiety for the detection of Al^{3+} . The mechanism was based on the Al^{3+} induced ring-opening of rhodamine conjugated C-dots resulting in increased fluorescent intensity at the longer-wavelength emission via FRET. The rhodamine conjugated C-dots were physically adsorbed and dried on cellulose based filter paper. A spot test was performed on the paper dot with fluorescence spectrometer detection.

For biological macromolecules, Li et al.³² demonstrated a FRET based hybridization assay for nucleic acids and proteins. Graphene oxide (GO), a two-dimensional carbon based material having high adsorption capability only to single-stranded DNA, was used as a quencher. Fluorescent labeled single stranded DNA was used as a reporter for specific DNA target and protein. For paper-based detection, GO was prior added on the glass filter membrane, subsequent the introduction of post-mix of DNA probe and target. The formation of double-stranded DNA (dsDNA) or aptamer-protein complex made fluorophore apart from GO, prohibiting the FRET phenomenon. The fluorescence corresponding to the target DNA/protein concentrations was measured using digital image analysis.

Li et al.³³ recently developed a three-dimensional (3D) origami paper-based microfluidic device for selective detection of phycocyanin. CdTe QDs using as fluorophore, were covalently grafted on a filter paper via EDC/NHS chemistry. The

phycocyanin-molecularly imprinted polymers (MIPs) were synthesized as silica shells and immobilized on the top of QDs-paper. In the presence of phycocyanin, a Meisenheimer complex was formed between phycocyanin and amino groups on the QD-loaded paper surface. Photoluminescent energy from the QDs was transferred to the complex resulting in a fluorescence quenching. The origami paper-based device was placed in the solid sample holder of a spectrofluorometer to facilitate the measurement.

Inkjet-printing is another fabrication technique that has been used to generate hydrophobic/hydrophilic patterns on μ PADs, first introduced by the Citterio group.^{34,35} In the same research group, Yamada et al.³⁶ developed an inkjet-printed μ PAD for determination of tear fluid lactoferrin without using costly antibodies. The assay relied on fluorescence emission from a complex between human lactoferrin and terbium (Tb^{3+}), which was printed on the sensing area of the μ PAD. A UV-curable ink (based on octadecyl acrylate and 1,10-decanediol diacrylate) was printed on a filter paper patterning hydrophobic wall to confine an aqueous sample and a TbCl_3 solution was deposited on the sensing area. Two UV handheld lamps (254 nm) were used to excite the fluorescent complex. The emitted green fluorescence was imaged using a digital camera through a long-pass filter to eliminate the light reflected from the paper substrate. Green intensity from an RGB signal output was graphed against lactoferrin concentration ($0.5\text{-}3.0 \text{ mg ml}^{-1}$) and used to demonstrate the quantitative utility of the technique.

Our research group has been developing novel fabrication techniques for microfluidic chips³⁷⁻⁴³ as well as chemical/biological assays on various microfluidic platforms.²⁹ One of the techniques established in our lab is to use polycaprolactone (PCL) as a bonding agent (adhesive) and a hydrophobic sidewall material on a chip.⁴⁴ PCL is a biodegradable thermoplastic polymer with a melting point of nominally 60°C (140°F). Its hydrophobicity and its low melting point enable its use on microfluidic platforms.

In Chapters 2 and 3 of this dissertation, two different approaches are utilized for the production of microfluidic devices. Laser-cut thermoplastic chips are used to facilitate a CdTe QD fluorescence assay for copper quantification, while paper-based microfluidic chips incorporating CdTe QDs are used for cyanide determination in a separate fluorescence assay.

1.4 References

- (1) Brus, L. E. *J. Chem. Phys.* **1984**, *80* (9), 4403–4409.
- (2) Chukwuocha, E. O. *World J. Condens. Matter Phys.* **2012**, *2* (2), 96–100.
- (3) BASIC PHOTOPHYSICS <http://www.photobiology.info/Visser-Rolinski.html> (accessed Dec 1, 2014).
- (4) Shin, S. K.; Yoon, H.; Jung, Y. J.; Park, J. W. *Curr. Opin. Chem. Biol.* **2006**, *10* (5), 423–429.
- (5) Donegá, C. de M. *Chem. Soc. Rev.* **2011**, *40* (3), 1512–1546.
- (6) Murray, C. B.; Norris, D. J.; Bawendi, M. G. *J. Am. Chem. Soc.* **1993**, *115* (19), 8706–8715.
- (7) Peng, X.; Schlamp, M. C.; Kadavanich, A. V.; Alivisatos, A. P. *J. Am. Chem. Soc.* **1997**, *119* (30), 7019–7029.

- (8) Peng, X.; Wickham, J.; Alivisatos, A. P. *J. Am. Chem. Soc.* **1998**, *120* (21), 5343–5344.
- (9) Peng, X.; Manna, L.; Yang, W.; Wickham, J.; Scher, E.; Kadavanich, A.; Alivisatos, A. P. *Nature* **2000**, *404* (6773), 59–61.
- (10) Peng, Z. A.; Peng, X. *J. Am. Chem. Soc.* **2001**, *123* (1), 183–184.
- (11) LaMer, V. K.; Dinegar, R. H. *J. Am. Chem. Soc.* **1950**, *72* (11), 4847–4854.
- (12) Murray, C. B.; Kagan, C. R.; Bawendi, M. G. <http://dx.doi.org/10.1146/annurev.matsci.30.1.545> **2000**, *30*, 545–610.
- (13) Jing, L.; Kershaw, S. V.; Li, Y.; Huang, X.; Li, Y.; Rogach, A. L.; Gao, M. *Chem. Rev.* **2016**, *116* (18), 10623–10730.
- (14) Jeong, S.; Achermann, M.; Nanda, J.; Ivanov, S.; Klimov, V. I.; Hollingsworth, J. A. *J. Am. Chem. Soc.* **2005**, *127* (29), 10126–10127.
- (15) Reiss, P.; Protière, M.; Li, L. *Small* **2009**, *5* (2), 154–168.
- (16) Hines, M. A.; Guyot-Sionnest, P. *J. Phys. Chem.* **1996**, *100* (2), 468–471.
- (17) Kim, S.; Fisher, B.; Eisler, H.-J.; Bawendi, M. *J. Am. Chem. Soc.* **2003**, *125* (38), 11466–11467.
- (18) Gao, X.; He, J.; Deng, L.; Cao, H. *Opt. Mater.* **2009**, *31* (11), 1715–1719.
- (19) Yang, P. In *Integrated Biomaterials for Biomedical Technology*; Ramalingam, M., Tiwari, A., Ramakrishna, S., Kobayashi, H., Eds.; John Wiley & Sons, Inc., 2012; pp 145–252.
- (20) Stöber, W.; Fink, A.; Bohn, E. *J. Colloid Interface Sci.* **1968**, *26* (1), 62–69.
- (21) Li, Z.; Du, Y.; Zhang, Z.; Pang, D. *React. Funct. Polym.* **2003**, *55* (1), 35–43.
- (22) Mansur, H. S.; Mansur, A. A. P.; Curti, E.; Almeida, M. V. D. *J. Mater. Chem. B* **2013**, *1* (12), 1696–1711.
- (23) Kang, B.; Chang, S.-Q.; Dai, Y.-D.; Chen, D. *Radiat. Phys. Chem.* **2008**, *77* (7), 859–863.
- (24) Yuan, C.; Wang, L.; An, Y.; Wu, G.; Zhang, D. *RSC Adv.* **2015**, *5* (37), 29048–29057.

- (25) Dogan, Ü.; Kasap, E.; Cetin, D.; Suludere, Z.; Boyaci, I. H.; Türkyılmaz, C.; Ertas, N.; Tamer, U. *Sens. Actuators B Chem.* **2016**, *233*, 369–378.
- (26) Sharma, A.; Pandey, C. M.; Sumana, G.; Soni, U.; Sapra, S.; Srivastava, A. K.; Chatterjee, T.; Malhotra, B. D. *Biosens. Bioelectron.* **2012**, *38* (1), 107–113.
- (27) *Principles of Fluorescence Spectroscopy*; Lakowicz, J. R., Ed.; Springer US: Boston, MA, 2006.
- (28) Zhang, R.-Q.; Liu, S.-L.; Zhao, W.; Zhang, W.-P.; Yu, X.; Li, Y.; Li, A.-J.; Pang, D.-W.; Zhang, Z.-L. *Anal. Chem.* **2013**, *85* (5), 2645–2651.
- (29) Tennico, Y. H.; Hutanu, D.; Koesdjojo, M. T.; Bartel, C. M.; Remcho, V. T. *Anal. Chem.* **2010**, *82* (13), 5591–5597.
- (30) Martinez, A. W.; Phillips, S. T.; Butte, M. J.; Whitesides, G. M. *Angew. Chem. Int. Ed.* **2007**, *46* (8), 1318–1320.
- (31) Kim, Y.; Jang, G.; Lee, T. S. *ACS Appl. Mater. Interfaces* **2015**, *7* (28), 15649–15657.
- (32) Li, H.; Fang, X.; Cao, H.; Kong, J. *Biosens. Bioelectron.* **2016**, *80*, 79–83.
- (33) Li, B.; Zhang, Z.; Qi, J.; Zhou, N.; Qin, S.; Choo, J.; Chen, L. *ACS Sens.* **2017**.
- (34) Abe, K.; Suzuki, K.; Citterio, D. *Anal. Chem.* **2008**, *80* (18), 6928–6934.
- (35) Yamada, K.; Henares, T. G.; Suzuki, K.; Citterio, D. *Angew. Chem. Int. Ed.* **2015**, *54* (18), 5294–5310.
- (36) Yamada, K.; Takaki, S.; Komuro, N.; Suzuki, K.; Citterio, D. *Analyst* **2014**, *139* (7), 1637–1643.
- (37) Koesdjojo, M. T.; Pengpumkiat, S.; Wu, Y.; Boonloed, A.; Huynh, D.; Remcho, T. P.; Remcho, V. T. *J. Chem. Educ.* **2015**, *92* (4), 737–741.
- (38) Koesdjojo, M. T.; Nammoonoy, J.; Wu, Y.; Frederick, R. T.; Remcho, V. T. *J. Micromechanics Microengineering* **2012**, *22* (11), 115030.
- (39) Koesdjojo, M. T.; Wu, Y.; Boonloed, A.; Dunfield, E. M.; Remcho, V. T. *Talanta* **2014**, *130*, 122–127.
- (40) Koch, C.; Remcho, V.; Ingle, J. *Sens. Actuators B Chem.* **2009**, *135* (2), 664–670.
- (41) Says, S. Simple and rapid fabrication of paper microfluidic devices utilizing Parafilm® – Chips and Tips.

- (42) Tennico, Y. H.; Koesdjojo, M. T.; Kondo, S.; Mandrell, D. T.; Remcho, V. T. *Sens. Actuators B Chem.* **2010**, *143* (2), 799–804.
- (43) Koesdjojo, M. T.; Tennico, Y. H.; Rundel, J. T.; Remcho, V. T. *Sens. Actuators B Chem.* **2008**, *131* (2), 692–697.
- (44) Heist, C. A. Polycaprolactone-based microfluidic devices: fabrication methods and applications in low-cost analytical devices, Oregon State University: Corvallis, OR, 2016.

A Microfluidic Detection System for Quantitation of Copper Incorporating a Wavelength-Ratiometric Fluorescent Quantum dot Pair

Sumate Pengpumkiat; Yuanyuan Wu; Anukul Boonloed; Gayan C. Bandara; and

Vincent T. Remcho

Analytical Methods, 2017 Advance article

DOI: 10.1039/C6AY02718K

Royal Society of Chemistry

1050 Connecticut Ave NW, 10th Floor Washington DC 20036

CHAPTER 2

A MICROFLUIDIC DETECTION SYSTEM FOR QUANTITATION OF COPPER INCORPORATING A WAVELENGTH-RATIOMETRIC FLUORESCENT QUANTUM DOT PAIR**2.1 Abstract**

Described is a new approach to building a microfluidic quantum dot wavelength-ratiometric sensor system for quantifying copper in water and biological samples. This simple-to-use, low-cost, sensitive analytical tool has great utility as an indicator and quantitative tool, and we have applied it here with copper as the target analyte. CdTe quantum dots of two different sizes, emitting green and red light, are utilized as fluorophores. The green dot is used as a constant emitter and is encapsulated in a silica shell. The red dot, which is immobilized on the silica surface, is quenched in the presence of copper. The dual emission of the quantum dot wavelength-ratiometric sensor results in a fluorescence color change from red to green, identified visually, corresponding to the absence or the presence of copper. The wavelength-ratiometric sensor is mixed with microcrystalline cellulose and dropcast on a microfluidic chip, made of poly(methyl methacrylate) and assembled using polycaprolactone. Red and green intensity values from the RGB system are used as analytical signals for the calibration curve. Copper in water samples is quantitatively determined by constructing a Stern-Volmer plot in the range of 1 - 30 mg/L. For serum samples, absolute values of red and green intensity were plotted to mitigate non-linearity in the Stern-Volmer plot. The microfluidic format of this quantum dot wavelength-ratiometric sensor makes rapid, low-cost testing feasible and convenient for copper detection, directly addressing a diagnostic goal.

2.2 Introduction

Copper is an essential trace element for maintaining health and development of humans and animals, and is a key component of various enzymes.¹ These copper-containing enzymes play a crucial role in metabolism. For example, cytochrome c oxidase is a multi-subunit complex that supports energy production at the cellular level; protein-lysine 6-oxidase is a cuproenzyme involved in connective tissue formation; ferroxidase I (ceruloplasmin) is a copper-containing enzyme that functions in iron metabolism. Homeostatic control regulates copper supply in vivo, in response to varying dietary intake. Copper imbalances can generate health problems in both humans and animals. The recommended dietary allowance (RDA) of copper is 0.9 mg/day for adults; at low intakes, copper deficiency disease may be seen. The symptoms include fatigue, arthritis, osteoporosis, paleness, low body temperature. At higher intakes, copper toxicity may result.; here, symptoms include metallic taste, nausea, vomiting, diarrhea, jaundice, hemoglobinuria, liver damage, kidney failure, potentially death.²

Acute copper poisoning is occasionally found due to contamination of food from copper-containing vessels and water supplies.² Guideline values for safe drinking water have been set by the US Environmental Protection Agency (1.3 mg Cu/L) and World Health Organization (2.0 mg Cu/L).³ In clinical diagnostic settings, copper test results must be evaluated in context and are normally compared to a patients' ceruloplasmin level. Abnormal copper test results trigger further investigation. Normal copper concentration in humans is usually in the interval of 70 – 140 µg/dL.⁴

In veterinary medicine, acute and chronic copper poisoning is found with some regularity in most parts of the world. Sheep and dogs are affected most often; other species are susceptible as well. Copper has been used as a feed additive for pigs at 125-250 ppm^{5,6} to promote rapid growth. Enhancing the absorption and retention of copper alters its metabolism, potentially leading to chronic poisoning. Blood and liver copper concentrations are elevated during the hemolytic period, often rise to 5-20 µg/mL, as compared with normal levels of about 1 µg/mL.⁵ Measurements of the trace element concentration in both environmental settings and biological specimens are helpful in nutritional assessment and disease monitoring.

Conventional methods for trace metal analysis include atomic absorption spectroscopy (AAS), inductively coupled plasma optical emission spectrometry (ICP-OES), and inductively coupled plasma-mass spectrometry (ICP-MS). These methods require relatively costly, comparatively sophisticated instrumentation, a skilled technician, and are available only in the central laboratory setting.

Several additional analytical techniques have been developed for copper detection, including electrochemical^{7,8} and colorimetric methods.⁹⁻¹¹ Several chromogens are available to form complexes with copper ions, such as diethyldithiocarbamate, bis-cyclohexanone, oxaldihydrazone (cuprizone), bathocuproine; however, they are not specific for a particular metal. Recently, copper ion was quantitatively determined in serum samples by using specific prion protein immobilized on a field effect transistor (FET) gate.¹² The method provides low concentration detection capability (0-100 nM) for examination of Cu²⁺ deficiency, but

this approach required that a selective Cu^{2+} binding protein be immobilized on the FET surface. It was time consuming, expensive, and involved multi-stage processes.

Semiconductor nanocrystals, or quantum dots, are inorganic fluorophores that exhibit a strong quantum confinement effect. They have unique, extraordinary properties; namely, high molar absorptivity, high fluorescence quantum yield, broad excitation spectra, narrow tunable emission wavelength, and resistance to photobleaching. Their applications have been widely explored in a variety of fields due to their remarkable optical properties. Applications include bioimaging, chemical/biosensors, light emitting diodes, and solar cells. In the field of chemical sensors, CdSe,¹³ CdTe,¹⁴ and CdTe/ZnS¹⁵ quantum dots have been utilized as fluorescence probes to detect copper ions. The methods are based on the measurement of a single effect, fluorescence quenching, which is subject to interferences arising from probe concentration variation and environmental conditions (such as pH, temperature, and solvent polarity). While attractive, this approach is not formatted for quantitative applications to field samples, all assays are conducted using liquid phase reagents, the QDs are not immobilized to prevent their loss in whole or in part, and the assay is not rendered in a field-portable format. In the work presented here, this weakness is addressed through measurement of two different QD fluorescence signals, or QD wavelength-ratiometric detection. The term “wavelength-ratiometric” is defined as *the simultaneous measurement of two fluorescence signals at the different wavelengths, only one of which is directly affected by analyte concentration, followed by calculation of their intensity ratio*; this approach provide built-in signal correction to account for variability in dosing of the device or sample

with quantum dot sensor. It is not limited to the scenario of having one species decrease while the other species increase (correlation).¹⁶⁻²⁵ This technique directly mitigates these adverse effects and promotes demonstrable precision; in addition, the observed color change enables simple visual identification.²¹

Digital image analysis, the extraction of meaningful information from images, is another field that has seen explosive growth. In RGB color space, all colors are represented as combinations of red, green, and blue (RGB). R, G & B are each represented in 8 bits, having integer values from 0 to 255. Our research group and others²⁶⁻³¹ have made efforts to incorporate digital image analysis as a tool for colorimetric detection. Several detection systems have been successfully developed for different analytes, such as artesunate,³² dual detection of copper and iron,³³ and determination of bromide in water as a proxy for contamination arising from hydraulic fracturing.³⁴ Image analysis makes possible easy-to-use, inexpensive, and rapid detection on a microfluidic chip platform.

In this work, we built a quantum dot wavelength-ratiometric sensor for copper detection and transferred the assay to a microfluidic chip format. CdTe QD with green emission at 530 nm (QD530) was encapsulated inside a silica shell and used as a constant green emitter. CdTe/CdS QD with red emission at 650 nm (QD650) was conjugated on the silica surface for sensing the presence of copper ion in the samples. Copper ion specifically quenched the red QD while the protected green QD (being embedded in the system prior to its use) continued to emit, resulting in a perceived color change from red to green corresponding to increasing copper concentration. Taking advantage of visual observations of bright fluorescence emissions from the

QD wavelength-ratiometric sensor on a microfluidic chip, digital image analysis (RGB values) were used to quantitatively determine the concentration of copper. No fluorescence spectrometer was needed to quantitate the copper concentration. Color intensity from a single RGB color system replaced the need to measure fluorescence intensity. Fluorescent emissions at 650 nm and 530 nm were recorded as measured red and green values in the RGB color system. The wavelength-ratiometric sensor was successfully transferred to a microfluidic chip, offering high sample throughput, portability, and low-cost detection. The microfluidic wavelength-ratiometric QD sensor was applied to analysis of water samples as well as complex biological samples, serum samples, for copper poisoning determinations. Digital image analysis using RGB values as proxies for luminescence of quantum dots paves a new path for QD sensing on a microfluidic chip.

2.3 Materials and methods

2.3.1 Materials

All the chemicals used were of analytical-reagent grade. Deionized water was obtained from a Milli-Q® Advantage A10. CdCl₂ (anhydrous, 99%), tellurium powder (~200 mesh, 99.8%), 3-mercaptopropionic acid (MPA, 99%), Sodium borohydride (NaBH₄, 98%), thiourea (99%), tetraethyl orthosilicate (TEOS, 99%), (3-aminopropyl) triethoxysilane (APTES, 99%), polyvinylpyrrolidone (PVP, Mw = 40 000 g/mol), poly(ethylene glycol) (PEG, Mw = 3350 g/mol), polycaprolactone (PCL, Mw = 70 000 – 90 000 g/mol), 2-(N-morpholino)ethanesulfonic acid (MES) were purchased from Sigma-Aldrich (St. Louis, MO, USA). Microcrystalline cellulose was purchased from Alfa Aesar (Ward Hill, MA, USA). Copper sulfate (CuSO₄) was

purchased from Fisher Chemical (Fair Lawn, NJ, USA). Zinc sulfate (ZnSO_4) was purchased from Flinn Scientific (Batavia, IL, USA). Fetal bovine serum (FBS, non-USA origin, from USDA approved countries, heat inactivated, sterile filtered) was used to represent a serum sample in this study.

2.3.2 Synthesis of CdTe quantum dots

CdTe Quantum dots were synthesized in aqueous solution following a previously reported method with some modifications.³⁵ 1 mmol anhydrous CdCl_2 (0.1883 g) and 2.5 mmol 3-mercaptopropionic acid (217 μL) were mixed in 100 mL of Milli-Q water. The pH of the solution was adjusted to 9 using 1.0 M NaOH. The solution became milky on addition of the NaOH solution, and became clear when nearing pH 9. The mixture was purged with N_2 gas for 30 min to eliminate oxygen from solution. The NaHTe solution was prepared separately by mixing 0.5 mmol tellurium powder (63.8 mg) and 5 mmol NaBH_4 (0.1892 g) in 5 mL Milli-Q water. Tellurium powder was slowly reduced by NaBH_4 to form a purple solution of NaHTe. The NaHTe precursor was added to the cadmium precursor solution and the mixture was refluxed at 95-100°C. The final molar ratio of Cd^{2+} /MPA/NaHTe was 1:2.5:0.5, respectively. The reflux time was varied to grow the nanoparticles (4 hours = green to 78 hours = red). The emission wavelengths of the nanoparticles were monitored using a fluorescence plate reader with the excitation wavelength set at 365 nm. CdTe quantum dots with an emission wavelength of 530 nm (QD530) were further encapsulated in a silica shell while the CdTe QDs with emission wavelength > 570

nm were purified by precipitation with isopropanol and dried to obtain a solid powder.

2.3.3 Synthesis of CdTe/CdS core/shell quantum dots

CdTe/CdS core/shell QDs were synthesized in aqueous solution following a procedure described elsewhere^{36,37} with some modifications. Briefly, 80 mL of purified CdTe QD core (1 mg/mL; emission wavelength > 570 nm), suspended in Milli-Q water, was mixed with 20 mL of CdCl₂ solution (30mM) and 131 μL MPA. The solution was adjusted to pH 11 using 1 M NaOH. The mixture solution was purged with N₂ for 30 min and then 20 mL of thiourea (30 mM) (a sulfur precursor) was added to the mixture. The molar ratio of CdS shell Cd²⁺/MPA/S²⁻ as 1:2.5:1. The solution was refluxed at 95-100°C to grow a CdS shell on the CdTe core. The reaction was tracked by monitoring the maximum emission peak of the CdTe/CdS core/shell to longer wavelengths (red shift). A maximum emission wavelength of 650 nm was obtained after the reaction was carried out for 12 hours.

2.3.4 Silica encapsulation of CdTe Quantum dots

CdTe QDs with a maximum emission of 530 nm (QD530) were cladded with silica following a modified Stober method.³⁸ Briefly: 200 mL of ethanol, 56 mL of Milli-Q water, 8 mL of QD530 and 1.6 mL of ammonium hydroxide (28%) were mixed in an HDPE bottle with stirring. 0.8 mL of tetraethyl orthosilicate (TEOS), a silica precursor, was then added to the mixture. The reaction was stirred for 2 hours for hydrolysis and condensation of TEOS. The solution became turbid indicating the

formation of the silica nanoparticles. The silica nanoparticles were aminated by adding 0.4 mL of (3-aminopropyl)triethoxysilane (APTES) to the suspension. The suspension was continuously stirred overnight. The QD encapsulated silica nanoparticles were washed with ethanol and water (3x) to remove the excess/unreacted reagents. The resulting QD530@SiO₂ was suspended in 20 mL of Milli-Q water for further use.

2.3.5 Assembly of the ratiometric sensor

The dual emission ratiometric sensor was synthesized by conjugating the QD530@SiO₂ with QD650. The objective was to optimize the red/green emission ratio of the sensor. The amount of QD650 was varied in such a way that when the QD650 was quenched by copper, the green emission from QD530 inside the silica shell would dominate, resulting in only green emission. In the experiment, 6.25 mL of QD650 was mixed with 20 mL of MES buffer (0.1 M, pH 6.0) and 4 mL of EDC/NHS (10 mg/mL and 5 mg/mL). Carboxyl groups on the QD surface were activated to form the amine-reactive NHS ester. Amine-terminated QD530@SiO₂ from the previous step was added to the mixture and reacted overnight. The conjugate was washed with Milli-Q water (3x) and stored in 20 mL Milli-Q water (concentration 13.5 mg/mL). The prepared, ready-to-use wavelength- ratiometric sensor was stored at 4°C and remained fully viable for 1 year.

2.3.6 Microfluidic chip design

The microfluidic chip was drawn and designed using SolidWorks® 2013 (Dassault Systèmes, Waltham, MA, USA). The design (Figure 2.1) contained a sample introduction zone for applying the liquid samples and a detection zone in which the QD ratiometric sensor was deposited. One chip contains ten individual channels for ten different samples. The diameters of the introduction and detection zones were 4 mm. The distance between the two zones was 3.63 mm.

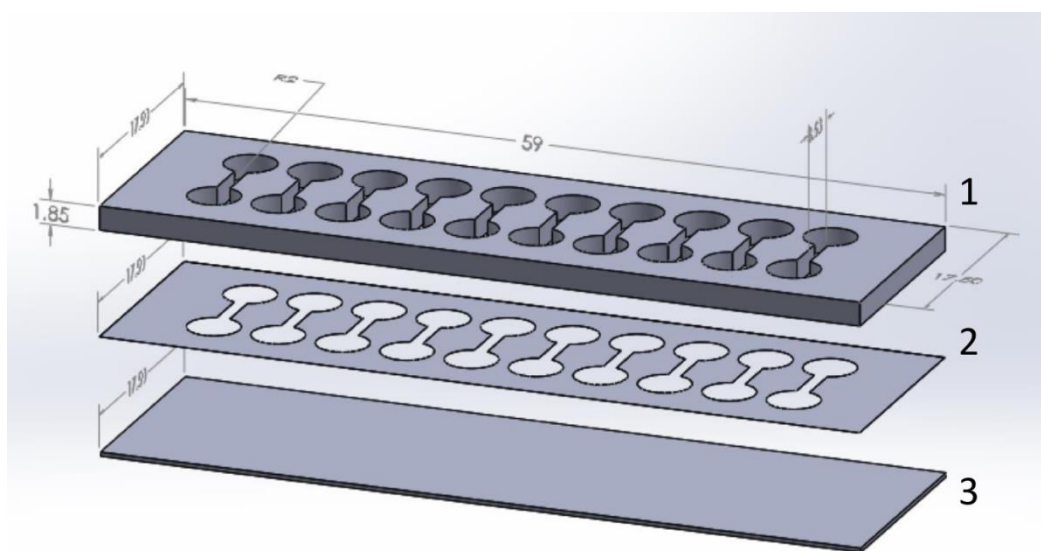


Figure 2.1 Microfluidic chip design and detection system for color measurement using a QD ratiometric sensor. (a) 1: the polymethyl methacrylate (PMMA) fluidic patterned layer was cut using a laser cutter; 2: a thin film of polycaprolactone (PCL, 5% solution in toluene) was sprayed onto the PMMA layer to serve as a bonding layer; 3: a polycarbonate layer was used as a base. All layers were assembled using a hot press (Carver model 3851-0, Carver, Inc., Wabash, IN, USA) at 60°C, 300 psi for 10 minutes.

2.3.7 Deposition of QD ratiometric sensor on a chip

Microcrystalline cellulose was used as a material to absorb the liquid samples and support the QD ratiometric sensor. 5 g of cellulose powder was well mixed with 20 mL of 0.1 M Zn^{2+} in Tris-base buffer (0.1 M, pH 8.5). Thirty microliters of the

mixture was dropcast on the sample introduction zone, and the chip was dried in a vacuum oven for 1 hour. The introduction zone allowed for the sample move slowly (*via* capillary action) to the detection zone, which offered the advantage of pre-adjustment of sample pH, and ensured that the detection zone surface remained smooth. For the detection zone, microcrystalline cellulose in 0.1 M Zn^{2+} /Tris-base buffer solution was mixed with 5 mL of the QD wavelength-ratiometric sensor. Eighteen microliters of the mixture was dropcast on each of the detection zones and the chip was again dried in a vacuum oven for 1 hour. As this semiconductor nanocrystal based assay is performed in the microfluidic chip format, very little Cd is required to enable the sensor (18 μL of a diluted QD probe in microcrystalline cellulose and buffer solution). The exposure hazard is exceedingly small, though, the low amount of waste should of course be handled with due care.

2.3.8 Quantitation of copper ion on a chip

Standards/samples were applied directly to the introduction zone. The liquid sample flowed rapidly through the channel and reached the detection zone, where the QD wavelength-ratiometric sensor was spotted. The color developed while an inexpensive external UV light source (365 nm; Compact UV lamps, UVGL-25, UVP, Upland, CA, USA) was used to excite the QD sensors on the chip. To generate a calibration curve for copper in water and serum samples, copper standards were prepared in the range of 0-30 ppm and applied on a chip. Color measurements were made by collecting images using a low-cost, consumer-grade digital camera (Nikon, CoolPix S9300, 16MP, CMOS sensor, Nikon Inc., Melville, NY, USA) with an under exposure of -2 steps. The color generated in each of the detection zones on each chip

was analyzed using ImageJ software, version 1.50b (National Institutes of Health, USA). RGB color intensities were collected and used to plot a calibration graph.

2.4 Results and discussion

2.4.1 Characterization of CdTe QDs and CdTe/CdS core/shell QDs

Water-soluble CdTe quantum dots and CdTe/CdS core/shell quantum dots were synthesized in aqueous solution with mercaptopropionic acid as a capping agent. Green CdTe QDs were obtained by refluxing the mixture for 4 hours. Red CdTe/CdS core/shell QDs were achieved by cladding CdTe core with CdS QD for 2 hours. The absorption and emission spectra of the two color QD pair is shown in Figure 2.2.

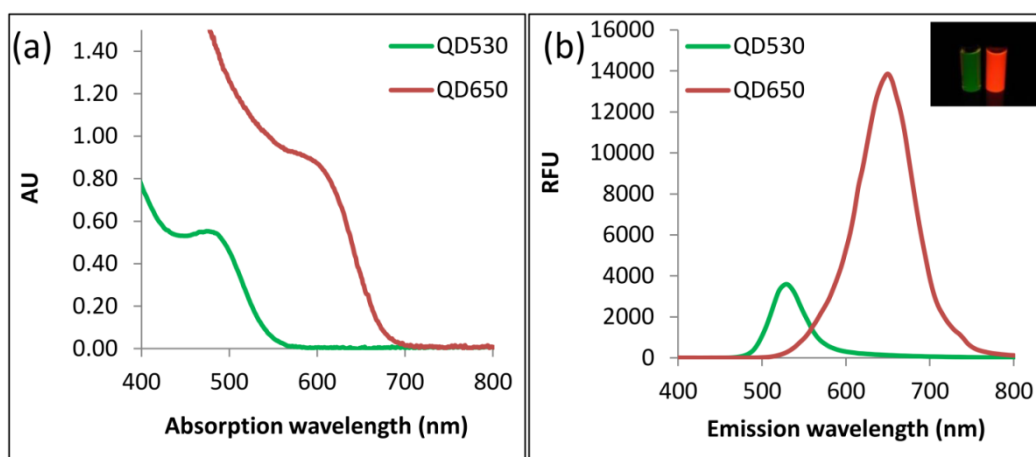


Figure 2.2 a) Absorption spectra of QD530 (green) and QD650 (red) b) Fluorescence emission spectra of QD530 and QD650. Inset image shows the solutions of QD530 and QD650, respectively, under UV light (365nm).

The absorption spectra of the quantum dots showed a first excitonic absorption peak which corresponded to the particle diameters, extinction coefficients and molar concentrations of the QDs. The diameters of the as-prepared QD530 and QD650 were 1.44 and 3.75 nm, respectively (calculated values).³⁹ The molar concentrations of QD530 and QD650 were 253 μM and 4.96 μM , respectively.

Quantum yields of the QDs were determined by comparison to Rhodamine B, which has a quantum yield of 0.31 (in water).⁴⁰ Quantum yields for QD530 and QD650 were 0.039 and 0.169, respectively. The core/shell structure of the red QD helped to improve the quantum yield of the product.

2.4.2 Characterization of the QD ratiometric sensor and optimization of the QD530/QD650 ratio

A quantum dot wavelength-ratiometric sensor was synthesized in order to yield dual emission of 530 nm (green) and 650 nm (red). The QD530 was protected by a silica layer and provided constant green emission for the purpose of signal correction (having been embedded in the system prior to sample application). QD650 was attached to the silica cladding and used as an analytical signal for copper detection. The QD650 was quenched in the presence of copper, while the green emission remained constant. This resulted in a color change from red to green corresponding to the concentration of copper ion in the sample.

In order to maximize the sensitivity of the method, the fluorescent signal ratio (red/green) was optimized for each of the end applications studied, as detailed further below, based on the extent of quenching of the red signal. In these experiments, the volume of QD650 solution added to the QD650/QD530 mixture was varied in the range from 1.25 to 6.25 mL (as prepared) while the volume of the QD530@SiO₂ solution was kept constant.

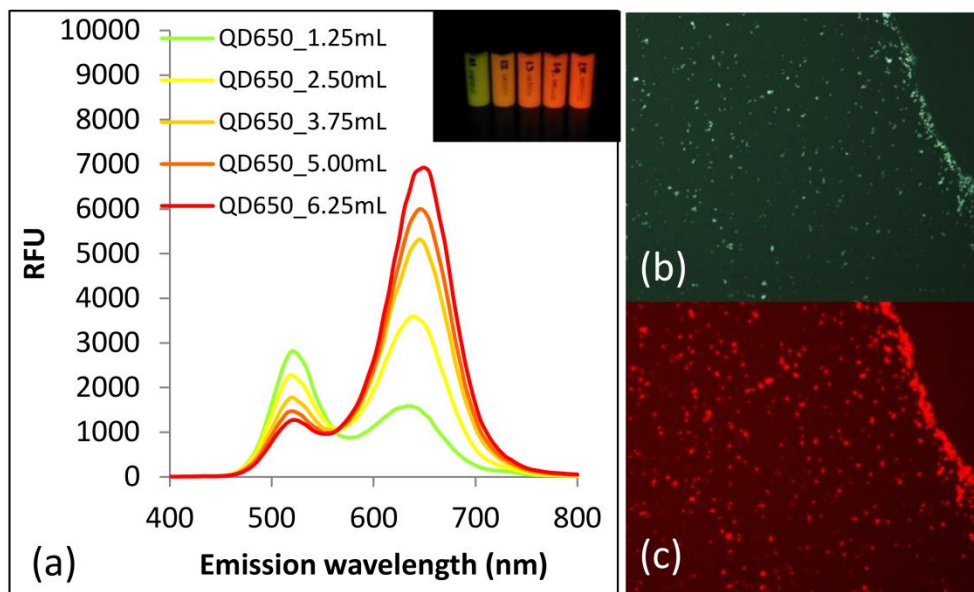


Figure 2.3 a) Spectra of QD ratiometric sensors prepared by varying the relative amounts of QD650 and QD530 to optimize the relative red/green fluorescence signal. Inset picture shows the solutions corresponding to the addition of QD650 solution volumes ranging from 1.25 to 6.25 mL (left to right) b) Fluorescence image of the QD ratiometric sensor visualized by a Zeiss Axio Imager M1m microscope (Thornwood, NY, USA) equipped with Qdot® 525 filter cube, magnification 50X. c) Fluorescence image of QD ratiometric sensor at the same area as (b), using a Qdot® 655 filter cube.

The spectra of the ratiometric sensor showed two emission maxima, as expected: one at 530 nm and one at 650 nm, arising from QD530 and QD650, respectively. When the fluorescence intensity of the red emission was higher than the intensity of the green emission, the solutions exhibited a red coloration. With decreasing red fluorescence emission, the green emission dominated and green coloration dominated. Optimal sensitivity was obtained with the 6.25 mL QD650 solution volume, thus this relative QD650/QD530 ratio was selected for use in all ensuing experiments.

The dual emission wavelength-ratiometric sensor was characterized by fluorescence microscopy. The fluorescence image in Figure 2.3(b) was obtained using

a Qdot®525 filter cube with 50X magnification, and portrays the individual silica nanoparticles loaded with QD530. Figure 2.3(c), obtained using the Qdot®655 filter cube with the same area and magnification, shows the QD655 on the silica nanoparticle surface. The red individual dots (Figure 2.3(c)) were bigger than the green individual dots (Figure 2.3(b)), suggesting that QD530 was indeed encapsulated inside the silica shell and that the QD650 was on the silica nanoparticle surface as intended.

The sensor probes were also characterized by scanning electron microscopy (FEI Quanta 600F Environmental SEM, FEI CO., Hillsboro OR, USA) (Figure 2.4). The particle size of the silica-clad QDs was in the range of 200 – 300 nm. It can be clearly seen that after conjugation of QD650 on the silica nanoparticles, the topography of the dual QD sensor is more rough (Figure 2.4b) than for the un-decorated silica nanoparticles (Figure 2.4a).

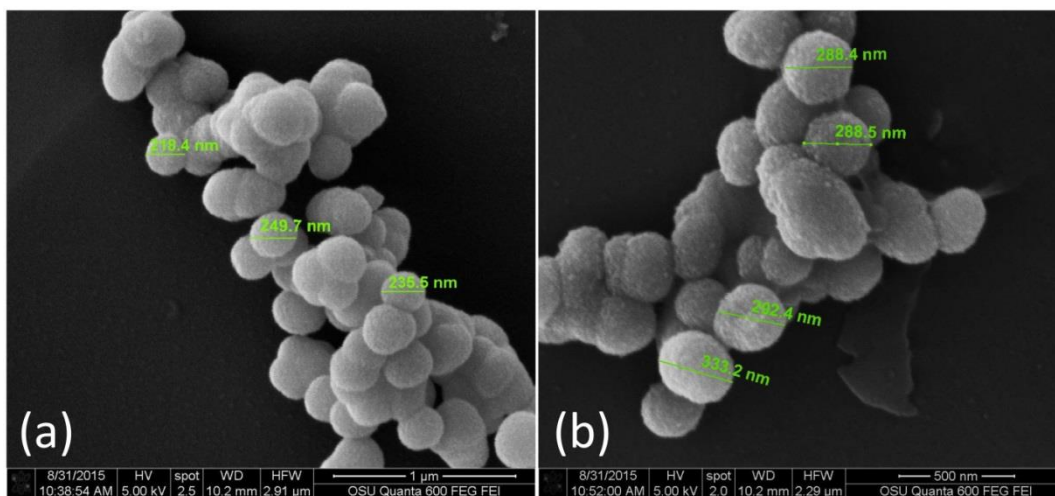


Figure 2.4 Scanning electron microscope images. a) QD530 encapsulated silica nanoparticles (QD530@SiO₂). b) QD650 attached on the QD530@SiO₂ surfaces.

2.4.3 Detection mechanism and Stern-Volmer calibration plot

Detection and quantification of copper using the CdTe/CdS quantum dot sensor is based on fluorescence quenching.⁴¹ The proposed mechanism for quenching suggests that copper ions in the sample solution strongly bind to the quantum dot surface, followed by photoinduced reduction of Cu^{2+} to Cu^+ , which in turn displaces surface Cd^{2+} ions on the QD.^{42,43}

This is a static fluorescence quenching mechanism,¹⁶ which is dependent on the formation of a nonfluorescent ground-state complex between the fluorophore and quencher, which in this case is copper. The well-known equation used to quantify the extent of static fluorescence quenching is the Stern-Volmer equation¹⁶:

$$\frac{F_o}{F} = 1 + K_s[Q]$$

where K_s is a quenching constant or association constant for binding; F_o and F are the fluorescent intensity of QD in a copper-free solution (blank) and at a given Cu^{2+} concentration. A Stern-Volmer plot of our data showed a linear relationship between F_o/F and copper concentration $[Q]$.

We used digital image analysis as a tool for quantitative analysis, rather than a benchtop spectrofluorometer or plate reader, in order to demonstrate the field portability of our approach. To achieve these measurements, the fluorescence intensity values at 530 nm and 650 nm were replaced by green (G) and red (R) channel RGB data. The ratios of red to green values were used as analytical signals in the Stern-Volmer equation:

$$\frac{[R/G]_o}{[R/G]} = 1 + K_s[Q]$$

By plotting $\frac{[R/G]_0}{[R/G]}$ vs. copper concentration $[Q]$, a linear relationship was obtained with an intercept of 1 (see Figure 2.8, which is further addressed later in the text). This equation was further used to quantitate copper in water samples.

2.4.4 Measurement of copper in water samples and assay optimization

The ultimate goals of this project were to measure copper concentrations in environmental water samples and in biological serum samples on a microfluidic chip. In preliminary experiments, the dual QD probe was successfully tested with copper solutions in a liquid phase assay (data not shown) by measuring the fluorescence intensity ratio between QD650 and QD530. This initial work was informed by the previous work of Yao *et al.*²¹ In pursuing this approach, we found that our as-prepared QD wavelength-ratiometric probe was too high in concentration to react with trace copper ion and generate a measurable analytical signal. For this reason, we introduced a solid support for the dual probe, namely microcrystalline cellulose or cellulose powder.

Microcrystalline cellulose performed the roles of supporting the QD wavelength-ratiometric sensor in the microfluidic chip format, diluting the mass concentration of the QD wavelength-ratiometric probe, enhancing absorption of the liquid sample, and facilitating sample transport by capillary action from the sample introduction zone to the detection zone. A negative feature of microcrystalline cellulose in this application, though, is its capacity to adsorb metal ions.⁴⁴⁻⁴⁸ To address this issue, we introduced another, non-interfering, metal ion to saturate the microcrystalline cellulose. Zinc was chosen due to the fact that zinc has the same

charge and a similar ionic radius to copper; however, Zn^{2+} does not interfere with detection because of its higher solubility product ($K_{sp} = 2 \times 10^{-25}$).⁴⁹

Photoluminescence of quantum dots can vary with pH, depending on the types of stabilizing agents used.⁵⁰ In the study, we maintained the pH of the wavelength-ratiometric sensor using Tris-base buffer (0.1M, pH 8.5) during preparation of the devices in order to conserve the photoluminescence of the probe. We found that without the use of this buffer during device assembly, the wavelength-ratiometric sensor, when later used, was susceptible to fluorescence instability.

2.4.5 Assay specificity of QD ratiometric probe

The specificity of the assay was evaluated over the range of relevant cations that would generally be found in environmental waters and/or serum samples. These cations included Mg^{2+} , Ca^{2+} , Fe^{3+} , Zn^{2+} , Mn^{2+} , Cd^{2+} at the concentration level of 5 mg/L. (Figure 2.5)

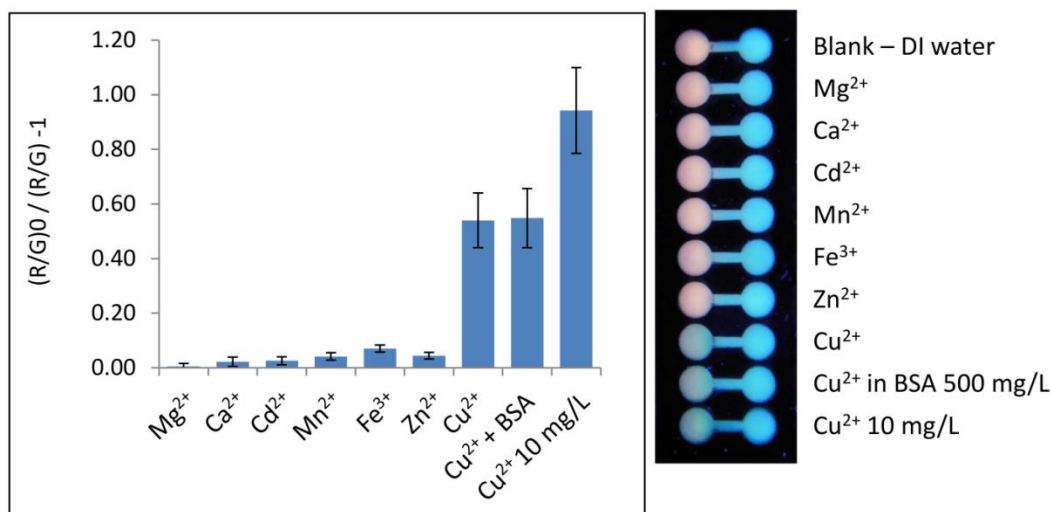


Figure 2.5 The assay specificity of a microfluidic ratiometric probe to various cations generally found in environmental waters and serum samples. (n=6)

Bearing in mind the static quenching model described earlier, we further considered the potential interfering cations. The solubility product (K_{sp}) values for each of the potential interferent metal sulphides having values greater than that of Cu_2S ($K_{sp} = 3 \times 10^{-49}$)⁴⁹ suggest that these metal ions would not quench the luminescent signals of the ratiometric probe, which is in keeping with the experimental results. With this model, slight but measurable fluorescence quenching would be expected for iron (Fe^{3+}), as was seen experimentally; however, this was quite low and therefore did not excessively interfere with the analytical signal for copper. Furthermore, the presence of bovine serum albumin (BSA) at 500 mg/L, the sensor showed the same response as was seen for solutions containing copper alone; this indicated that low amounts of protein (500 mg/L) did not produce sufficient background signal to interfere with the signal attributable to copper. This microfluidic approach to wavelength-ratiometric fluorescence detection of copper proved to be quite specific to copper with minimal interferences.

2.4.6 Reaction time for color development

The optimum reaction time for the introduction of copper standards/samples on a chip was evaluated in the reaction time range of 0 to 60 min (sample size = 30 μL ; Figure 2.6). After application of the copper standards to the chip, color development was immediately noted. The slope of the calibration curve expresses the association constant of Cu^{2+} on the QD650 surface and also reflects the sensitivity of the detection method. The sensitivity increased (from 0.0769 to 0.168) in moving from 1 minute reaction time to 5 minute. In general, sensitivity increased with

reaction time; however, the linear range was concomitantly reduced. A reaction time of 20 min was found to be optimal, as it yielded the highest sensitivity and broadest linear range, with an $R^2 > 0.995$, though shorter reaction times did generate useful and reliable data. This suggests that devices could be tailored specifically to particular applications (environmental and biological) to affect the best compromise between sensitivity, dynamic range, and time-to-data.

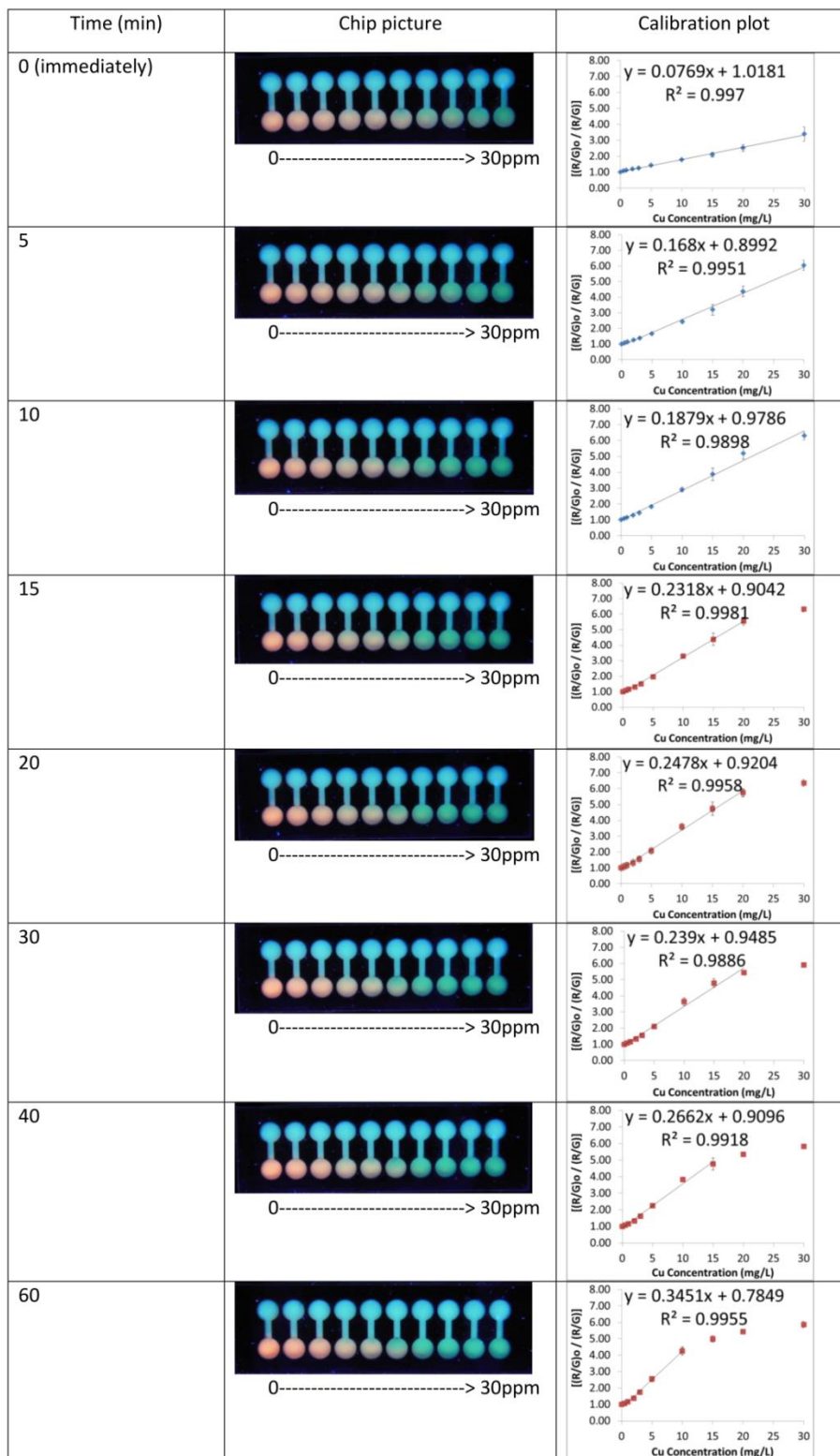


Figure 2.6. Effect of reaction time on sensitivity and linearity of the calibration curve (n=5, sample size = 30 μ L).

2.4.7 Calibration of devices for application to environmental water samples

When the copper standards (0 – 30 mg/L) were applied to the microfluidic chip and a single UV emitter at 365 nm was used as an excitation source, the fluorescence signals for QD650 (red) were quenched, while the fluorescence signals for QD530 (green) remained constant (Figure 2.7). In order to determine concentration of an unknown, each detection well was evaluated for red and green intensity values using ImageJ. Average values for the entire sampling area were determined and then graphed as a Stern-Volmer plot.

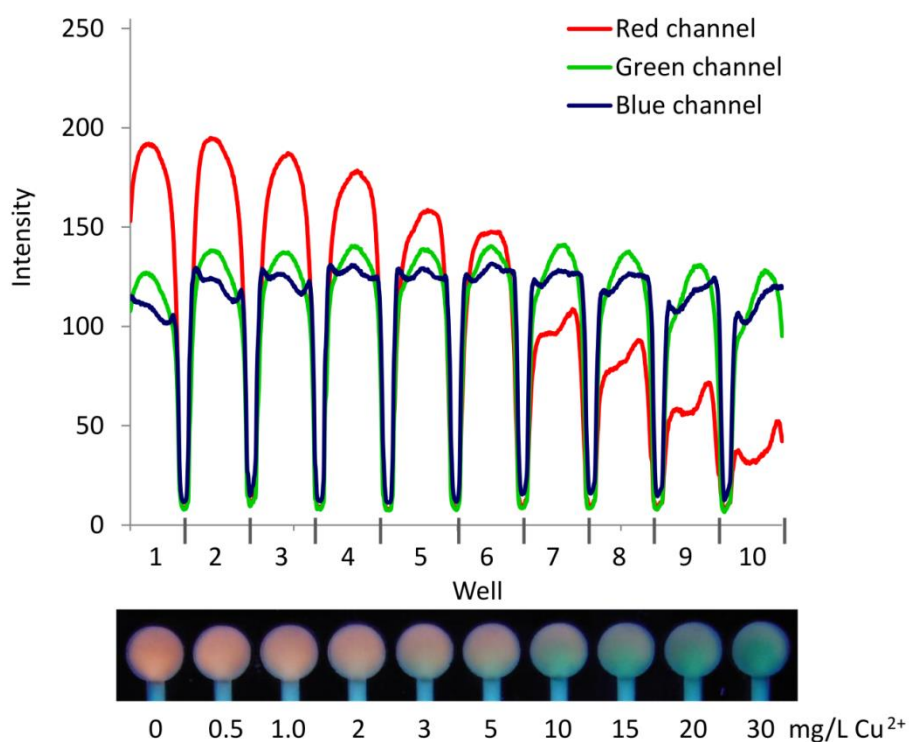


Figure 2.7 RGB profile plot for a microfluidic QD ratiometric sensor after application of copper standards in the range of 0 to 30 mg/L (left to right). (Sample size 20 μ L, reaction time 20 min) The profile plot was obtained using ImageJ software -> plugins -> Graphics -> RGB profile plot.

A calibration curve for Cu²⁺ detection in water samples was established, building on the encouraging results from the initial ImageJ data. The data for

calibration curves was collected both within-day and between-days (4 days; n=34). The calibration plot was generated using the entire data pool and was quite linear; $y = 0.0969x + 0.9944$ ($R^2 = 0.9989$) (Figure 2.8). As the quantum dot quenching mechanism is not spontaneous, the color developed with time. A data set comprised of five separate samples evaluated on five different microfluidic chips was collected simultaneously to plot a calibration graph. The time required to place each chip in the measurement window, collect an image, and cycle to the next chip – the “collection time” – affected the standard deviation of the data points. For this reason, the error bars systematically increased in magnitude with increasing copper concentrations (see Figure 2.6). While this is not a barrier to effective use of the measurement tool, this minor but measurable temporal sensitivity bears mention.

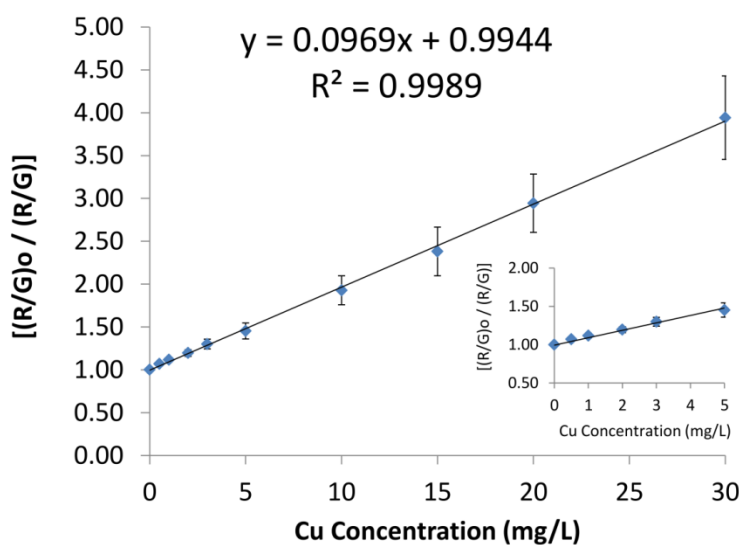


Figure 2.8 calibration curve derived from the Stern-Volmer plot for microfluidic copper detection in water samples. (n=34, sample size= 20 μ L, reaction time= 20 min).

Limit of detection (LOD) and limit of quantification (LOQ) were determined using the International Union of Pure and Applied Chemistry (IUPAC) definitions⁵¹ by incrementally fortifying a Cu^{2+} standard prepared in Milli-Q water at low concentration (0.5 mg/L; n=27) and calculating standard deviations at each fortification level. LOD and LOQ were 0.24 mg/L and 0.81 mg/L, respectively. Furthermore, we tested the accuracy and precision of the detection system by measuring recovery at three concentration levels; low (2 mg/L), medium (5 mg/L), and high (20 mg/L) over the calibration curve (Table 1). At low concentration (2 mg/L), the %RSD was larger than that of high concentration (20 mg/L). The microfluidic detection system showed high accuracy with recovery more than 92% (the acceptable recovery levels recommended by the Association of Official Analytical Chemists (AOAC) International are in the range of 80-115% at the 10 ppm concentration level).

Table 2.1 Recovery test of microfluidic copper detection in water samples. (n=18)

Add (mg/L)	Found			% Recovery	
	(mg/L)	SD	RSD	Value	SD
2	1.94	0.40	20.61	96.77	20.17
5	4.61	0.85	18.44	92.12	13.83
20	19.47	2.16	11.09	97.36	10.80

2.4.8 Measurement of copper in serum samples

It is challenging to measure copper in the presence of high concentrations of protein (such as in serum samples; 3.0–4.5 g/dL) as Cu^{2+} binds strongly to many proteins including albumin and ceruloplasmin. Copper has an intrinsic affinity

constant on the order of 10^{11} M^{-1} for the BSA-Cu²⁺ complex.⁵² Bearing that in mind, we explored the application of our microfluidic QD wavelength-ratiometric measurement device to copper poisoning determination. Blood copper concentration can reach levels as high as 5 – 20 mg/L in animals, establishing that as our upper limit of application.⁵

Fetal Bovine Serum (FBS) from Sigma-Aldrich (Product No. 12306C) was utilized as a blank serum sample in this study. Copper standards were prepared over a range of relevant concentrations (0, 1, 2, 5, 10, 15, 20, 30 mg/L) in serum samples. The copper-fortified serum samples were applied to the QD microfluidic chip following some modification to facilitate simpler use and a more relevant concentration sensitivity. First, the ratio of the volume of as-prepared QD ratiometric probe to the mass of microcrystalline cellulose was reduced to 3 mL of probe solution per 5 grams of cellulose powder. Second, water-soluble polymers, namely polyvinylpyrrolidone (PVP, $M_w = 40\,000 \text{ g}\cdot\text{mol}^{-1}$) and poly(ethylene glycol) (PEG, $M_w = 3350 \text{ g}\cdot\text{mol}^{-1}$) were added to the cellulose slurry at concentrations of 3% and 1%, respectively. The polymers made the microfluidic channel more hydrophobic, while ensuring sufficient hydrophilicity to support transport of the serum samples. These changes ensured that we met the objectives of (1) increased sensitivity, and (2) minimized extent of adsorption of the protein-Cu²⁺ complex on the cellulose filled microfluidic channel.

Our study found that the Stern-Volmer plot from the copper-fortified serum sample yielded a non-linear calibration graph (Figure 2.9) This result was in agreement with a previous report, in which BSA-stabilized CdSe/ZnS core/shell

particles were used for metal binding.⁵³ The non-linearity in the Stern-Volmer plot for the serum sample is a result of the high concentration of protein in this sample (specification: 3-4.5 g/dL). Very high concentrations of protein in the serum depleted the copper concentrations (Cu^{2+} /protein binding) and competed with the detection mechanism.

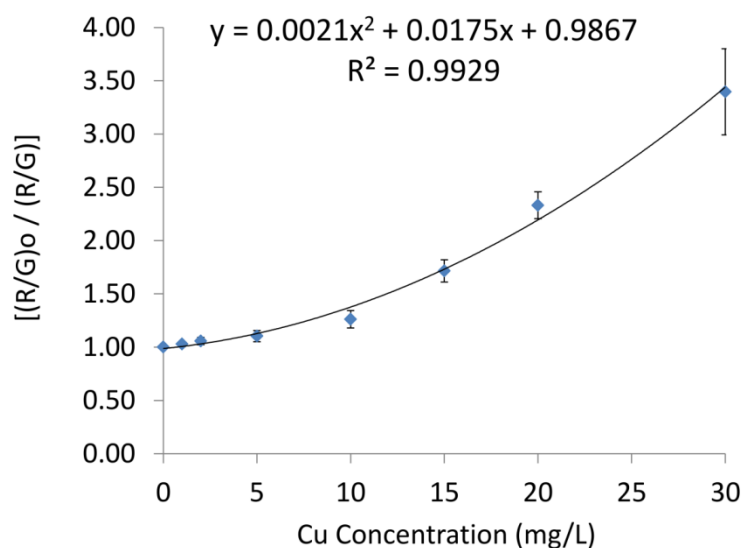


Figure 2.9 calibration curve derived from a Stern-Volmer plot for microfluidic copper detection from copper-fortified serum sample. (n=20, sample size= 20 μL).

In order to quantitatively determine a concentration, absolute intensity values of the red and green channels were used to plot a calibration graph. The plot between the intensity ratio of red to green and Cu^{2+} concentrations gave a negative slope, while the plot of the intensity ratio of green to red showed a positive slope. By measuring the absolute intensity values, there was no need for blanks to be measured. However, the presence of a high protein concentration in serum samples certainly reduced measurement sensitivity. The calibration graph showed two linear regions in two different concentration ranges. In the concentration range of 0 to 10 mg/L

($y = 0.0231x + 0.9026$, $R^2 = 0.9849$) the achieved sensitivity was lower than for the concentration range of 10 to 30 mg/L ($y = 0.0976x + 0.1357$, $R^2 = 0.9982$). The serum sample, which has a high protein concentration, did affect accuracy by depleting some of the copper (forming protein-Cu²⁺ complexes). The resulting limits of detection and quantification were 1.14 mg/L and 3.80 mg/L, respectively.

The precision and accuracy of the method were also evaluated for recovery. Four concentration levels of copper standards were prepared in FBS; 4 mg/L (close to the previously determined LOQ), 10 mg/L, 15mg/L, 20 mg/L. (Table 2) The overall recoveries were greater than 89% except for the sample having a concentration of 4 mg/L, near the LOQ.

Table 2.2 Recovery data for microfluidic copper detection of samples prepared in fetal bovine serum samples (n=40).

Add (mg/L)	Found		%Recovery	
	(mg/L)	SD	Value	SD
4	2.88	0.72	71.95	25.09
10	9.58	0.77	95.80	8.03
15	13.36	0.76	89.08	5.66
20	18.96	1.46	94.78	7.68

2.5 Conclusions

We have developed a microfluidic copper detection system incorporating a quantum dot wavelength-ratiometric sensor. It was demonstrated that copper in water and serum samples quenched the fluorescence signal of QD650 (red) on the QD ratiometric probe while the fluorescence signal of QD530 (green) remained constant,

resulting in a color change that was correlated directly to the concentration of copper in solution. RGB intensity value was used as a tool to quantitatively determine copper concentration in both environmental water samples and biological serum samples of clinical significance. The microfluidic QD wavelength-ratiometric detection system offers a simple, rapid, high-throughput, low-cost approach to detection of copper in environmentally and biologically relevant ranges of concentration. The platform has been further developed to quantitatively determine other analytes based on quantum dot assay using the RGB color space.

2.6 Acknowledgments

The authors acknowledge Christopher A. Heist for his assistance with development of a fabrication approach for production of the microfluidic chip, Simon Brundage for his assistance with reagent preparation, Dr. Shay Bracha (College of Veterinary Medicine) for consulting on copper toxicity in animals, and Kelly M. Ramzy for editorial review.

2.7 References

- (1) O'Dell, B. L.; Sunde, R. A. *Handbook of Nutritionally Essential Mineral Elements*; CRC Press, 1997.
- (2) Bremner, I. *Am. J. Clin. Nutr.* **1998**, *67* (5 Suppl), 1069S–1073S.
- (3) Fitzgerald, D. J. *Am. J. Clin. Nutr.* **1998**, *67* (5 Suppl), 1098S–1102S.
- (4) Carl A. Burtis; Ashwood, E. R.; Bruns, D. E. *Tietz Textbook of Clinical Chemistry and Molecular Diagnostics*, 5 edition.; Saunders: St. Louis, Mo, 2011.

- (5) Overview of Copper Poisoning: Copper Poisoning: Merck Veterinary Manual http://www.merckvetmanual.com/mvm/toxicology/copper_poisoning/overview_of_copper_poisoning.html (accessed Jan 15, 2016).
- (6) Jacela, J. Y.; DeRouchey, J. M.; Tokach, M. D.; Goodband, R. D.; Nelssen, J. L.; Renter, D. G.; Dritz, S. S. *J. Swine Health Prod.* **2012**, *18* (2), 87–91.
- (7) Mazloun Ardakani, M.; Salavati-Niasari, M.; Khayat Kashani, M.; Ghoreishi, S. M. *Anal. Bioanal. Chem.* **2004**, *378* (6), 1659–1665.
- (8) Procopio, J. R.; del Mar Ortiz Viana, M.; Hernandez, L. H. *Environ. Sci. Technol.* **1997**, *31* (11), 3081–3085.
- (9) Chen, D.; Darabedian, N.; Li, Z.; Kai, T.; Jiang, D.; Zhou, F. *Anal. Biochem.* **2015**, 27–35.
- (10) Shan, Z.; Lu, M.; Wang, L.; MacDonald, B.; MacInnis, J.; Mkandawire, M.; Zhang, X.; Oakes, K. D. *Chem. Commun. Camb. Engl.* **2016**, 2087–2090.
- (11) Arain, S. A.; Kazi, T. G.; Afridi, H. I.; Arain, M. S.; Panhwar, A. H.; Khan, N.; Baig, J. A.; Shah, F. *Ecotoxicol. Environ. Saf.* **2016**, *126*, 186–192.
- (12) Wustoni, S.; Hideshima, S.; Kuroiwa, S.; Nakanishi, T.; Mori, Y.; Osaka, T. *Analyst* **2015**, *140* (19), 6485–6488.
- (13) Chan, Y.-H.; Chen, J.; Liu, Q.; Wark, S. E.; Son, D. H.; Batteas, J. D. *Anal. Chem.* **2010**, *82* (9), 3671–3678.
- (14) Nurerk, P.; Kanatharana, P.; Bunkoed, O. *Lumin. J. Biol. Chem. Lumin.* **2015**.
- (15) Bian, W.; Wang, F.; Zhang, H.; Zhang, L.; Wang, L.; Shuang, S. *Lumin. J. Biol. Chem. Lumin.* **2015**, *30* (7), 1064–1070.
- (16) *Principles of Fluorescence Spectroscopy*; Lakowicz, J. R., Ed.; Springer US: Boston, MA, 2006.
- (17) Jayaraman, S.; Biwersi, J.; Verkman, A. S. *Am. J. Physiol. - Cell Physiol.* **1999**, *276* (3), C747–C757.
- (18) Zhang, K.; Zhou, H.; Mei, Q.; Wang, S.; Guan, G.; Liu, R.; Zhang, J.; Zhang, Z. *J. Am. Chem. Soc.* **2011**, *133* (22), 8424–8427.
- (19) Chen, T.; Hu, Y.; Cen, Y.; Chu, X.; Lu, Y. *J. Am. Chem. Soc.* **2013**, *135* (31), 11595–11602.
- (20) Gui, R.; Wan, A.; Jin, H. *Analyst* **2013**, *138* (20), 5956–5964.

- (21) Yao, J.; Zhang, K.; Zhu, H.; Ma, F.; Sun, M.; Yu, H.; Sun, J.; Wang, S. *Anal. Chem.* **2013**, *85* (13), 6461–6468.
- (22) Cen, Y.; Wu, Y.-M.; Kong, X.-J.; Wu, S.; Yu, R.-Q.; Chu, X. *Anal. Chem.* **2014**, *86* (14), 7119–7127.
- (23) Mu, Q.; Li, Y.; Xu, H.; Ma, Y.; Zhu, W.; Zhong, X. *Talanta* **2014**, *119*, 564–571.
- (24) Wang, K.; Qian, J.; Jiang, D.; Yang, Z.; Du, X.; Wang, K. *Biosens. Bioelectron.* **2015**, *65*, 83–90.
- (25) Liu, S.; Li, Y.; Zhang, C.; Yang, L.; Zhao, T.; Zhang, R.; Jiang, C. *J. Colloid Interface Sci.* **2017**, *493*, 10–16.
- (26) Hao, J.; Xiong, B.; Cheng, X.; He, Y.; Yeung, E. S. *Anal. Chem.* **2014**, *86* (10), 4663–4667.
- (27) Moonrungsee, N.; Pencharee, S.; Jakmunee, J. *Talanta* **2015**, *136*, 204–209.
- (28) Choodum, A.; Boonsamran, P.; NicDaeid, N.; Wongniramaikul, W. *Sci. Justice J. Forensic Sci. Soc.* **2015**, *55* (6), 437–445.
- (29) Chen, Y.; Zilberman, Y.; Mostafalu, P.; Sonkusale, S. R. *Biosens. Bioelectron.* **2015**, *67*, 477–484.
- (30) Pohanka, M. *Sensors* **2015**, *15* (6), 13752–13762.
- (31) Jung, Y.; Kim, J.; Awofeso, O.; Kim, H.; Regnier, F.; Bae, E. *Appl. Opt.* **2015**, *54* (31), 9183–9189.
- (32) Koesdjojo, M. T.; Wu, Y.; Boonloed, A.; Dunfield, E. M.; Remcho, V. T. *Talanta* **2014**, *130*, 122–127.
- (33) Koesdjojo, M. T.; Pengpumkiat, S.; Wu, Y.; Boonloed, A.; Huynh, D.; Remcho, T. P.; Remcho, V. T. *J. Chem. Educ.* **2015**, *92* (4), 737–741.
- (34) Loh, L. J.; Bandara, G. C.; Weber, G. L.; Remcho, V. T. *Analyst* **2015**, *140* (16), 5501–5507.
- (35) Zhang, K.; Mei, Q.; Guan, G.; Liu, B.; Wang, S.; Zhang, Z. *Anal. Chem.* **2010**, *82* (22), 9579–9586.
- (36) Thuy, U. T. D.; Liem, N. Q. *Adv. Nat. Sci. Nanosci. Nanotechnol.* **2013**, *4* (4), 45010.

- (37) Zeng, Q.; Kong, X.; Sun, Y.; Zhang, Y.; Tu, L.; Zhao, J.; Zhang, H. *J. Phys. Chem. C* **2008**, *112* (23), 8587–8593.
- (38) Wang, Y.-Q.; He, X.-W.; Li, W.-Y.; Zhang, Y.-K. *J. Mater. Chem. C* **2013**, *1* (11), 2202–2208.
- (39) Yu, W. W.; Qu, L.; Guo, W.; Peng, X. *Chem. Mater.* **2003**, *15* (14), 2854–2860.
- (40) Zhang, Y.; Shen, Y.; Wang, X.; Zhu, L.; Han, B.; Ge, L.; Tao, Y.; Xie, A. *Mater. Lett.* **2012**, *78*, 35–38.
- (41) Yao, J.; Zhang, K.; Zhu, H.; Ma, F.; Sun, M.; Yu, H.; Sun, J.; Wang, S. *Anal. Chem.* **2013**, *85* (13), 6461–6468.
- (42) Chan, Y.-H.; Chen, J.; Liu, Q.; Wark, S. E.; Son, D. H.; Batteas, J. D. *Anal. Chem.* **2010**, *82* (9), 3671–3678.
- (43) Ghosh, S.; Priyam, A.; Bhattacharya, S. C.; Saha, A. *J. Fluoresc.* **2009**, *19* (4), 723–731.
- (44) Astrini, N.; Anah, L.; Haryadi, H. R. *Macromol. Symp.* **2015**, *353* (1), 191–197.
- (45) Yu, X.; Tong, S.; Ge, M.; Wu, L.; Zuo, J.; Cao, C.; Song, W. *J. Environ. Sci.* **2013**, *25* (5), 933–943.
- (46) Weltje, L.; Hollander, W. D.; Wolterbeek, H. T. *Environ. Toxicol. Chem. SETAC* **2003**, *22* (2), 265–271.
- (47) Zhou, D.; Zhang, L.; Zhou, J.; Guo, S. *Water Res.* **2004**, *38* (11), 2643–2650.
- (48) Castro, G. R. de; Alcântara, I. L. de; Roldan, P. dos S.; Bozano, D. de F.; Padilha, P. de M.; Florentino, A. de O.; Rocha, J. C. *Mater. Res.* **2004**, *7* (2), 329–334.
- (49) *Quantitative Chemical Analysis*, 9th edition.; W. H. Freeman: New York, NY, 2015.
- (50) Hardzei, M.; Artemyev, M. *J. Lumin.* **2012**, *132* (2), 425–428.
- (51) Long, G. L.; Winefordner, J. D. *Anal. Chem.* **1983**, *55* (7), 712A–724A.
- (52) Torrado, A.; Walkup, G. K.; Imperiali, B. *J. Am. Chem. Soc.* **1998**, *120* (3), 609–610.
- (53) Xie, H.-Y.; Liang, J.-G.; Zhang, Z.-L.; Liu, Y.; He, Z.-K.; Pang, D.-W. *Spectrochim. Acta. A. Mol. Biomol. Spectrosc.* **2004**, *60* (11), 2527–2530.

CHAPTER 3

**A PAPER-BASED DISPOSABLE WELL PLATE FOR CYANIDE
DETECTION INCORPORATING A FLUORESCENT CHITOSAN-CdTe
QUANTUM DOT NANOPARTICLE****3.1 Abstract**

A novel approach to building a paper-based well plate, here applied to cyanide detection, is described. Chitosan encapsulated CdTe quantum dots with a maximum emission of 520 nm (CS-QD520) were synthesized, characterized, and used as fluorophores. The CS-QD520 was specifically quenched by copper (II), and the quenched CS-QD520, was deposited onto a glass microfiber filter (grade GF/B) via electrostatic attraction. Subsequent introduction of cyanide ion (on sample application) resulted in fluorescence recovery upon release of copper from the QD surface to form copper cyanide complex, thus freeing the CS-QD520 nanoparticle. The “Signal-On” fluorescence linearly correlates to cyanide concentration in the range of 0 to 200 μM . The QD fluorescent assay on glass microfiber filter was incorporated into a paper-based well plate format to enhance sample throughput. Three layers of paper well plate design were cut using a laser cutter and assembled using 5% (w/v) polycaprolactone (PCL) in toluene and a low-cost laminator. The experimental conditions, namely probe concentration, amount of copper, and well-plate design, were optimized and applied to detect cyanide in drinking waters and environmental samples. The sensitivity of the assay dramatically increased since the reaction was preconcentrated and performed on the surface of the glass microfiber filter rather than in bulk solution (in the traditional well plate format). The paper-

based disposable well plate incorporating CS-QD520 makes a rapid, high throughput, low-cost testing feasible, and convenient for cyanide detection.

3.2 Introduction

Cyanide is a group of chemicals containing carbon bound to nitrogen with a triple covalent bond. Cyanide is able to form complexes with metals as metal-cyanide complexes or can be found as free cyanide, which is the most toxic form. It can naturally occur in plants as cyanogenic glycoside or discharged from some metal mining processes, photogenic developing, chemical industries, combustion of plastic and vinyl as well as cyanide-containing pesticides.¹ Cyanide can enter the human body by breathing air, drinking water, or absorption through the skin. Cyanide in the blood, existing as HCN (weak acid with $pK_a = 9.21$), freely crosses all biological membranes and binds to heme iron (Fe^{3+}) in the cytochrome a-a3 complex. It readily works as a competitive inhibitor causing decoupling of oxidative phosphorylation.² This action prevents the cell from utilizing oxygen leading to the rapid onset of cellular hypoxia – flushing, headache, tachypnea, respiratory depression, complete heart block, and death. Maximum contaminant level (MCL) in drinking water was set at 0.2 mg/L (7.7 μ M) by US Environmental Protection Agency.³

In North America, about 100 million kg cyanide is used annually by the industrial sector, of which 80% is used in gold mining or cyanidation process.^{4,5} If the industrial regulations are not properly enforced, the leaching of the cyanide-containing water will poses potential hazards to wildlife, fish, aquatic biota and human health. US EPA set an analytical standard method based on the

spectrophotometric detection.⁶ Chloramine-T with pyridine-barbituric acid is used to react with free cyanide to form a colored complex measured at 578 nm. Several conventional detection techniques for cyanide have been recently reviewed⁷⁻⁹ including UV-Vis spectrometry, capillary electrophoresis, potentiometry, voltammetry, IC-PAD, and GC/MS. These analytical methods are expensive, time consuming, and requiring both a laboratory setting and a skilled analyst.

Another approach for cyanide detection is a chemodosimeter, which uses chromogenic or fluorogenic probes that change color when they react with a cyanide ion. The selectivity of detection is based on cyanide's property as an exceptional nucleophile, better than other common anion, for functional groups presented in the probes. The chemical reactions include carbon-carbon bond formation,¹⁰⁻¹⁷ proton transfer,¹⁸⁻²⁰ and electron transfer.²¹⁻²³ Although detection limits for this approach can be as low as $\mu\text{g/L}$ or nM, the assays were mainly performed in an aqueous/organic-based solution and chromogenic or fluorogenic probes required complex synthetic processes in an organic solvent.

Semiconductor nanocrystals or quantum dots (QDs) have superior optical properties when compared to organic fluorophores, namely high photostability, highly tunable emission wavelengths, large Stokes shifts, broad absorption spectra, and narrow emission peaks. TOPO-coated CdSe QDs²⁴ and mercaptosuccinic acid-capped CdTe QDs²⁵ were used for cyanide determination in water samples by prior quenching of their fluorescence with copper ions. The introduction of cyanide caused the dissociation of copper from the QD surface resulting in fluorescence recovery. The modulation of QDs and copper as a sensor enables a simple approach for cyanide

detection with a low detection limit; however, all assays were conducted in liquid phase reagents. In our previous work, we have developed a microfluidic copper detection incorporating a wavelength-ratiometric fluorescent QD pair²⁶ demonstrating the potential ability of a dried QDs assay for a field test.

Due to the fact that cyanide is extremely toxic, causing acute cytotoxic hypoxia, rapid screening or point-of-care testing would be invaluable for quick detection. According to The Office of the Chief Medical Examiner for the City of New York, a commercially available paper test, namely Cyantesmo® (Macherey-Nagel, Dueren, Germany) is currently used to qualitatively screen for the presence of cyanide in aqueous solutions.²⁷ The Cyantesmo® has been validated in water samples²⁸ (0.25 – 30 µg/mL), blood²⁹ (0.2 – 10 µg/mL), and plant material³⁰ (1 – 50 µg/mL) at clinically relevant concentrations. In water samples, semi-quantitative detection of cyanide at concentrations greater than 1 mg/L can be accomplished in 5 minutes. However, for concentrations lower than 0.75 mg/L, more than 2 hours are required for adequate colorimetric development, severely limiting its ability for rapid detection of low cyanide concentrations.

Paper microzone plates are a class of microfluidic paper-based analytical devices (µPADs) containing hydrophilic regions defined by hydrophobic barriers for fluid handling. This type of point-of-care diagnostic device, related to conventional 96- and 384-plastic well plates, was first introduced by the Whitesides group using a photolithographic fabrication technique.³¹ Our research group has continued developing paper-based detection platforms with different novel fabrication techniques. In some of these applications, we used a biodegradable hydrophobic

polymer, polycaprolactone (PCL) to make a hydrophobic barrier on the paper, along with the use of a low-cost laminator (\$30) to assemble multiple layers of paper.^{32–34} The proposed fabrication technique is fast, simple, and inexpensive. Spot test of the dry assay on each individual well was independently performed on a glass microfiber filter promoting its use in resource-limited setting.

In this work, we demonstrated the fabrication and use of paper-based disposable well plates for cyanide detection using the CS-QD520 as a sensor. The sensing mechanism for the detection is shown in Figure 3.1.

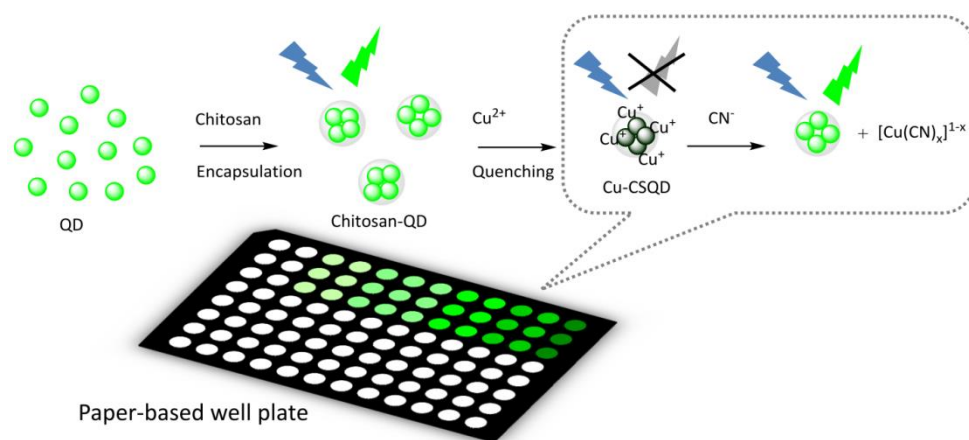


Figure 3.1 Schematic diagram of paper-based well plate for cyanide detection based on CS-QD520 nanoparticles.

Our well plate design makes use of chitosan encapsulated CdTe QDs with a maximum emission at 520 nm (CS-QD520) as fluorophores, which were specifically quenched by copper (Cu²⁺). The quenched chitosan-QD nanoparticle was used as a sensor probe for cyanide detection. Upon cyanide introduction, the fluorescent signal was recovered due to the formation of copper cyanide complex [Cu(CN)_x]^{1-x}, thus freeing the chitosan-QD nanoparticle. The “signal-ON” fluorescence was graphed against clinically relevant cyanide concentrations. The fluorescent assay was

preconcentrated on the surface of a glass microfiber filter enabling higher signal compared to solution based assays due to the increased surface to volume ratio. Each well on the paper well plate ran an independent assay enabling simultaneous analysis of multiple samples. The paper-based well plate format incorporated disposable μ PADs into the existing ubiquitous analytical instrument, namely the microplate reader. The platform enabled rapid inexpensive testing, high sample throughput, and reliable quantitative results with good specificity.

3.3 Materials and methods

3.3.1 Materials

All the chemicals used were of analytical-reagent grade. Deionized water was obtained from a Milli-Q® Advantage A10 (EMD Millipore, Billerica, MA, USA). CdCl_2 (anhydrous, 99%), tellurium powder (~200 mesh, 99.8%), 3-mercaptopropionic acid (MPA, 99%), Sodium borohydride (NaBH_4 , 98%), Chitosan (MW = 50 – 190 KDa, 75-85% deacetylated) were purchased from Sigma-Aldrich (St. Louis, MO, USA). 1-ethyl-3-(3-dimethylaminopropyl)carbodiimide hydrochloride (EDC) and N-hydroxysuccinimide (NHS) were purchased from Thermo Scientific (Rockford, IL, USA). Polycaprolactone (PCL, Capa™ 6800, MW = 80 000) was obtained from Perstorp (Cheshire UK). Copper sulfate ($\text{CuSO}_4 \cdot 5\text{H}_2\text{O}$) was purchased from Fisher Chemical (Fair Lawn, NJ, USA). Potassium Cyanide (KCN) was obtained from Mallinckrodt (Phillipsburg, NJ, USA). Black filter paper was purchased from Ahlstrom Filtration LLC (Mt. Holly Springs, PA, USA). Microfiber filter (grade GF/B) was purchased from Whatman GE healthcare

(Buckinghamshire, UK). Black poster paper board was purchased from UCreate poster board, 22"x28" (Charlotte, NC, USA).

3.3.2 Synthesis of core CdTe quantum dots

CdTe QDs were synthesized in aqueous solution as previously described with some modifications.³⁵ Two mmol anhydrous CdCl₂ (0.3666 g) and 4.8 mmol 3-mercaptopropionic acid (418 µL) were mixed in 200 mL of Milli-Q water. The pH of the solution was adjusted to 11 using 1.0 M NaOH. The mixture was purged with N₂ gas for 30 min to eliminate oxygen from solution. The NaHTe solution was prepared separately by mixing 0.5 mmol tellurium powder (63.8 mg) and 5 mmol NaBH₄ (0.1891 g) in 5 mL Milli-Q water. The NaHTe precursor was added to the cadmium precursor solution and the mixture was refluxed at 95-100°C for 3 hours under N₂ atmosphere. The final molar ratio of Cd²⁺/MPA/NaHTe was 1:2.4:0.25, respectively. The average diameter and concentration of CdTe QDs were calculated as 1.76 nm and 81.7 µM, respectively.³⁶

3.3.3 Synthesis of chitosan encapsulated CdTe quantum dots (CS-QD520)

Chitosan stock solution (1% w/v) was prepared by dissolving 1 g chitosan in 100 mL of 1% (v/v) acetic acid. The stock solution was subsequently diluted to 0.01% (w/v) using 0.1%(v/v) acetic acid. As prepared CdTe QDs solution (22 mL) was gradually added in 100 mL of 0.01% chitosan solution with stirring followed by addition of 1 mL EDC (10mg/mL) /NHS (5mg/mL) solution. The mixture was further stirred overnight at room temperature to form covalent bonds between carboxylic

acids on the surface of the QDs and amino groups on chitosan. The chitosan encapsulated CdTe QDs was washed 3 times with Milli-Q water by centrifugation. In the final step, the precipitate was re-dispersed and stored in 22 mL (the same volume as QD520) phosphate buffer 10 mM, pH 7.4. The concentration of CS-QD520 would be 81.7 μM derived from QD520 concentration. The mass/volume concentration is 3.76 mg/mL.

3.3.4 Cyanide probe - Quenching of CS-QD520 by copper ion

The stock chitosan-QD solution was diluted 10 fold with Tris-HCl buffer (10 mM, pH 7). A certain amount of Cu^{2+} standard (100 mg/L) was added to the diluted CS-QD520 solution with stirring to quench the fluorescence signal. The quenching reaction was continued for 3 hours. Twenty microliters of the quenched solution was dropcasted on a circular piece of GF/B (6.8 mm diameter, cut by a hole punch). The sensor dot was dried overnight at 40°C in a vacuum oven.

3.3.5 Paper-based well plate and a plate holder

The paper based well plate was designed and drawn to resemble a standard 96-plastic well plate using SolidWorks® 2013 (Dassault Systèmes, Waltham, MA, USA) shown in Figure 3.2. The design contained three layers: bottom, middle, and top. The bottom and middle layer were composed of black poster paper (0.45 mm thickness). The top layer was composed of black filter paper (0.15 mm thickness). Each well on the middle layer has a diameter of 6.8 mm to match with the GF/B sensor dot. The top layer contained wells with a diameter of 5.4 mm, smaller than the

wells on the middle layer. This helped lock the GF/B sensor dots in place in the middle layer. The poster paper and the filter paper were cut using a laser cutter (VS 3.50, Universal Lasers, Scottsdale, AZ, USA). The paper-based well plate was assembled by first air-brushing 5% polycaprolactone (PCL) in toluene in between each of the paper layers. A low-cost thermal laminator (Scotch, model TL902A) was used to press all layers together resulting in the melting of PCL on the paper surfaces. First, the top and middle layers were laminated before aligning the GF/B sensor dots in the wells. Finally, the bottom layer was laminated to the previously prepared assembly. PCL acts as a hydrophobic barrier preventing fluid flow between individual wells allowing for independent assays on the same plate. The disposable well plate was stored in a vacuum-sealed bag prior to use. The paper-based well plate was designed to be placed in a plate holder (described in the next section), which was compatible with the tray of any standard plate reader.

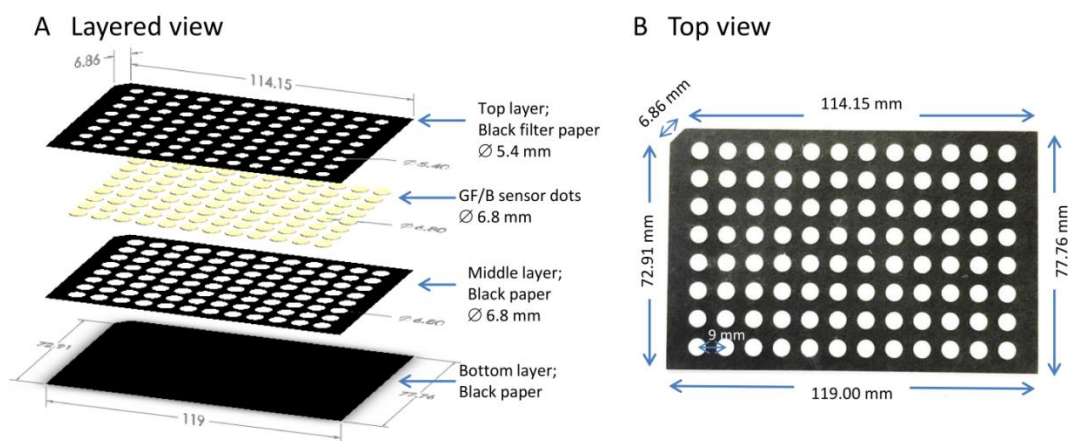


Figure 3.2 A Paper-based well plate resembling a standard plastic 96 well plate designed for use in a plate reader. (A) Layered-view from SolidWorks®; (B) The actual top view.

The plate holder (Figure 3.3) was drawn using SolidWorks® 2013 and printed with a 3D printer (Ultimaker2) using polylactic acid (PA) material. The paper plate was fitted inside the plate holder and ready to use.

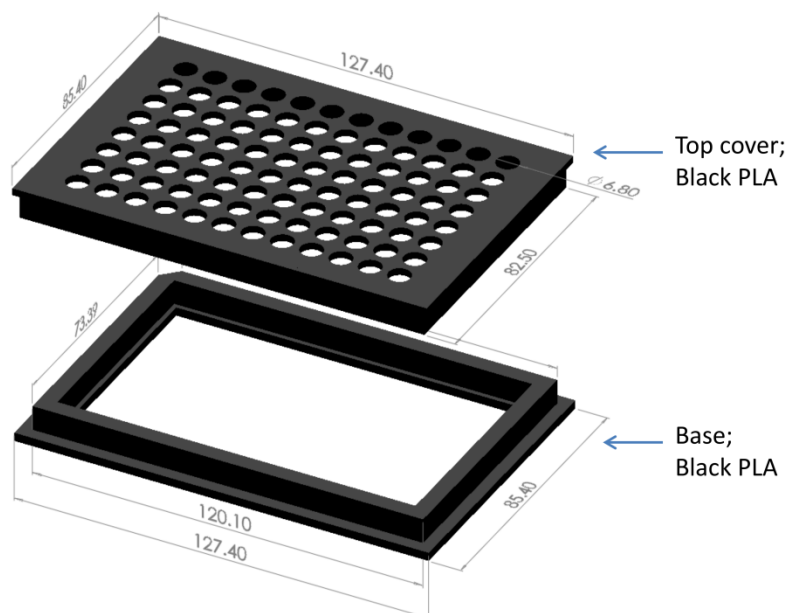


Figure 3.3 A plate holder for the paper-based well plate. Base and Top-cover were designed using SolidWorks® 2013 and printed using 3D printer Ultimaker2.

3.3.6 Quantitation of cyanide ion on a chip

Disposable paper based well plates were placed in plastic holders prior to detection. Twenty microliters of cyanide standards or samples were applied directly to the paper based well plate and allowed to react at room temperature. The liquid sample absorbed on the GF/B substrate and slowly reacted with the Cu-CSQD520 on the top surface of the GF/B. A fluorescence signal was measured at 520 nm with the excitation wavelength at 350 nm using a fluorescence plate reader (Gemini XS, Molecular Devices, Sunnyvale, CA, USA).

3.4 Results and discussion

3.4.1 Characterization of CdTe QDs and chitosan encapsulated QDs

Chitosan encapsulated CdTe QDs with a maximum emission at 520 nm were synthesized in an aqueous solution and used as a fluorophore. The CS-QDs nanoparticles formed via the electrostatic attraction between the positive charge of the amino functional groups on chitosan and negative charge of MPA on the QD surface. Both chitosan and QDs were covalently linked through amide bond formation by carbodiimide chemistry. The scan emission spectra of QD520 and CS-QD520 shown in Figure 3.4A indicated that fluorescence intensity of CS-QD520 was 3.5 times higher than those of the original QD520 at the same mass/volume concentration.³⁷ This exceptional phenomenon may result from the intrinsic properties of chitosan. The numerous amino and hydroxyl functional groups on the biopolymer act as good capping agents, helping to stabilize the QDs surface.³⁸⁻⁴⁰ The morphology of CS-QD520 was studied by TEM (FEI Titan with ChemiSTEM mode) as shown in Figure 3.4B, which revealed the irregular shape of the nanoparticles with a particle size of about 10 – 25 nm. The elemental analysis from ChemiSTEM mode in Figure 3.4C confirmed the presence of cadmium and telluride in the chitosan encapsulated CdTe QDs.

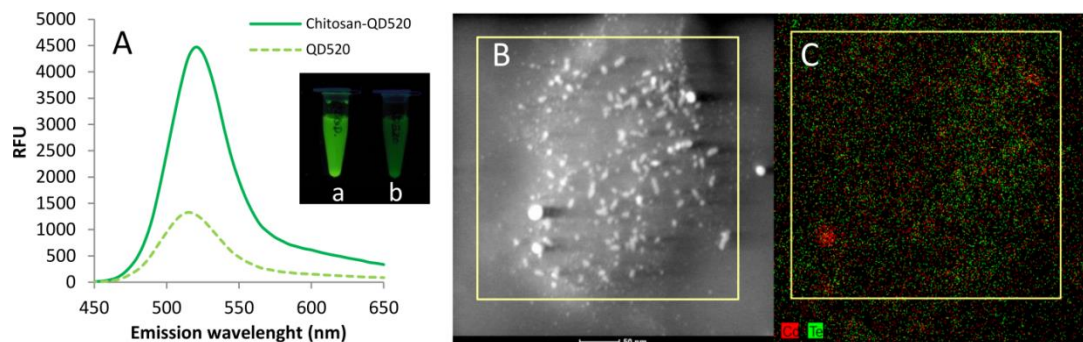


Figure 3.4 Characterization of chitosan encapsulated CdTe QDs (CS-QD520): (A) Emission spectra of CS-QD520 compared to the original QD520. Inset a) CS-QD520, b) QD520 under UV light 365 nm; (B) TEM image of CS-QD520; (C) ChemiSTEM mode image of the same area of B showing elemental analysis.

We incorporated chitosan into CdTe QDs in order to facilitate its use on a paper-based well plate format. Chitosan is a biocompatible and biodegradable polymer, which has been integrated with nanomaterials⁴¹ and microfluidic chips⁴² in the biomedical field. Due to the fact that chitosan contains plenty of amino groups on the side chain, they are readily available for bioconjugation, exhibiting a positive charge at acidic to neutral pH (pKa of D-glucosamine unit = 6.5 – 7.0)⁴³ When CS-QD520 was applied on the glass microfiber filter containing silanol groups, the chitosan-QD nanoparticle was electrostatically adsorbed only on the top surface of the substrate, while QD520 thoroughly absorbed into the substrate. We also evaluated the retention capability of CS-QD520 as shown in Figure 3.5. The CS-QD520 was permanently retained on the top of the substrate after flushing with 10 mL of PB buffer. The CS-QD520 remained in a tight narrow band on the top of the GF/B, whereas the original QD520 leached off from the substrate. Having a low fluorescence background and high loading volume capacity, the GF/B enabled the

retention of CS-QD520 on its top surface. This improved the homogeneity of fluorescence signal, promoting its use on paper-based format.

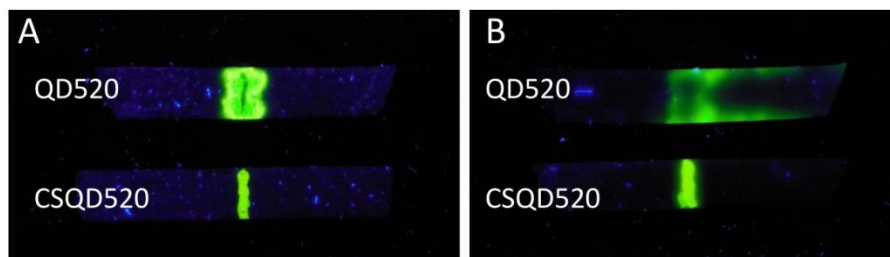


Figure 3.5 Interaction of CS-QD520 on the GF/B surface. Both QD520 and CS-QD520 were applied on the GF/B surface and dried in the vacuum oven: (A) Before flushing with PB buffer 10 mM, pH 7; (B) After flushing with PB buffer 10 mM, pH 7.

3.4.2 Paper-based well plate design and evaluation

The idea of paper-based well plate was first introduced by Whitesides group using a photolithography fabrication technique.³¹ The paper-based well plate format provided several advantages for point-of-care diagnostics including high sample throughput, low cost alternative to plastic plates, environmental more friendly, better suitability to on-site applications. We continued developing the platform for rapid cyanide detection with our novel, inexpensive, simple fabrication technique. Black poster paper (0.45 mm thickness) was chosen as a material for the bottom and middle layer due to its low cost, sturdiness, and low fluorescence background. Black filter paper (0.15 mm thickness) was used as a top layer to hold the GF/B sensor dot in place. Both black poster and filter paper were cut to the size of a standard well plate. Polycaprolactone in toluene was air-brushed on every cut paper surface, leaving thin film PCL on the surface. This made a hydrophobic barrier on each individual well in

the paper plate. Not only being used as a hydrophobic boundary, the PCL in-between layers also functioned as an adhesive, attaching each plate layer together.

The performance of the well plate was evaluated for PCL hydrophobicity. Two parameters were assessed, namely volume of liquid sample and retention time for liquid to be held in the wells. These two parameters related to the degree of cross contamination from well to well. Food coloring was used, representing a liquid sample applied on the plate enabling visual inspection. The results from Figure 3.6 showed that with 5% PCL sprayed on the paper, the loading capacity of the liquid sample was 25 μL /well. When the percentage of PCL was increased to 10%, the sample loading capacity increased to 30 μL .


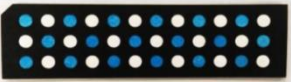









5% PCL in toluene	T = 0 min, 25 μL (no leaking) 	T = 30 min, 25 μL (no leaking) 
	T = 0 min, 30 μL (no leaking) 	T = 30 min, 30 μL (leaking) 
	T = 0 min, 35 μL (leaking) 	
7.5% PCL in toluene	T = 0 min, 30 μL (no leaking) 	T = 30 min, 30 μL (leaking) 
10% PCL in toluene	T = 0 min, 30 μL (no leaking) 	T = 30 min, 30 μL (no leaking) 
	T = 0 min, 35 μL (small leaking) 	T = 30 min, 35 μL (leaking) 

Figure 3.6 Evaluation of 3-layered paper-based well plates for a PCL hydrophobic barrier. Leak testing on the paper-based well plates were visually inspected. Percent of PCL in toluene, volume of liquid sample, and retention time for liquid to be held in the wells were varied.

According to the design principle of the fabrication method for the well plate, the sample loading capacity of the paper-based well plate can be increased by inserting additional layers in the middle for a larger volume. For the proof of concept, we demonstrated that the loading capacity can be increased up to 40 μL with a 4-layer paper-based plate design shown in Figure 3.7.

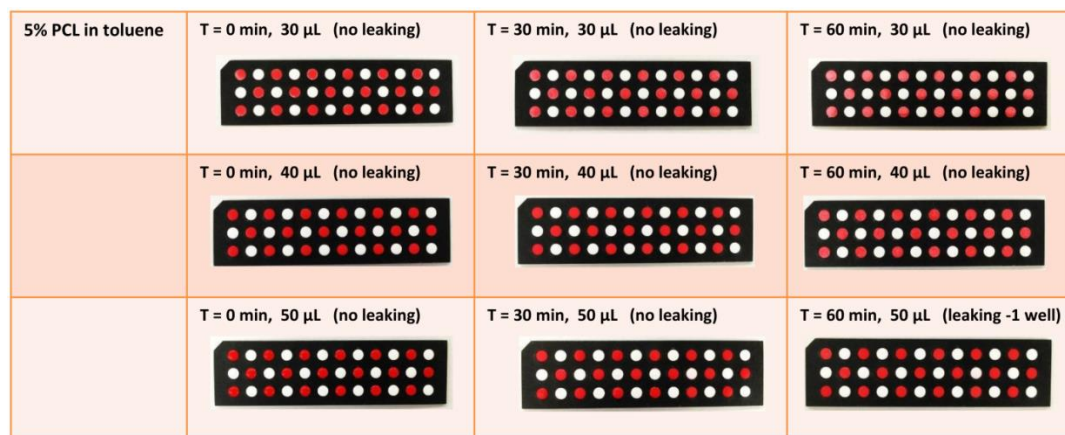


Figure 3.7 Evaluation of 4-layer paper-based well plates for a PCL hydrophobic barrier. Leak testing on the paper-based well plates were visually inspected. Volume of liquid sample, and retention time for liquid to be held in the wells were varied.

3.4.3 Detection mechanism and selectivity

The present work demonstrated the cyanide sensor probe using the signal “ON” fluorescence from chitosan-QDs nanoparticle on a paper-based well plate. Chitosan-QDs nanoparticles were specifically quenched by copper. The introduction of cyanide upon sample application, removed Cu^+ from the QD surface forming highly stable $[\text{Cu}(\text{CN})_x]^{1-x}$ species.^{25,44} This phenomenon caused the fluorescence recovery of the releasing CS-QD520, which was proportional to the cyanide concentration. The signal “ON” of the chitosan-QD sensor eliminated a false positive result and enabled higher sensitivity than signal “OFF” sensor.²⁵

The selectivity of the assay on the paper-based well plate was evaluated by testing with several common anions and cations, including F^- , Cl^- , I^- , SCN^- , CH_3COO^- , NO_3^- , $C_2O_4^{2-}$, CO_3^{2-} , SO_4^{2-} , S^{2-} , Mg^{2+} , Al^{3+} , Mn^{2+} , Zn^{2+} , Fe^{2+} , Cd^{2+} , Ni^{2+} , Co^{2+} , Hg^{2+} , and Pb^{2+} at concentrations of 1 mM. Their fluorescence signals were monitored and compared with the fluorescence obtained from cyanide at 100 μM . The results, shown in Figure 3.8A and 3.8B, demonstrate that in all cases the tested anions and cations did not contribute to increased fluorescence intensity. Hence, the sensor probe was highly selective toward cyanide.

The detection method described here, was intended to determine free cyanide, which is the most toxic and reactive form. According to the EPA standard method 9016, for any cyanide detection, if there is a presence of interferences in a solution, namely chlorine and sulfide, they can degrade cyanide into cyanogen chloride and thiocyanate, respectively. The water samples can be treated prior testing; chlorine can be eliminated by adding a reducing agent such as sodium thiosulfate or ascorbic acid; sulfide can precipitate with lead acetate or lead carbonate.

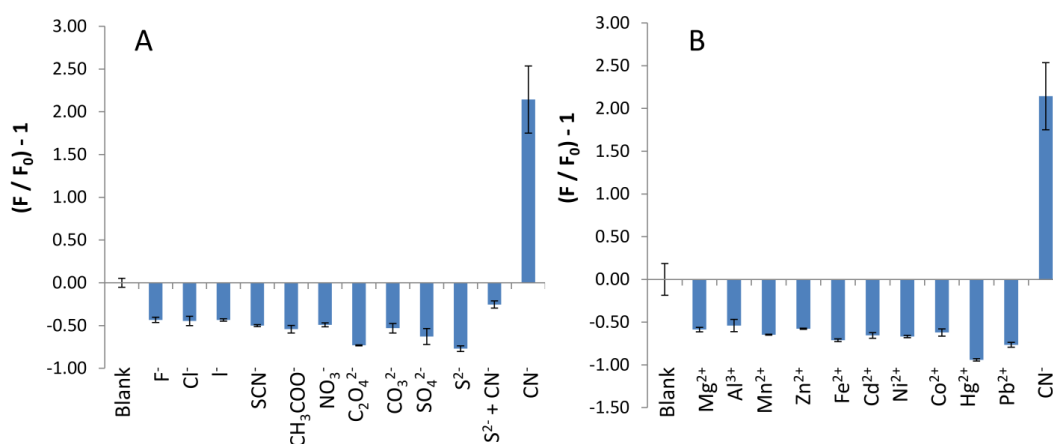


Figure 3.8 Selectivity of the assay on paper-based well plates: (A) a set of tested anions at 1 mM compared to cyanide at 100 μM ; (B) a set of tested cations at 1 mM compared to cyanide at 100 μM .

3.4.4 Optimization of the cyanide assay on paper-based well plate

Transferring the highly selective assay of copper-modulated chitosan-QDs to the paper-based format presented several advantages over a solution-based assay. One benefit was that paper-based well plates offered higher sensitivity than the solution based formats. We performed the preliminary experiment shown in Figure 3.9 that the dried assay on a paper-based well plate has about 20 times higher sensitivity than the assay in a solution. This is due to the high surface to volume ratio of GF/B used as a supporting material. In this case, QD sensors were preconcentrated on the top surface of GF/B.

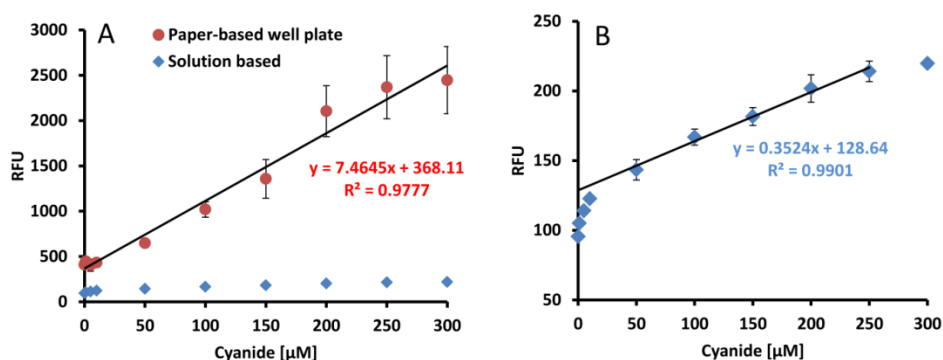


Figure 3.9 Comparative study of assay sensitivity: (A) Calibration graph of the assay on a paper-based well plate; (B) Calibration graph of the assay in a solution. Preliminary conditions: CS-QD520 at 8.17 μM was quenched with 50 μL - Cu^{2+} (100 mg/L) for 2 hr. For the solution-based assay, 50 μL of sensor was mixed with 50 μL of cyanide standard.

In order to maximize the sensitivity of the paper-based well plate cyanide detection, we optimized the assay chemistry, including CS-QD520 concentration, amount of Cu^{2+} for quenching, and reaction time. Firstly, CS-QD520 concentration was varied from 4.08 – 20.43 μM . The calibration graphs in Figure 3.10 (A) showed that the calibration slopes dramatically increased from 4.08 μM to 8.17 μM with little

change in slope after 8.17 μM . The optimum sensor probe concentration was then chosen at 8.17 μM . Second, the amount of Cu^{2+} to modulate the fluorescence signal played a crucial role for the sensitivity since the detection mechanism was based on the formation of $[\text{Cu}(\text{CN})_x]^{1-x}$ species. For example, if there is free Cu^{2+} in the assay, it will first form a complex with the added cyanide and no fluorescence is generated. On the contrary, if there is less Cu^{2+} in the assay, high fluorescence background will be obtained, having a negative impact on the detection limit. The optimum amount of Cu^{2+} (100 mg/L) for QD quenching was found to be 40 μL per 1 mL of 8.17 μM CS-QD520 (Figure 3.10B). Third, the reaction time for fluorescence recovery was monitored, shown in Figure 3.10C. After the introduction of cyanide, fluorescence slowly regenerated owing to the releasing of free CS-QD520 from copper. The longer the reaction time, the more sensitive the assay. However, in the interests of a rapid test, there was a necessity for minimizing reaction time while maintaining high sensitivity. The optimum reaction time was chosen at 30 min because it offered higher sensitivity with a low standard deviation.

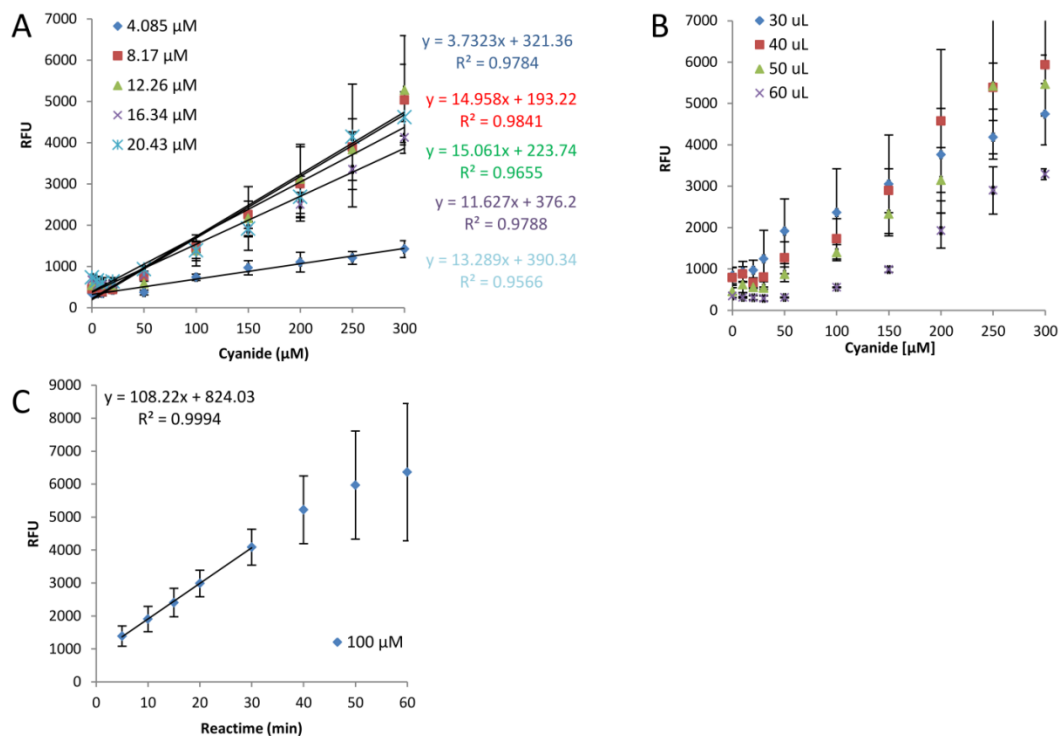


Figure 3.10 Optimization parameters for cyanide detection on paper-based well plates; (A) Effect of CS-QD520 concentration [condition: ratio of CSQD : Cu^{2+} (100 mg/L) = 4.085 μM : 25 μL , reaction time = 30 min]; (B) Effect of amount of Cu^{2+} (100 mg/L) for quenching CS-QD520 probe [condition: CSQD = 8.17 μM , reaction time = 30 min]; (C) Effect of reaction time [condition: CSQD = 8.17 μM , Cu^{2+} , 100 mg/L = 40 μL]

3.4.5 Quantitative cyanide analysis

A calibration curve for cyanide detection in water samples was established using the optimum conditions. The data for calibration curves was collected both within-day and between-days (4 days; $n=12$). A linear calibration plot covering the range of 0 - 200 μM was generated from the entire data pool; $y = 27.441x + 1398$ ($R^2 = 0.997$) (Figure 3.11).

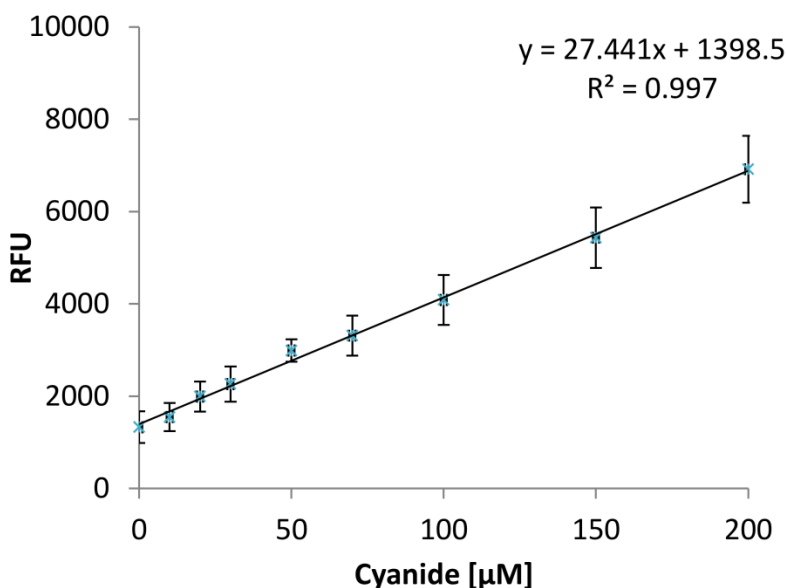


Figure 3.11 Endpoint calibration graph derived from paper-based well plates for cyanide detection; [condition: CS-QD520 = 8.17 μM , amount of Cu^{2+} (100 mg/L) = 40 μL / 1 mL of 8.17 μM CS-QD520, reaction time = 30 min]

Limit of detection (LOD) and limit of quantification (LOQ) were determined using the International Union of Pure and Applied Chemistry (IUPAC) definitions. LOD and LOQ were 11.6 μM (0.3 $\mu\text{g}/\text{mL}$) and 38.7 μM (1 $\mu\text{g}/\text{mL}$), respectively. The LOD presented here by disposable paper-based well plate was comparable to the commercially available “Cyantesmo kit” (0.25 – 30 $\mu\text{g}/\text{mL}$) with quantitative results rather than the semi-quantitative results obtained with the “Cyantesmo kit”.

3.4.6 Real sample analysis

The real sample analysis was performed by using drinking water as a matrix. Drinking water was obtained from a local store; adjusted to a pH above 12 with 50% NaOH prior to analysis. It was found that there was no cyanide detected in the drinking water used. The accuracy and precision of the detection system were

assessed by measuring recovery at three standardized cyanide concentration levels added to drinking water; low (50 μM), medium (100 μM), and high (200 μM) over the calibration curve (Table 3.1). At low cyanide concentration (50 μM), the %RSD was larger than that of high cyanide concentration (200 μM). The disposable paper-based well plate demonstrated high accuracy with acceptable recovery (the recovery levels recommended by the Association of Official Analytical Chemists (AOAC) International are in the range of 75-120% at the 1 ppm concentration level). The lower recovery of cyanide at 50 μM may result from the trace metals present in the drinking water, which can deplete the fortified cyanide standard.

Table 3.1 Recovery of cyanide at different concentrations in drinking water (N=10)

Samples	Added	Found	Recovery	RSD
	(μM)	($\mu\text{M} \pm \text{SD}$)	(% \pm SD)	(%)
Low	50	37.64 \pm 5.33	75.28 \pm 10.66	14.16
Medium	100	82.72 \pm 8.75	82.72 \pm 8.75	10.57
High	200	198.25 \pm 12.44	99.13 \pm 6.22	6.27

3.4.7 Kinetic fluorescent method for cyanide detection on a paper-based well plate

Kinetic fluorescence is a method for studying reaction rates of chemical or physical transformations first introduced by Ryan and Ingle (1980).⁴⁵ An increase or decrease in fluorescence intensity is directly correlated with the formation or degradation of a fluorescent species. Kinetic method establishes a relationship between the change in fluorescence intensity per unit time (reaction rate) and the concentration of the reactants. In general, the advantages of kinetic method are improved specificity and precision due to the fact that only species which react and generate a change in the monitored fluorescence signal are measured. Thus, steady state signals such as scattering or background fluorescence do not interfere with the analytical signal.

In the experiment, the fluorescence recovery was generated from the formation of copper cyanide complexes following the release of free CS-QD520. The reactions between copper(II) and the cyanide ion start with a thermodynamic reduction of Cu(II) to Cu(I),⁴⁶ followed by a series of reactions shown in Table 3.2.

Table 3.2 Thermodynamic quantities for the Cu^+ and CN^- system.⁴⁷⁻⁴⁹

Reaction	Log K	ΔG°	ΔH°	ΔS°
		kcal/mol	kcal/mol	cal/deg mol
$\text{Cu}^+ + 2\text{CN}^- \longrightarrow \text{Cu}(\text{CN})_2^-$	23.94	-32.7	-29.1	+12
$\text{Cu}(\text{CN})_2^- + \text{CN}^- \longrightarrow \text{Cu}(\text{CN})_3^{2-}$	5.3	-7.23	-11.1	-13.4
$\text{Cu}(\text{CN})_3^{2-} + \text{CN}^- \longrightarrow \text{Cu}(\text{CN})_4^{3-}$	1.5	-2.0	-11.2	-31

The formation of cyanide complexes gives negative Gibbs free energies (Table. 3.2) indicating that all of the reactions are stable and spontaneous. The

distribution of copper cyanide species depends upon the molar ratio of cyanide to copper, total cyanide concentration, pH, and temperature. The distribution favors the highly coordinated complex $[\text{Cu}(\text{CN})_4]^{3-}$ at a high cyanide concentration.

As mentioned earlier, the fluorescence intensity increased with the reaction time (Figure 3.12) revealing the reaction kinetics of the fluorescence assay. The fluorescence signal dramatically increased at the first 30 min and slowly increased until 60 min.

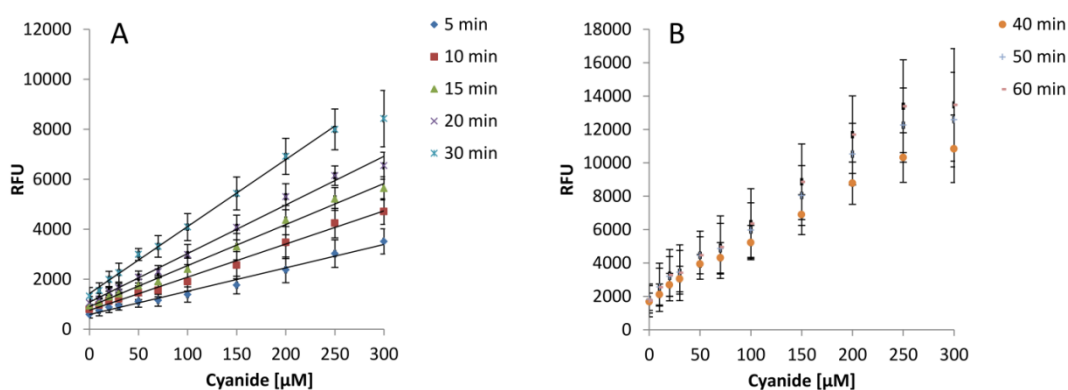


Figure 3.12 Calibration graphs plotted between cyanide concentrations and fluorescence intensity (A) at 5 to 30 min; (B) at 40 to 60 min.

In order to determine the reaction rate for each cyanide concentration, the calibration graphs were re-plotted between reaction time (min) and fluorescence intensity (RFU) shown in Figure 3.13A. The reaction rates were determined from the slope of the fluorescence intensity-versus-time. An instantaneous rate near the beginning of each concentration reaction ($t=0$), known as an initial rate, was used to study the reaction kinetics. In this work, the reaction times from 0 to 30 min were utilized to calculate initial rates since the calibration curves showed good linearity.

The slopes of the calibration (reaction rate) decreased after 40 min due to the consumption of reactants.

The initial rate (slope) was plotted against cyanide concentrations with a linear range from 0 to 200 μM ($y = 0.7745x + 29.17$; $R^2=0.9954$). The calibration curve (Figure 3.13B) can be used as an alternative to quantify the cyanide concentration in an unknown sample. While this advantage increases specificity and precision, a kinetic method does require multiple data collections and time for processing.

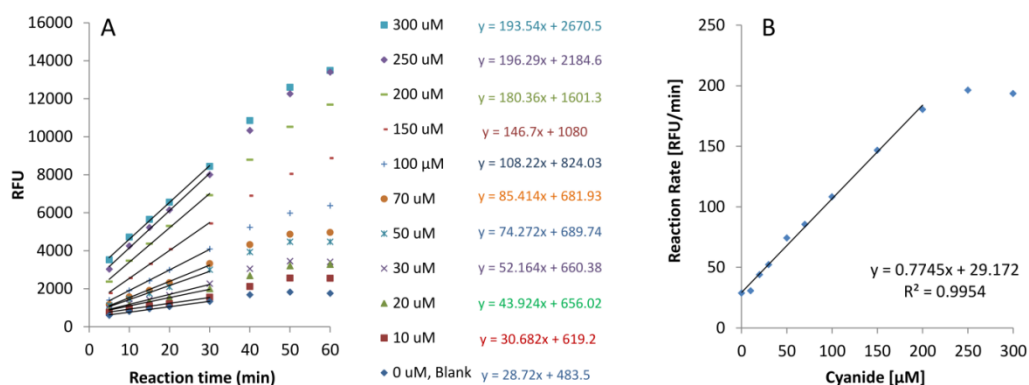


Figure 3.13 Kinetic fluorescence method showing (A) calibration graphs plotted between reaction time and fluorescence signal at different cyanide concentrations; (B) Calibration curve for reaction-rate determination of cyanide.

From the rates of reaction, the reaction order providing the information about reaction mechanism can be calculated. Given the reaction only involves copper and cyanide, the rate equation was defined as below;

$$\text{Reaction rate} = k[\text{CN}^-]^a[\text{Cu}^{2+}]^b$$

Table 3.3 The relationship between cyanide concentrations and reaction rates.

Experiment No	Cyanide (μM)	Copper	Reaction rate (RFU/min)
1	0	Constant as a sensor	28.72
2	10		30.68
3	20		43.92
4	30		52.16
5	50		74.27
6	70		85.41
7	100		108.22
8	150		146.70
9	200		180.36
10	250		196.29
11	300		193.54

The reaction order “a” with respect to cyanide can be made by pairing 2 experiments. The equation below was derived using data from experiments 5 and 7 from Table 2.

$$\frac{108.22}{74.27} = \frac{k [100 \mu\text{M}]^a}{k [50 \mu\text{M}]^a}$$

Solving the equation for a, reveals the order of the reaction with respect to cyanide to be 0.5, indicating the mechanism of reaction as a complex formation.

3.5 Conclusions

We have developed a rapid cyanide detection system on a paper-based well plate with a novel fabrication technique. Polycaprolactone acts as a hydrophobic barrier between individual wells/assays and also serves as an adhesive for assembling the multi-layer plates. The modulation of Cu^{2+} on chitosan-CdTe QDs nanoparticles on the well plate enabled the signal “ON” for the presence of cyanide in a range of 0-

200 μM . The paper-based well plate for cyanide detection showed high precision and accuracy upon validation. The disposable paper-based well plate offers a simple, rapid, high-throughput, and low-cost approach to cyanide detection in water samples at the relevant ranges of concentration comparable to the commercially available with the added benefit of quantitative results.

3.6 Acknowledgments

The authors acknowledge Craig E. Brauer for editorial review.

3.7 References

- (1) ATSDR - Public Health Statement: Cyanide
<https://www.atsdr.cdc.gov/phs/phs.asp?id=70&tid=19> (accessed Nov 27, 2016).
- (2) Carl A. Burtis; Ashwood, E. R.; Bruns, D. E. *Tietz Textbook of Clinical Chemistry and Molecular Diagnostics*, 5 edition.; Saunders: St. Louis, Mo, 2011.
- (3) US EPA, O. Table of Regulated Drinking Water Contaminants
<https://www.epa.gov/ground-water-and-drinking-water/table-regulated-drinking-water-contaminants> (accessed Feb 8, 2017).
- (4) Eisler, R.; Wiemeyer, S. N. In *Reviews of Environmental Contamination and Toxicology*; Ware, D. G. W., Ed.; Reviews of Environmental Contamination and Toxicology; Springer New York, 2004; pp 21–54.
- (5) Eisler, Ronald. *Cyanide Hazards to Fish, Wildlife, and Invertebrates: A Synoptic Review*; Biological Report 85(1.23); U.S. Fish and Wildlife Service, 1991.
- (6) US EPA, O. Approved CWA Test Methods: Inorganic Non-Metals
<https://www.epa.gov/cwa-methods/approved-cwa-test-methods-inorganic-non-metals> (accessed Dec 25, 2016).
- (7) Ma, J.; Dasgupta, P. K. *Anal. Chim. Acta* **2010**, 673 (2), 117–125.
- (8) Xu, Z.; Chen, X.; Kim, H. N.; Yoon, J. *Chem. Soc. Rev.* **2009**, 39 (1), 127–137.

- (9) Randviir, E. P.; Banks, C. E. *TrAC Trends Anal. Chem.* **2015**, *64*, 75–85.
- (10) Lee, C.-H.; Yoon, H.-J.; Shim, J.-S.; Jang, W.-D. *Chem. – Eur. J.* **2012**, *18* (15), 4513–4516.
- (11) Jeong, Y.-H.; Lee, C.-H.; Jang, W.-D. *Chem. – Asian J.* **2012**, *7* (7), 1562–1566.
- (12) Park, S.; Kim, H.-J. *Chem. Commun.* **2010**, *46* (48), 9197–9199.
- (13) Jo, J.; Olsaz, A.; Chen, C.-H.; Lee, D. *J. Am. Chem. Soc.* **2013**, *135* (9), 3620–3632.
- (14) Cheng, X.; Zhou, Y.; Qin, J.; Li, Z. *ACS Appl. Mater. Interfaces* **2012**, *4* (4), 2133–2138.
- (15) Goswami, S.; Manna, A.; Paul, S.; Das, A. K.; Aich, K.; Nandi, P. K. *Chem. Commun.* **2013**, *49* (28), 2912–2914.
- (16) Lv, X.; Liu, J.; Liu, Y.; Zhao, Y.; Chen, M.; Wang, P.; Guo, W. *Sens. Actuators B Chem.* **2011**, *158* (1), 405–410.
- (17) Gómez, T.; Moreno, D.; Díaz de Greñu, B.; Fernández, A. C.; Rodríguez, T.; Rojo, J.; Cuevas, J. V.; Torroba, T. *Chem. – Asian J.* **2013**, *8* (6), 1271–1278.
- (18) Kumari, N.; Jha, S.; Bhattacharya, S. *J. Org. Chem.* **2011**, *76* (20), 8215–8222.
- (19) Shi, B.; Zhang, P.; Wei, T.; Yao, H.; Lin, Q.; Zhang, Y. *Chem. Commun.* **2013**, *49* (71), 7812–7814.
- (20) Saha, S.; Ghosh, A.; Mahato, P.; Mishra, S.; Mishra, S. K.; Suresh, E.; Das, S.; Das, A. *Org. Lett.* **2010**, *12* (15), 3406–3409.
- (21) Ajayakumar, M. R.; Asthana, D.; Mukhopadhyay, P. *Org. Lett.* **2012**, *14* (18), 4822–4825.
- (22) Ajayakumar, M. R.; Mukhopadhyay, P.; Yadav, S.; Ghosh, S. *Org. Lett.* **2010**, *12* (11), 2646–2649.
- (23) Ajayakumar, M. R.; Mandal, K.; Rawat, K.; Asthana, D.; Pandey, R.; Sharma, A.; Yadav, S.; Ghosh, S.; Mukhopadhyay, P. *ACS Appl. Mater. Interfaces* **2013**, *5* (15), 6996–7000.
- (24) Touceda-Varela, A.; Stevenson, E. I.; Galve-Gasi6n, J. A.; Dryden, D. T. F.; Mareque-Rivas, J. C. *Chem. Commun.* **2008**, No. 17, 1998–2000.
- (25) Shang, L.; Zhang, L.; Dong, S. *Analyst* **2008**, *134* (1), 107–113.

- (26) Pengpumkiat, S.; Wu, Y.; Boonloed, A.; Bandara, G. C.; Remcho, V. T. *Anal. Methods* **2017**.
- (27) NYC Office of Chief Medical Examiner - Forensic Toxicology SOP <http://www.nyc.gov/html/ocme/html/ftox/SOP.shtml> (accessed Dec 14, 2016).
- (28) Rella, J.; Marcus, S.; Wagner, B. J. *J. Toxicol. -- Clin. Toxicol.* **2004**, *42* (6), 897–900.
- (29) Fligner, C. L.; Luthi, R.; Linkaityte-Weiss, E.; Raisys, V. A. *Am. J. Forensic Med. Pathol.* **1992**, *13* (1), 81–84.
- (30) Dalefield, R. R. *Vet. Hum. Toxicol.* **2000**, *42* (6), 356–357.
- (31) Carrilho, E.; Phillips, S. T.; Vella, S. J.; Martinez, A. W.; Whitesides, G. M. *Anal. Chem.* **2009**, *81* (15), 5990–5998.
- (32) Koesdjojo, M. T.; Pengpumkiat, S.; Wu, Y.; Boonloed, A.; Huynh, D.; Remcho, T. P.; Remcho, V. T. *J. Chem. Educ.* **2015**, *92* (4), 737–741.
- (33) Koesdjojo, M. T.; Wu, Y.; Boonloed, A.; Dunfield, E. M.; Remcho, V. T. *Talanta* **2014**, *130*, 122–127.
- (34) Koesdjojo, M. T.; Nammoonoy, J.; Wu, Y.; Frederick, R. T.; Remcho, V. T. *J. Micromechanics Microengineering* **2012**, *22* (11), 115030.
- (35) Wei, F.; Lu, X.; Wu, Y.; Cai, Z.; Liu, L.; Zhou, P.; Hu, Q. *Chem. Eng. J.* **2013**, *226*, 416–422.
- (36) Yu, W. W.; Qu, L.; Guo, W.; Peng, X. *Chem. Mater.* **2003**, *15* (14), 2854–2860.
- (37) Nie, Q.; Tan, W. B.; Zhang, Y. *Nanotechnology* **2006**, *17* (1), 140.
- (38) Li, Z.; Du, Y.; Zhang, Z.; Pang, D. *React. Funct. Polym.* **2003**, *55* (1), 35–43.
- (39) Kang, B.; Chang, S.-Q.; Dai, Y.-D.; Chen, D. *Radiat. Phys. Chem.* **2008**, *77* (7), 859–863.
- (40) Mansur, H. S.; Mansur, A. A. P.; Curti, E.; Almeida, M. V. D. *J. Mater. Chem. B* **2013**, *1* (12), 1696–1711.
- (41) Shukla, S. K.; Mishra, A. K.; Arotiba, O. A.; Mamba, B. B. *Int. J. Biol. Macromol.* **2013**, *59*, 46–58.
- (42) Koev, S. T.; Dykstra, P. H.; Luo, X.; Rubloff, G. W.; Bentley, W. E.; Payne, G. F.; Ghodssi, R. *Lab. Chip* **2010**, *10* (22), 3026–3042.

- (43) Lee, D. W.; Lim, C.; Israelachvili, J. N.; Hwang, D. S. *Langmuir* **2013**, *29* (46), 14222–14229.
- (44) Parkash, R.; Zýka, J. *Microchem. J.* **1972**, *17* (3), 309–317.
- (45) Ryan, M. A.; Ingle, J. D. *Anal. Chem.* **1980**, *52* (13), 2177–2184.
- (46) Kurnia, K.; Giles, D. E.; May, P. M.; Singh, P.; Hefter, G. T. *Talanta* **1996**, *43* (12), 2045–2051.
- (47) Izatt, R. M.; Johnston, H. D.; Watt, G. D.; Christensen, J. J. *Inorg. Chem.* **1967**, *6* (1), 132–135.
- (48) Parkash, R.; Zýka, J. *Microchem. J.* **1972**, *17* (3), 309–317.
- (49) Lu, J.; Dreisinger, D. B.; Cooper, W. C. *Hydrometallurgy* **2002**, *66* (1–3), 23–36.

Rapid Synthesis of a Long Double-Stranded Oligonucleotide from a Single-Stranded Nucleotide Using Magnetic Beads and an Oligo Library

Sumate Pengpumkiat; Myra Koedjojo; Erik R. Rowley; Todd C. Mockler; and
Vincent T. Remcho

PLOS ONE

Public Library of Science

1160 Battery Street, Koshland Building East, Suite 100, San Francisco, CA 94111,

USA 11(3): e0149774. doi:10.1371/journal.pone.0149774

March 1, 2016

CHAPTER 4

RAPID SYNTHESIS OF A LONG DOUBLE-STRANDED OLIGONUCLEOTIDE FROM A SINGLE-STRANDED NUCLEOTIDE USING MAGNETIC BEADS AND AN OLIGO LIBRARY**4.1 Abstract**

Chemical synthesis of oligonucleotides is a widely used tool in the field of biochemistry. Several methods for gene synthesis have been introduced in the growing area of genomics. In this paper, a novel method of constructing dsDNA is proposed. Short (28-mer) oligo fragments from a library were assembled through successive annealing and ligation processes, followed by PCR. First, two oligo fragments annealed to form a dsDNA molecule. The double-stranded oligo was immobilized onto magnetic beads (solid support) via streptavidin-biotin binding. Next, single-stranded oligo fragments were added successively through ligation to form the complete DNA molecule. The synthesized DNA was amplified through PCR and gel electrophoresis was used to characterize the product. Sanger sequencing showed that more than 97% of the nucleotides matched the expected sequence. Extending the length of the DNA molecule by adding single-stranded oligonucleotides from a basis set (library) via ligation enables a more convenient and rapid mechanism for the design and synthesis of oligonucleotides on the go. Coupled with an automated dispensing system and libraries of short oligo fragments, this novel DNA synthesis method would offer an efficient and cost-effective method for producing dsDNA.

4.2 Introduction

Oligonucleotide synthesis, the chemical synthesis of nucleic acids, has become an important tool in the field of molecular biology. Synthetic oligonucleotides have been utilized in numerous applications such as diagnosis of genetic and infectious diseases, new drug discovery, and disease treatment. Oligonucleotide synthesis has a long history, starting with a synthetic approach developed by Marvin Caruthers in early 1980s.¹ Solid-phase phosphoramidite chemistry is a well-established 4-step process, which elongates a chain of nucleotide from the 3' end to the 5' end, and is used by many commercial DNA synthesizers. The phosphoramidite chemistry has enabled routine synthesis oligos up to 100 nt with error rates of 1 in 200 nt or better,² yet provides short oligonucleotides owing to the fact that the method adds one base at a time to the growing oligonucleotide chain. Each step in the synthetic cycle must have very high yield in order to obtain a final product in the required amount with a very low accumulated error rate. For example, for 200 nt oligo synthesis, 99% yield from each cycle will result in 13% yield of the desired final product. The longer the desired oligomer, the lower the yield that can be obtained from the synthesis process.

To assemble longer DNA strands, a set of pre-synthesized oligonucleotides can be used as building blocks and assembled using enzymatic methods. Ligation-based assembly is a method to join overlapping oligonucleotides using DNA ligase to form a longer gene. Here, all of the oligos are mixed together with DNA ligase and are thermocycled for annealing and ligation to build the gene product. The Polymerase Chain Reaction (PCR) is then used to amplify the full-length product.

The drawbacks of the method are a relatively high probability of generating ligation by-products and the need for multiple overlapping oligos along the entire length of both strands.

Most gene synthesis today is conducted by service companies, and typically employs one or more of four different general approaches: ligation,^{3,4} PCR-mediated assembly,⁵ convergent assembly,⁶ or solid-phase assembly.⁷⁻¹⁰ These approaches are relatively simple and published protocols are available. Recently, technologies and applications of DNA synthesis have been reviewed.^{2,11,12} However, while these approaches generally succeed in producing usable oligos, they each have limitations that can lead to errors in assembly.¹³ Additionally, some sequences are impossible to synthesize using these approaches, and the methodologies, which rely on laboriously constructed large (up to 200-base) oligos, are time consuming and error-prone.

As implemented by service companies, gene synthesis is still being conducted via a largescale, semi-automated process using custom-synthesized individual DNA oligonucleotides. Because every gene is different, each is synthesized anew for each individual purchase order. Attempts have been made to automate the gene synthesis approaches described above by using DNA microarrays or microfluidic devices^{14,15} in synthesis platforms that use ligation or PCR-mediated assembly. However, these technologies and approaches required custom synthesis, purification and amplification of relatively long oligonucleotides that are then joined into longer DNA molecules. In the microarray format, these approaches also tend to produce DNA products of lower-than-ideal purity. Accumulated errors and truncated DNA products can be significant problems as there is no purification following each synthetic step.¹⁶

This is exacerbated by decreasing product yields with longer oligonucleotides due to the fact that chains may either stop growing or incorporate undesired nucleotides. For DNA synthesis in microfluidic systems, the materials used for fabrication must have excellent chemical resistance given the variety of chemicals and organic solvents used in standard DNA synthesis.¹⁷

In this paper, we demonstrated enzymatic DNA synthesis using magnetic beads as solid supports. Magnetic beads have been widely utilized as solid supports for biomolecule separation, as they facilitate washing and easy manipulation of the sample. Typically, streptavidin is coupled to magnetic beads to specifically capture a target of interest such as a nucleic acid, protein, or antibody that has been biotinylated. Recently, chemical gene synthesis using magnetic beads as the solid support was presented.⁶ Short double stranded (ds) oligo fragments 8 bp long were assembled to form longer 32 bp intermediate single stranded fragments through ligation. The target DNA sequence of 128 bp was constructed from four sets of intermediate fragments in a pair-wise manner.

Herein, we describe a proof of principle study for the construction of a full-length double stranded DNA molecule from short fragments of single-stranded nucleotides (ss-oligonucleotides). 28-mer oligo fragments were used as the building blocks to assemble the full length DNA. The gene was constructed by adding one ssDNA fragment at a time to extend the length of a target sequence through repeated ligation reactions. T4 DNA ligase was used to catalyze the formation of phosphodiester bonds between the adjacent 3'-hydroxy and 5'-phosphate termini in the double-stranded DNA. Streptavidin-coated magnetic beads were utilized as the

solid supports for easy means of washing excess reagents at the completion of each ligation process. Without magnetic bead separation for each ligation step in the process, it is impossible to clean or eliminate the unreacted ssDNA from the enzymatic reaction. The magnetic bead purification approach provides each ligation reaction with only main chain DNA on the building block and the fragment ssDNA to be annealed and ligated to the main chain. Compared to conventional ligation-based assembly, our protocol generates more pure and accurate DNA final products, and affords an easy path to full automation through the use of automatic liquid dispenser, work that is ongoing in our laboratory. The overall procedure is shown in Figure 1. In this paper, we demonstrated the successful synthesis of a long dsDNA from a 28-mer library through successive ligation reactions. Combined with an automated system, this novel strategy will provide a powerful and rapid method for synthesizing custom dsDNA molecules in a standard laboratory.

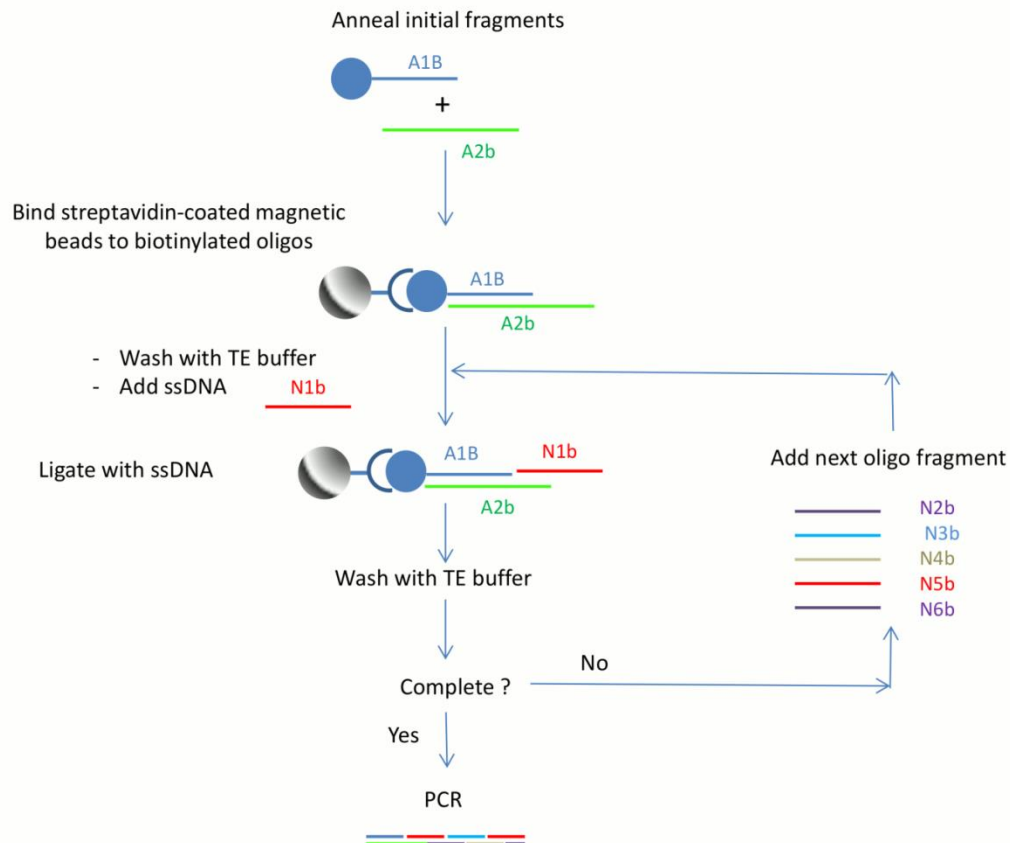


Figure 4.1 Schematic diagram for the proposed dsDNA synthesis. The overall procedure for dsDNA synthesis is composed of three processes: annealing, binding of streptavidin coated magnetic beads to biotinylated oligos, and ligation.

4.3 Materials and methods

4.3.1 Materials

All single-stranded oligonucleotides were purchased from Integrated DNA Technologies (Coralville, IA) with the 5' ends of the oligos phosphorylated. A schematic of the building blocks for construction of the target DNA molecule is shown in Figure 2. The building blocks (N1b-N6b) were synthesized as 28 nucleotide-long fragments that overlapped the next fragment by 14 bases. The first two fragments (A1B and A2b) were designed to be 29 and 43 nucleotides long, respectively. All oligonucleotides were prepared at 100 μ M (Table 1) and were stored

at 4°C throughout the study. Streptavidin-coated magnetic beads, Dynabeads M-270, were obtained from Invitrogen™/Life Technologies (Grand Island, NY). Quick Ligation™ kits were obtained from New England Biolabs (Ipswich, MA).

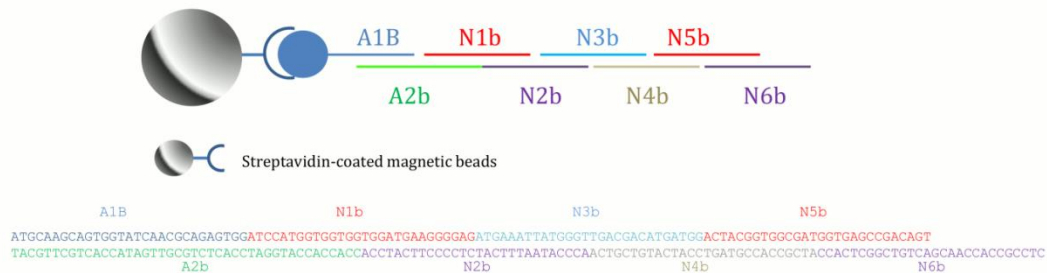


Figure 4.2 Schematic of the building blocks for DNA construction. Streptavidin-coated magnetic beads were used as solid support for dsDNA synthesis and oligo fragments were ligated to the building block one at a time.

Table 4.1 Sequence of the oligo fragments used to form the complete dsDNA.

Sequence name	Sequence	Number of nucleotides
Biotin-A1B	Biotin -5'-ATGCAAGCAGTGGTATCAACGCAGAGTGG-3'	29
A2b	3'-TACGTTTCGTCACCATAGTTGCGTCTCACCTAGGTACCACCACC-5'	43
N1b	5'-ATCCATGGTGGTGGTGGATGAAGGGGAG-3'	28
N2b	3'-ACCTACTTCCCCTCTACTTTAATACCCA-5'	28
N3b	5'-ATGAAATATGGGTTGACGACATGATGG-3'	28
N4b	3'-ACTGCTGTACTACCTGATGCCACCGCTA-5'	28
N5b	5'-ACTACGGTGGCGATGGTGAGCCGACAGT-3'	28
N6b	3'CCACTCGGCTGTCAAGCAACCACCGCCTC-5'	28

Annealing buffer (10×) consisted of 100mM Tris-HCl, 500 mM NaCl, 10 mM EDTA, was adjusted to pH 7.4 with NaOH. The ligation kit contains quick ligation buffer (2× QLB) (132 mM Tris-HCl, 20 mM MgCl₂, 2 mM dithiothreitol, 2 mM ATP, 15% PEG6000, pH 7.6 at 25°C) and T4 ligase. EmeraldAmp® GT PCR Master Mix was obtained from Takara Bio Company (Mountain View, CA). DNA Ladder (O'RangeRuler 20 bp) was obtained from Life Technologies (Grand Island, NY).

Binding and washing buffer (2× B&W) buffer contains 10 mM Tris-HCl, 1 mM EDTA, 2 M NaCl, and 0.05% Tween20, pH 7.5. Binding and washing 1× buffer

(B&W) was prepared by diluting 2× B&W buffer with TE buffer in equal proportions. The TE buffer contains 10 mM Tris-HCl, 1 mM EDTA, and 0.05% Tween20.

Tris-acetate-EDTA (TAE) 50× buffer was obtained from Bio-Rad (Hercules, CA). It was diluted to 1× buffer with deionized water. The composition of 1× TAE buffer was 40mM Tris (pH 7.6), 20 mM acetic acid, and 1 mM EDTA.

4.3.2 Preparation of Streptavidin-coated magnetic beads

50 µL of magnetic beads were washed with 50 µL of 2× B&W buffer (10 mM Tris-HCl pH 7.5, 1 mM EDTA, 2 M NaCl, and 0.05% Tween20) for three times to remove excess sodium azide bacteriostatic agent and resuspended in 50 µL, 1X B&W buffer.

4.3.3 Annealing process

5 µL of stock solutions (100 µM) of the first (A1B) and second (A2b) single-stranded oligo fragments were mixed with 80 µL of deionized water and 10 µL of 10× annealing buffer (100 mM Tris-HCl, 500 mM NaCl, 10 mM EDTA, pH 7.4). The mixture was vortexed and heated in a water bath at 95°C for 10 min, and was slowly cooled to room temperature. The final concentration of each oligonucleotide was 5 µM.

4.3.4 Binding streptavidin coated-magnetic beads and biotinylated oligos

The annealed products from the first two fragments (Biotin A1B-A2b) were incubated with the magnetic beads by gentle-rotation at room temperature for 30 min

and then washed for 2 times with TE buffer to eliminate excess amount of biotinylated oligos from the beads.

4.3.5 Ligation

The magnetic beads (product of 4.3.2.4) were added to a PCR tube along with 8 μL of deionized water, 2 μL of 100 μM subsequent single-stranded oligo (N1b), 10 μL of Quick Ligase Buffer, and 1 μL of T4 ligase. The PCR tube was vortexed and incubated at room temperature (25°C) for 15 min. Phosphodiester bonds were formed between the two fragments at the 5' phosphate and 3' hydroxyl groups.

These steps were repeated for the remainder of the oligo fragments (N2b, N3b, N4b, N5b, and N6b). Excess oligos and T4 ligase enzyme were removed by washing with 2 \times 100 μL of TE buffer after each ligation step. At the end of the ligation process, the magnetic beads were resuspended in 20 μL deionized water.

4.3.6 Polymerase chain reaction (PCR)

The final product of the synthesis was amplified by PCR (Hybaid PCR Express HBPX gradient Thermal Cycler). The forward and reverse primers were 5'-TGCAAGCAGTGGTATCAACG-3' and 5'-ACCATCGCCACCGTAGTC-3', respectively. The PCR solution contained 2 μL of ligation product, 22 μL deionized water, 25 μL Emerald master mix, 1 μL DMSO and 0.5 μL of each primer. The negative control was prepared without the addition of the template DNA. The steps for the PCR program were: 95°C for 30 s, followed by 30 amplification cycles (95°C for 15 s, 65°C for 30 s, and 72°C for 20 s) and 72°C for 5 min.

4.3.7 Gel electrophoresis

PCR products were run on a 3% agarose gel in 1×TAE buffer. The horizontal electrophoresis system and power supply were obtained from Bio-Rad (Hercules, CA). The potential was set at 75 V.

4.3.8 Sanger DNA sequencing

Bands were cut from the gel, extracted, and purified using the GeneJet PCR purification kit from Fermentas (Thermo Scientific, Pittsburgh, PA). The solutions were stored in a freezer (-20°C) prior to DNA sequencing.

4.3.9 One-pot dsDNA synthesis

To perform a one-pot gene synthesis experiment, 5 µL of each of the annealed products of N1b-N2b, N3b-N4b, N5b-N6b was mixed in a tube with 10 µL Quick Ligation Buffer and 1 µL T4 Ligase. The tube was incubated at room temperature for 15 min. The final product was analyzed using gel electrophoresis.

4.4 Results and discussion

We have demonstrated a novel strategy to synthesize a full-length dsDNA molecule accurately and efficiently. A 101-bp long dsDNA product was synthesized by successive ligation of 28-mer fragments. The synthesis process involves annealing, binding of biotinylated oligo fragments to magnetic beads (solid support), and consecutive ligation reactions. In this study, we tested each of these steps separately to ensure the optimization of all conditions prior to synthesizing the full-length

dsDNA. Oligo fragments N1b-N6b shown in Table 1 were used to test and optimize the annealing and ligation processes.

4.4.1 Annealing

Deoxyribonucleic acids recognize their complementary oligonucleotides by base pairing: A-T and G-C. Single-stranded DNA will hybridize with its complement via the formation of hydrogen bonds. The annealing process was carried out at 95°C for 10 min in an annealing buffer that promotes hydrogen bonding between the two complementary ssDNA molecules. The annealing process was tested by pairing N1b with N2b, N3b with N4b, and N5b with N6b. The annealed product was characterized using gel electrophoresis. The lengths of all the annealed products were expected to be 42 bp (28+14). Lanes 2, 3, and 4 in Figure 3 show the expected bands around 40 bp, which suggests that the annealing process was successful.

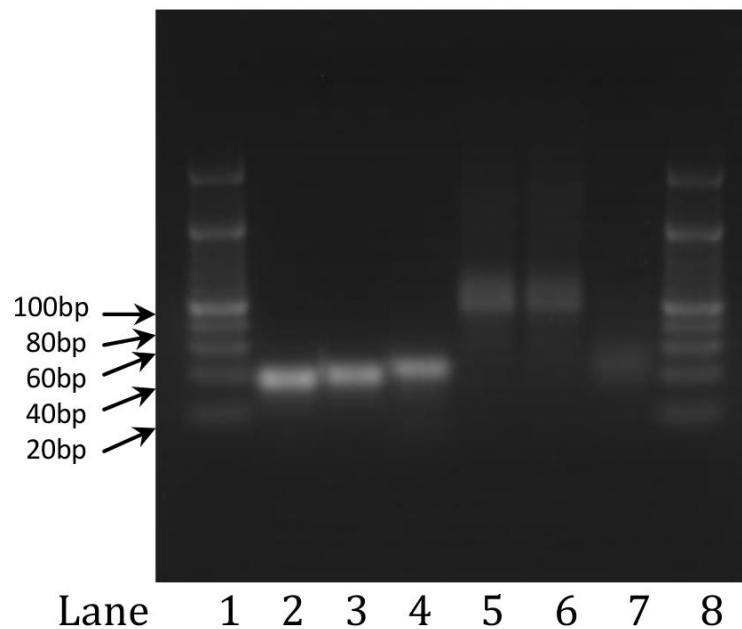


Figure 4.3 Agarose gel electrophoresis of annealed and ligation products. Lane 1 and 8, ladder; Lane 2, annealed product of N1b and N2b; Lane 3, annealed product of N3b and N4b; Lane 4, annealed product of N5b and N6b; Lane 5, “one-pot” ligation product of [(N1b-N2b)+(N3b-N4b)+(N5b-N6b)]; Lane 6, sequential ligation product of [(N1b-N2b)+(N3b-N4b)]+(N5b-N6b); Lane 7, ligation product of [(N1b-N2b)+(N5b-N6b)].

4.4.2 Ligation

In this study, T4 DNA ligase was utilized as the catalyst for the formation of phosphodiester bonds between two ssDNA oligo fragments. This enzyme has been shown to effectively join both blunt and sticky ends of dsDNA. In this part of the study, we wanted to evaluate whether the T4 ligase has a favorable reaction towards dsDNA with sticky ends compared to ssDNA with blunt end. T4 ligase is most commonly used to join dsDNA fragments. In our approach we used this enzyme to join ssDNA fragments with the complementary sticky ends of dsDNA molecules (Figure 4.1).

To better understand the efficiency of the T4 ligase in joining our dsDNA fragments with sticky ends, we first performed a sequential ligation reaction using the annealed products of N1b-N2b, N3b-N4b, and N5b-N6b described in section 4.4.1. The first ligation was carried out between the N1b-N2b and N3b-N4b dsDNA fragments and was allowed to incubate at room temperature for 15 min. The next dsDNA fragment, N5b-N6b, was then added into the solution mixture and incubated under the same conditions as the first ligation. The resulting approximately 100 bp product is shown in Figure 3, Lane 6, and is consistent with our expected product size of 98 bp (28+28+28+14 bp). This confirms that the sequential ligation of dsDNA

fragments with complementary sequences can be accomplished at room temperature as fast as 15 minutes.

We also investigated whether or not the T4 ligase enzyme was able to effectively join dsDNA fragments at their complementary sites in the presence of impurities in the form of other dsDNA fragments. A “one-pot” reaction was performed by mixing all of the annealed products with the T4 ligase in a tube, which was incubated at room temperature (25°C) for 15 min. The resulting product was run on a gel and showed a similar band at ~100 bp (Figure 3, Lane 5). To determine whether or not ligation occurs between the N1b-N2b and N5b-N6b fragments, we ran a similar test in which only these two dsDNA fragments were mixed with the T4 ligase and incubated at 25°C for 15 min. The product was again analyzed on a gel and the result showed a band around 40 bp that corresponded to the sizes of the annealed products themselves (42 bp expected) and not the product of successful ligation (Figure 3, Lane 7). These two annealed products were not designed with complementary sequences in their overhang portions. This result indicated that ligation of dsDNA fragments with non-complementary sticky ends was unfavorable under the specified reaction conditions with T4 ligase. This feature plays an important role in the proposed gene synthesis approach, as it shows that ligation is only favorable in the presence of DNA fragments with complementary sticky ends. This significantly reduced the chance of misalignments or sequence errors in the final gene product as a result of non-complementary oligo fragments that may be present in solution during the ligation process.

4.4.3 Oligonucleotide synthesis using streptavidin-coated magnetic beads

The proposed gene synthesis strategy began with the annealing process, where the biotinylated A1B fragment was annealed with the A2b fragment to form the initial dsDNA molecule. The annealed product of A1B/A2b was immobilized on magnetic beads via streptavidin-biotin binding. Magnetic beads allow for convenient washing and separation of the desired products from excess reagents. Holmberg et al.¹⁸ demonstrated that dissociation of biotin and streptavidin molecules occurs when a solution is heated to 70°C. Thus, the annealing of the first dsDNA fragment was performed prior to its immobilization on the magnetic beads to avoid exposing the immobilized products to the elevated temperature of the annealing process (95°C).

The results from section 4.4.2 demonstrated that T4 DNA ligase was capable of joining dsDNA fragments with complementary sticky ends. In this experiment, the ligation process was repeated by adding the annealed products of N1b-N2b, N3b-N4b and N5b-N6b one at a time to the main chain. At the completion of the ligation reactions, the full-length dsDNA was amplified by PCR. The result is illustrated in Figure 4, lane 2, as a band of approximately 100 bp, which corresponds to the expected length of the final product (101 bp).

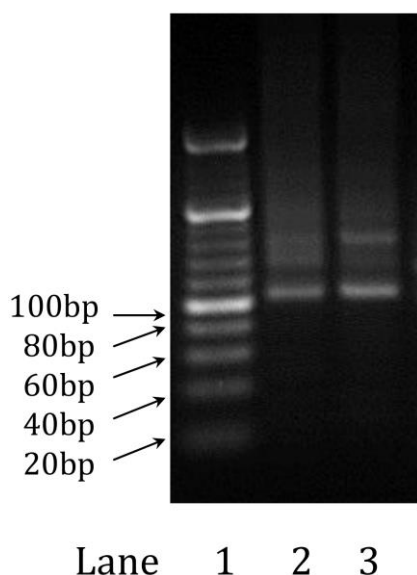


Figure 4.4 Agarose gel electrophoresis of the final product. Lane 1, ladder; Lane 2, ligation product from double-stranded oligo fragments; Lane3, ligation product from single-stranded oligo fragments.

We also investigated whether or not it was possible to ligate single-stranded oligonucleotides sequentially to the main dsDNA chain using the T4 DNA ligase under the same experimental conditions described in section 4.4.2. To test this, 28-mer ssDNA fragments were used as building blocks (rather than the double-stranded oligos), and were ligated one at a time to extend the length of the main chain. Thorough washing was performed at the completion of each ligation step to minimize interference from excess oligos that may still be present in solution. Once all of the ligation steps were completed to form the desired dsDNA, the product was amplified by PCR and analyzed using gel electrophoresis. The result of the PCR product is illustrated in Figure 4 lane 3 and clearly shows a product of approximately 100 bp. We have successfully demonstrated an efficient approach to synthesizing and extending the length of dsDNA through repetitive ligation of short ssDNA oligo fragments. Each cycle of the DNA synthesis step takes approximately 20 minutes,

including the cleaning and washing steps. Our proposed method would take only about 12 hours to synthesize a DNA molecule of 500 bp, whereas today's commercial gene synthesis operations generally require multiple days to synthesize DNA molecules of this size.

4.4.4 Sequencing of the target DNA

PCR products were cut from the agarose gels, extracted, and purified using the GeneJet PCR purification kit (ThermoScientific) for sequencing analysis. Sanger sequencing was performed to characterize the final products. Since the quality of Sanger sequencing was normally poor for the first 20 bp of the DNA sequence, sequencing of the DNA products was performed in both the forward and reverse directions to obtain the whole sequence data. The reproducibility of the gene synthesis approach and the accuracy of the DNA sequencing results were determined by repeating the entire process in triplicate. The resulting PCR product for each process was sequenced 3 times. Sequencing data were aligned and compared to the expected sequence by CodonCode Aligner (v. 5.1.5 CodonCode Corp., MA). The sequence validation by Sanger sequencing revealed that gene synthesis product was nearly identical (97%) to the expected sequence. DNA sequencing alignment is shown in Figure 4.5.

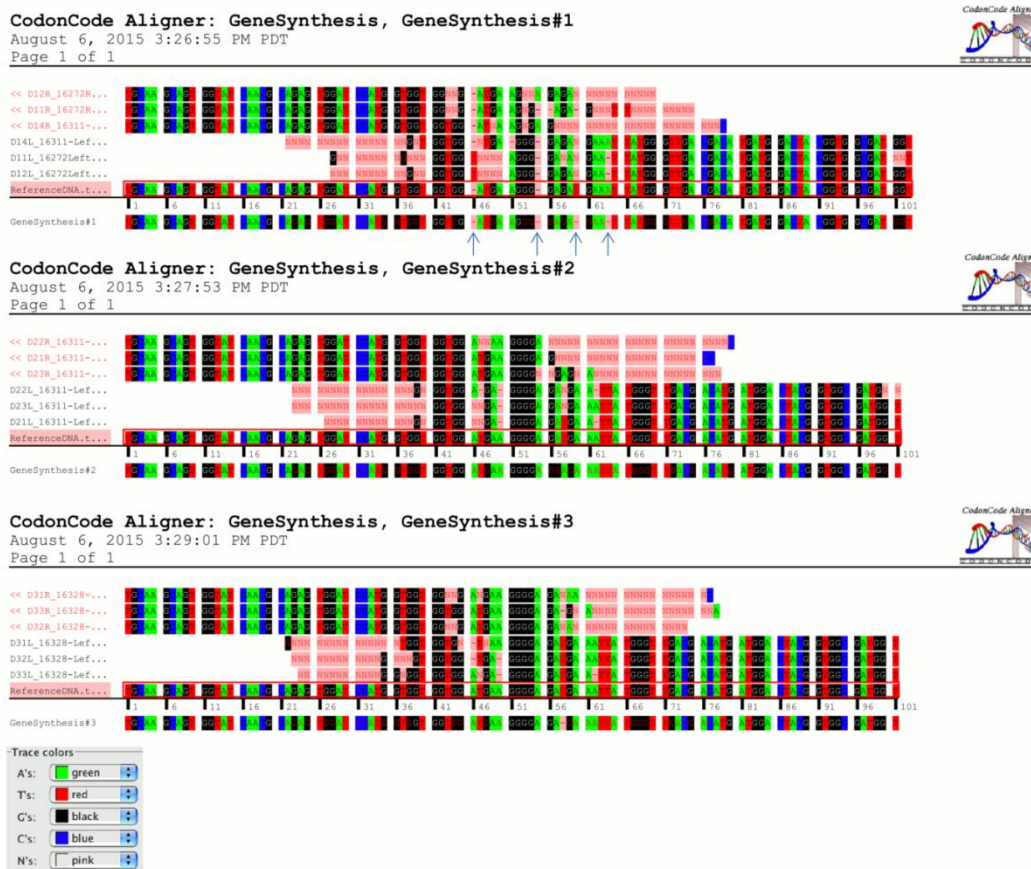


Figure 4.5 DNA sequencing alignment of the final product.

4.5 Conclusions

In this work, we have demonstrated a novel approach of synthesizing a long double stranded oligonucleotide through repetitive ligation of short ssDNA oligo fragments. The method is simple and straightforward, using streptavidin coated magnetic beads as solid supports for ease of washing. The magnetic bead purification for each ligation-based assembly helps promote the assembly of a pure and accurate dsDNA product and enables complete automation of the synthetic approach—work that is underway in our lab. The accuracy of the synthesis method was validated by Sanger sequencing, and the results showed we were able to generate DNA products

with precision of more than 97%. With this approach, it is possible to create custom DNA with rapid turnaround time. Combined with automation technology and access to universal libraries of short oligo fragments, this approach would provide a powerful gene synthesis solution with significant time and cost savings.

4.6 Acknowledgments

We would like to thank Dr. Sergei Filichkin, Department of Botany and Plant Pathology, Oregon State University for mentoring; Yuanyuan Wu, Nicole J. Hams, Sara Townsend for technical discussion; the Oregon State University Center for Genome Research & Biocomputing (CGRB lab) for DNA sequencing and Dr. Genevieve Weber for editorial review.

4.7 References

- (1) Beaucage, S. L.; Caruthers, M. H. *Tetrahedron Lett.* **1981**, *22* (20), 1859–1862.
- (2) Kosuri, S.; Church, G. M. *Nat. Methods* **2014**, *11* (5), 499–507.
- (3) Borodina, T. A.; Lehrach, H.; Soldatov, A. V. *Anal. Biochem.* **2003**, *318* (2), 309–313.
- (4) Kuhn, H.; Frank-Kamenetskii, M. D. *FEBS J.* **2005**, *272* (23), 5991–6000.
- (5) Wu, G.; Wolf, J. B.; Ibrahim, A. F.; Vadasz, S.; Gunasinghe, M.; Freeland, S. J. *J. Biotechnol.* **2006**, *124* (3), 496–503.
- (6) Horspool, D. R.; Coope, R. J.; Holt, R. A. *BMC Res. Notes* **2010**, *3* (1), 291.
- (7) Caruthers, M. H. *Science* **1985**, *230* (4723), 281–285.
- (8) Caruthers, M. H. *Acc. Chem. Res.* **1991**, *24* (9), 278–284.
- (9) Sierzchala, A. B.; Dellinger, D. J.; Betley, J. R.; Wyrzykiewicz, T. K.; Yamada, C. M.; Caruthers, M. H. *J. Am. Chem. Soc.* **2003**, *125* (44), 13427–13441.

- (10) Kumar, P.; Gupta, K. C. *Bioconjug. Chem.* **2003**, *14* (3), 507–512.
- (11) Vaijayanthi, B.; Kumar, P.; Ghosh, P. K.; Gupta, K. C. *Indian J. Biochem. Biophys.* **2003**, *40* (6), 377–391.
- (12) Engels, J. W.; Uhlmann, E. *Angew. Chem. Int. Ed. Engl.* **1989**, *28* (6), 716–734.
- (13) LeProust, E. M.; Peck, B. J.; Spirin, K.; McCuen, H. B.; Moore, B.; Namsaraev, E.; Caruthers, M. H. *Nucleic Acids Res.* **2010**, *38* (8), 2522–2540.
- (14) Engels, J. W. *Angew. Chem. Int. Ed.* **2005**, *44* (44), 7166–7169.
- (15) Kim, H.; Jeong, J.; Bang, D. *J. Biotechnol.* **2011**, *151* (4), 319–324.
- (16) Baker, M. *Nat. Methods* **2011**, *8* (6), 457–460.
- (17) Tian, J.; Ma, K.; Saaem, I. *Mol. Biosyst.* **2009**, *5* (7), 714–722.
- (18) Holmberg, A.; Blomstergren, A.; Nord, O.; Lukacs, M.; Lundeberg, J.; Uhlén, M. *ELECTROPHORESIS* **2005**, *26* (3), 501–510.

CHAPTER 5

SUMMARY AND CONCLUSIONS

Microfluidic analytical systems have been developed rapidly and gained much attention over the last three decades. Integration of fluid handling, extraction, preconcentration, and conducting of reactions in microscale volumes on a chip offers significant advantages to the field of chemical analysis, especially as regards biomedical/clinical research. Microsystems often reduce the necessary sample size to the microliter or even nanoliter scale, reduce waste generation, can be made to be safely disposable, facilitate rapid mixing and fluidic transport (reducing analysis time), increase sample throughput, and are inexpensive. A wealth of platforms and fabrication techniques are currently available on inorganic media, thermoplastics, elastomeric polymers, and on paper, glass microfiber, and organic membrane materials. Our research group fabricated a novel technique for microfluidic chip production utilizing polycaprolactone (PCL) as a bonding agent¹ and sidewall material for hydrophobic patterning,² which was utilized extensively in the work presented here.

The development of microfluidic detection systems integrating semiconductor nanocrystal quantum dots (QDs) was also presented in this dissertation. The size-dependent optical properties of QDs and their chemical compositions offer a unique detection mechanism. This part of the research effort started with QD synthesis in aqueous solution. Then, MPA-capped CdTe QDs were further surface modified to enhance their optical properties and promote their use on two distinct microfluidic

platforms. Silica and chitosan encapsulation were utilized in Chapters 2 and 3, respectively, to facilitate the use of QD pairs for ratiometric measurements.

In Chapter 2, a quantum dot wavelength-ratiometric sensor was built for copper detection and transferred to a polymer-based microfluidic format to facilitate parallel analysis of multiple samples and standards. CdTe QDs with green emission (530 nm) were cladded in a silica shell and used to generate a sample-independent baseline emission signal. CdTe/CdS QDs with red emission (650 nm) were decorated on the silica surface for the purpose of sensing the presence of copper ions in the sample. Copper specifically and quantitatively quenched the red QDs while the protected green QDs (embedded in the silicate shell) continued to emit, resulting in a visual color change from red to green corresponding to the increasing copper concentration. The assay was successfully transferred to a PMMA-based chip produced using a PCL bonding technique. Each chip accommodated 10 individual assays, which were used simultaneously. This approach allowed digital image analysis (in the RGB color space) to be used as a tool for quantitation, replacing a purpose-built fluorescence spectrometer. Using a low-cost UV lamp (365 nm) as an excitation source, the microfluidic copper detection system proved to be highly portable and enabled high sample throughput for both environmental water samples and biological serum samples in clinically significant, relevant concentrations.

In Chapter 3, a novel, disposable, paper-based well plate was developed and applied to the detection and quantitation of cyanide in solution. Detection was accomplished using chitosan modified CdTe QDs. Here, MPA-CdTe QDs with a maximum emission at 520 nm were encapsulated in chitosan; these CS-QDs were

quenched by copper prior to their use as sensor probes for cyanide. Upon exposure to cyanide, fluorescence was recovered due to the displacement of copper from the quenched QD by formation of copper cyanide complexes $[\text{Cu}(\text{CN})_x]^{1-x}$. Fluorescence “ON” signal was graphed against the cyanide concentration in the clinically relevant concentration range. The solution based fluorescence assay was then transferred to the microfluidic format in a μPAD . Here, PCL and a glass microfiber filter (GF/B) enabled an increase in fluorescence intensity relative to the solution assay owing to the increased surface area to volume ratio.

A disposable paper-based well plate was designed as a multilamellar device. The two functions of PCL in constructing this device were: (1) bonding, and (2) serving as a hydrophobic barrier to maintain the integrity of each individual assay in the 96 well plate. This format allowed for existing technology, a fluorescence microplate reader, to be used to quantitatively determine analyte concentrations in an automated fashion. The detection system demonstrated high precision and accuracy. The disposable paper-based well plate offered a simple, rapid, high-throughput, and low-cost approach to cyanide detection in water samples at the relevant ranges of concentration, performing comparably to the commercially available “Cyantesmo®” assay with the added benefits of quantitative (rather than qualitative) results, increased sample throughput, automation, and decreased cost.

In Chapter 4, a novel technique for constructing a long dsDNA from a library of fragmented ssDNA was presented. Magnetic beads were used as solid supports as they facilitated washing at each step. To prove the concept, 28-mer oligo fragments were used as building blocks by adding one ssDNA fragment at a time to extend the

length of the target sequence. T4 DNA ligase was used to catalyze the formation of phosphodiester bonds at the sticky-end of each fragment. The full-length of synthesized dsDNA was amplified using PCR. Sanger sequencing was used to determine the precise order of nucleotides within the target DNA molecule. Compared to a conventional method (phosphoramidite), the novel approach presented here generated higher purity final DNA products with fewer defects. Combined with an automated dispenser, this novel strategy holds the promise to provide a powerful and rapid method for synthesizing custom dsDNA molecules in the laboratory of an end-user, obviating the need to order custom long-strand DNA from outside suppliers and eliminating both a research bottleneck and a “middleman”.

In conclusion, this work has expanded the range of materials and methods available for the production and application of microscale systems – from the production and application of QDs for chemical analysis in micro-total analysis systems, to the automated synthesis of genes. In large part, this work focused on development of disposable polymer-based and paper-based microfluidic platforms that demonstrably enabled simple, low-cost, high throughput, sensitive measurements of biologically and environmentally relevant target analytes.

5.1 References

- (1) Koesdjojo, M. T.; Nammoonnoy, J.; Wu, Y.; Frederick, R. T.; Remcho, V. T. *J. Micromechanics Microengineering* **2012**, 22 (11), 115030.
- (2) Heist, C. A. Polycaprolactone-based microfluidic devices: fabrication methods and applications in low-cost analytical devices, Oregon State University: Corvallis, OR, 2016.